

ON THE POTENTIAL FOR FIBER-OPTIC DISTRIBUTED MAGNETIC SENSING IN
NEAR-SURFACE GEOPHYSICS

by
Tomas H. Snyder

© Copyright by Tomas H. Snyder, 2024

All Rights Reserved

A thesis submitted to the Faculty and the Board of Trustees of the Colorado School of Mines in partial fulfillment of the requirements for the degree of Master of Science (Hydrologic Science and Engineering).

Golden, Colorado

Date _____

Signed: _____

Tomas H. Snyder

Signed: _____

Dr. Eileen Martin
Thesis Advisor

Golden, Colorado

Date _____

Signed: _____

Dr. David Benson
Professor and Program Head
Hydrologic Science and Engineering Program

ABSTRACT

Breakthroughs in distributed fiber optic sensing have enabled continuous recording of seismic and temperature data, resulting in unparalleled spatial resolution and coverage at a more affordable cost in remote areas. Electromagnetic data has proven to be useful in providing additional insight into near-surface applications, however, distributed electromagnetic sensing systems are still in the prototype stage. This thesis explores the attributes of a multi-physics optical fiber that records seismic waves and magnetic fields simultaneously and its potential for application in selected near-surface problems.

Current applications of magnetic geophysical methods are discussed and used to inform potential uses of the distributed magnetic sensing fiber, particularly for improved monitoring of seawater intrusion, mine drainage, and lithium brines. Simulations of these potential groundwater application areas are explored with a hypothetical survey design and computational simulation. Preliminary magnetic field sensitivity requirements of the fiber are established based on simulation results.

Laboratory experiments to determine the fiber sensitivity to magnetic fields are performed in addition to field tests that are used to discuss practical applications of the fiber in geophysical surveys. Additional testing was performed to provide insight into the variation of the fiber signal over time. Studies are conducted using a fiber with Bragg gratings as well as a fiber without Bragg gratings to guide future fiber design and selection.

The magnetostrictive effect underlies the basic measurement principle of the proposed distributed magnetic sensing. Two-dimensional and three-dimensional modeling of the magnetic fiber based on micromagnetic dynamics and magnetostriction are explored in this thesis to improve the understanding of the mechanisms causing a response in the fiber and ensure data can be reliably modeled, even in the face of nonlinearity. Model sensitivity to source magnetic field amplitude, source frequency, environmental temperature, initial conditions, and the Gilbert damping parameter is explored. Comparisons of model amplitude spectra to laboratory-measured amplitude spectra along with model prediction of fiber sensitivity offer insight into the reliability of the models.

TABLE OF CONTENTS

ABSTRACT	iii
LIST OF FIGURES	vii
LIST OF SYMBOLS	xiii
LIST OF ABBREVIATIONS	xiv
ACKNOWLEDGMENTS	xv
CHAPTER 1 INTRODUCTION	1
1.1 Applications of Magnetic Methods	1
1.2 Distributed Fiber Optic Sensing	4
1.3 Ferromagnetism and Magnetostriction	7
1.4 DMS Application Background	9
1.4.1 Seawater Intrusion	9
1.4.2 Mine Drainage	10
1.4.3 Lithium Brine Mining	10
1.5 Laboratory Experiment Background	11
1.6 Field Experiment Background	11
1.7 Motivation and Thesis Layout	12
CHAPTER 2 FEASIBILITY OF DMS FOR HYDROGEOLOGIC PROBLEMS	13
2.1 Groundwater Solution Monitoring Methods	13
2.1.1 Design of Application	13
2.1.2 Simulation	14
2.2 Seawater Intrusion Modeling	16
2.2.1 Simple Model	16
2.2.2 Gradient Model	18
2.3 Mine Drainage Modeling	20
2.4 Lithium Brine Modeling	22

2.5	Model Limitations	23
2.6	Conclusions	25
CHAPTER 3 LABORATORY AND FIELD EXPERIMENTS		27
3.1	Laboratory Experiments	27
3.1.1	Experimental Design	29
3.1.2	Data and Analysis	30
3.1.3	Laboratory Results and Discussion	31
3.2	Field Experiments	33
3.2.1	Field Test with Bragg Grating Fiber and Solenoid	33
3.2.2	TEM Experiments	35
3.2.2.1	First Trial	36
3.2.2.2	Second Trial	40
3.2.3	Field Experiment Results and Discussion	40
CHAPTER 4 COMPUTATIONAL MODELING OF DMS		43
4.1	Two-Dimensional Model	43
4.1.1	Applied Magnetic Field Sensitivity	45
4.1.2	Initial Angle Sensitivity	46
4.1.3	Frequency Sensitivity	47
4.1.4	Discussion of the Two-Dimensional Model	48
4.2	Three-Dimensional Model	49
4.2.1	Applied Magnetic Field Sensitivity	52
4.2.2	Damping Parameter Sensitivity	53
4.2.3	Temperature Dependence	55
4.2.4	Discussion of the Three-Dimensional Model	56
CHAPTER 5 SUMMARY AND CONCLUSION		58
5.1	Summary of Results	58
5.2	Future Work	59

REFERENCES 61

APPENDIX A MODELING CODE 67

APPENDIX B SOIL BOX FOR ENVIRONMENTAL CONDITION STUDIES 103

APPENDIX C FIBER MANUAL ALIGNMENT METHOD 104

APPENDIX D FURTHER TWO-DIMENSIONAL MODELING 107

APPENDIX E APPLICATION SIMULATION OF BOREHOLE WATER SOLUTION 110

LIST OF FIGURES

Figure 1.1	This figure shows what a magnetic anomaly looks like in aerial data captured 10 m above the surface due to a spherical block of a magnetic mineral in the subsurface. The block is centered at $x = 0$ m and $y = 0$ m with a radius of 15 m and a depth of 50 m (top). The simulated data created using SimPEG is shown in the bottom image (Cockett <i>et al.</i> , 2015).	2
Figure 1.2	A schematic illustration of the distributed acoustic and magnetic sensing fiber is shown in this image. This illustration shows a fiber with two rods of magnetostrictive material, however, other fiber configurations have been created and tested (Hileman <i>et al.</i> , 2022). . .	5
Figure 1.3	This image illustrates a change in length Δl of a magnetostrictive material due to an external magnetic field. Δl can represent an increase or decrease in length depending on material properties (image adapted from Pérez-Aparicio & Sosa 2004).	6
Figure 1.4	The domains within a ferromagnetic material are sections of magnetic saturation M_s , with magnetization vectors oriented in different directions. The net magnetic field outside the material due to the internal magnetic moments is zero when not magnetized by an external magnetic field (left). When a magnetic field \vec{H} is applied to the material, the magnetic dipoles align in the direction of the external field, causing a change in length Δl (right).	8
Figure 1.5	This illustration shows a typical saltwater-freshwater interface in seawater intrusion. The transition zone is a mix of saltwater and freshwater (adapted from Costall <i>et al.</i> 2020).	9
Figure 2.1	This figure shows a simple model of an application of the DMS fiber, wherein the DMS fiber is buried within the borehole and a magnetic field is applied to the whole block model. The unsaturated zone is yellow and the saturated zone is blue in this image. . . .	13
Figure 2.2	This illustration shows a simple subsurface model slice at $y = 0$ m that was created for magnetic simulation forward modeling of a simple seawater intrusion boundary. There are two blocks of different χ values (purple and green) representative of water with different solutes. These blocks are placed below five meters to represent a water table with dry soil on top (yellow layer).	14
Figure 2.3	The forward modeling results of Figure 2.2 are shown in this image. The sensors are ten meters deep and are placed two meters apart to model the Bragg grating spacing of the DMS fiber. This image is a two-dimensional slice at the sensor depth of 10 m. There is a clear shift of 17 nT in the value of the TMI anomaly visible at the interface between the saltwater and freshwater.	15
Figure 2.4	The profiles at $y = 0$ m of the forward modeled TMI anomaly data slice at the sensor depth, with sensors at different depths are shown in this illustration. For these models, the boundary between the saltwater and freshwater blocks was placed at $x = 0$ m. The water table is at a depth of 5 m. We see this reflected in the simulations as the boundary resolution improves greatly when the sensors are placed below the water table at a depth of 7.5 m and deeper.	16

Figure 2.5	The profiles at $y = 0$ m and $z = -10$ m of the forward modeled TMI anomaly data with different saltwater-freshwater boundary locations are shown in this illustration. The sudden changes in TMI anomaly are at the same x locations as the boundary. This illustration shows that the forward-modeled data accurately represents the boundary location at any point along the profile.	17
Figure 2.6	This illustration shows the subsurface model slice at $y = 0$ m that was created for magnetic simulation forward modeling of the gradient seawater intrusion model. The saltwater is on the left with a gradient in χ towards the freshwater. The χ values from left to right are $\chi_{seawater} = -6.5 \times 10^{-5}$, $\chi_1 = -5 \times 10^{-5}$, $\chi_2 = -4 \times 10^{-5}$, and $\chi_{freshwater} = -3 \times 10^{-5}$	18
Figure 2.7	The forward modeling results of Figure 2.6 are shown in this image. The sensors are ten meters deep and are placed two meters apart to model the Bragg grating spacing of the DMS fiber. This image is a two-dimensional slice at the sensor depth of 10 m. There are two major shifts visible in this data along the x -axis that coincide with changes in χ at a depth of 10 m.	19
Figure 2.8	The profiles at $y = 0$ m and of the forward modeled TMI anomaly data slice at the sensor depth, with sensors at different depths of the model in Figure 2.6 are shown in this illustration. Shifts that are relatively large in the TMI anomaly data compared to the gradual slopes of the data are indicative of χ boundaries.	20
Figure 2.9	The forward modeling results with iron as a solute with χ values based on are shown in this image. The sensors are ten meters deep and are placed two meters apart to model the Bragg grating spacing of the DMS fiber. This image is a two-dimensional slice at the sensor depth of 10 m. There is a slight change in TMI anomaly at the boundary between the freshwater and iron water at $x = 0$ m, but it is not as obvious as seen in the seawater intrusion model.	21
Figure 2.10	The profiles at $y = 0$ m and $z = -10$ m of the forward modeled TMI anomaly data with sensors at a depth of 10 m in the model shown in Figure 2.2 are shown in this illustration. The profiles shown are for different concentrations of Fe^{2+} in the right block with freshwater in the left block. The 0 mg/L, 1 mg/L, and 10 mg/L lines overlap nearly completely.	22
Figure 2.11	The profiles at $y = 0$ m and $z = -10$ m of the forward modeled TMI anomaly data with sensors at a depth of 10 m in the model shown in Figure 2.2 are shown in this illustration. The profiles shown are for different concentrations of Li^+ in the right block with freshwater in the left block.	23
Figure 2.12	In this proposed application method, the fiber will be placed in a horizontal borehole below the water table (blue) with a solenoid surrounding it. An alternating current would be sent through the solenoid to produce an alternating magnetic field that the fiber would respond to.	24
Figure 3.1	The laboratory setup for testing the DMS fiber without Bragg gratings is shown in this image. The top image shows the actual laboratory setup, while the bottom image shows a simplified diagram of the laboratory setup. The interrogator is not shown in the top image.	28
Figure 3.2	The current amplifier (left) and its circuit diagram (right) are shown in this image. The current amplifier is not attached to the solenoid in the left image, but the solenoid is shown as a 1Ω load in the circuit diagram.	29

Figure 3.3	The time series (left) and power spectrum (right) output for an AC source amplitude of 3.0 V are shown in this image. The power spectrum shows a 1000 Hz and 2000 Hz fiber response, which are typical magnetostrictive responses at the source frequency and double the source frequency.	30
Figure 3.4	The experimental spectral response amplitudes of the fiber without Bragg gratings for the 1000 Hz response to a 1000 Hz solenoid source are plotted against magnetic field strength in this figure. The signal fades from the power spectrum at 0.2 mT.	31
Figure 3.5	The power spectrum variation over time of the fiber response for an AC source amplitude of 3.0 V and a frequency of 1000 Hz is shown in this plot. The 1000 Hz and 2000 Hz response magnitudes were calculated using sample sliding windows (30 s length, 5 s offset) of the 300 s signal.	32
Figure 3.6	The experimental setup for the Metglas fiber with Bragg gratings is shown in this image. The fiber was lightly buried underneath the solenoid in this experimental setup (figure courtesy of Shihao Yuan).	34
Figure 3.7	Amplitude spectra of the DMS fiber response to the solenoid on top of the fiber at 100 Hz (left) and 1000 Hz (right) are shown in this image. These spectra were calculated from channel 20 of the fiber and are normalized by the number of samples.	35
Figure 3.8	This image shows amplitude spectra recorded by the Bragg grating DMS fiber with the solenoid on top of the fiber (left), and 0.5m away from the fiber (right). These spectra were calculated from channel 20 of the fiber and are normalized by the number of samples.	36
Figure 3.9	This image shows the signal from the TEM unit in the time domain (top) and the frequency domain (bottom). The frequency domain signal shows an initial peak around 33 Hz and harmonics at higher frequencies.	37
Figure 3.10	The top images show the first trial field setup. A diagram of the field setup is shown in the bottom image.	38
Figure 3.11	The frequency response of the entire length of the fiber (top) and power spectrum of channel 12 at 19.6 m (bottom) for the first trial are shown in this image.	39
Figure 3.12	The field setup for the second trial (left) and a simplified diagram of the field setup (right) are shown in this image.	40
Figure 3.13	The frequency response of the entire length of the fiber (top) and power spectrum of channel 15 at 24.5 m (bottom) for the second trial are shown in this image.	42
Figure 4.1	A visualization of the 2D model setup is shown in this image. The x direction is also the strain measurement direction, with saturation occurring in the direction of \vec{M} , where $\ \vec{M}\ = M_s$	43
Figure 4.2	This figure shows an example of the modeled strain response to a source with a frequency of 100 Hz in the time domain (left) and the frequency domain (right). In the time domain, frequency doubling is apparent as two oscillations occur within 0.01 s. In the frequency domain, the spectrum shows clear peaks at 100 Hz, 200 Hz, and 300 Hz. Peaks at 400 Hz and 500 Hz are also present, though much smaller.	44

Figure 4.3	This image shows the variation of the response amplitudes at 100 Hz, 200 Hz, 300 Hz, and 400 Hz to a source with $f_s = 100$ Hz and magnetic field amplitude H_0 . All frequencies examined have peak amplitudes below 8 kA/m with a sudden drop in amplitude between 8 kA/m and 10 kA/m. All signals then increase at 10 kA/m then the even integer frequencies (i.e. $2f_s = 200$ Hz and $4f_s = 400$ Hz) dominate the signal for increasing H_0	45
Figure 4.4	This figure demonstrates the difference in the response of two different initial conditions $\theta_0^{(1)} = 2\pi/3$ and $\theta_0^{(2)} = 2\pi/3.01$. The left image shows the difference of the magnetic moment direction over time for two simulations with the different initial conditions mentioned $\Delta\theta$, the log of the difference $\log \Delta\theta $ to show small scale variation, and the difference between the strain responses $\Delta\lambda_\theta$. The right image shows the amplitude spectra of both strain responses plotted on top of each other.	46
Figure 4.5	Amplitude spectra for two different source frequencies, f_1 and f_2 , are shown in this figure. The amplitude spectra with the same H_0 for each source frequency are shown on the left. There is a clear difference in the amplitude of the source frequency response, double frequency response, and harmonics. The amplitude spectra with the same ratio of f_s/H_0 are shown on the right. The f_1 and f_2 responses are similar with the same amount of significant harmonics.	47
Figure 4.6	A two-dimensional model amplitude spectrum (left) and laboratory amplitude spectrum (right) of the fiber with two Nickel cladding wires and Bragg gratings to a 1.3 kA/m magnetic field ($1 \text{ mT} = 0.79577 \text{ kA/m}$) are shown in this figure. The noise in the lab response is at 60 Hz and is attributable to electrical noise from the building. The base noise level in the laboratory amplitude spectrum is $\sim 10^{-5} \mu\varepsilon$. Note the difference in magnitude scale between the model and laboratory amplitude spectra (the laboratory amplitude spectrum is courtesy of Zachary Dejneka).	48
Figure 4.7	This figure shows a mesh of three-dimensional cells defined in Ubermag (left) and a slice of the model at $z = 0$ nm (right). The slice shows the demagnetized case, with all magnetic dipole moments adding to a net zero moment.	49
Figure 4.8	This figure shows amplitude spectra produced from the three-dimensional model for a magnetized block (left) and demagnetized block (right). The source frequency was 100 Hz with an amplitude of 1.3 kA/m. The demagnetized amplitude spectrum contains lower amplitude peaks than the magnetized amplitude spectrum, closer to the amplitudes seen in the laboratory results for the same magnetic field source, shown in Figure 4.6.	51
Figure 4.9	These plots show the variation of the 100 Hz and 200 Hz peaks for 0.01 A/m to 1.02 A/m (left) and 10 A/m to 98 A/m (right) from three-dimensional model outputs. The orange line in the low field case is indicative of the magnetic field amplitude at which the 100 Hz signal is visible in the model amplitude spectrum. The orange line in the high field case indicates the magnetic field strength at which the 100 Hz signal matches the noise level.	52
Figure 4.10	Changing the damping parameter can result in the appearance of more or less harmonics in the three-dimensional model ($H_0 = 10 \text{ kA/m}$). This figure shows how the amplitudes of the peaks in the amplitude spectrum change based on α (top). Some signal issues appear at certain values of α , producing a random time domain signal, as indicated in the top image. An example random time domain signal is shown in the bottom image.	54

Figure 4.11	These plots show the modeled relationship between temperature and M_s (left), adapted from , and temperature and α (right), adapted from , for nickel.	55
Figure 4.12	The amplitudes of the 100 Hz and 200 Hz peaks in the amplitude spectrum for simulations at different temperatures are shown in this image. The field amplitude was set to 10 kA/m and a source frequency of 100 Hz. There are only small variations in these peak amplitudes from -40°C to 50°C	56
Figure B.1	This figure shows the sandbox experimental setup. Temperature probes are evenly spaced at the top of the box. The solenoid is shown near the bottom of the box. The DMS fiber is buried shallow between the solenoid and temperature probes	103
Figure C.1	This figure shows the Fujikura FSM-70S Fusion Splicer manual alignment screen. Shown on the screen, a DMS fiber is being aligned with an acoustic fiber, with index matching gel applied.	104
Figure C.2	This figure shows an example of what a good alignment, allowing for transmission of light through the fiber, looks like on the OTDR. There should be a peak at the manual alignment position, followed by a steady decrease along the length of the fiber, and a peak at the end of the fiber. The peaks indicate points of greater back-scattering. The lower you can get the first peak with alignment, the better the alignment is.	106
Figure D.1	This figure shows plots of the odd harmonic (top) and even harmonic (bottom) peak amplitudes at increasing magnetic field strength. Magnitude is in units of $\mu\epsilon$	107
Figure D.2	This figure shows how peak amplitudes in the amplitude spectrum change based on the initial angle between the external magnetic field and the magnetization vector, θ_0 in the two-dimensional model. Magnitude is in units of $\mu\epsilon$	108
Figure D.3	This figure shows phase space plots for two different initial conditions in each plot. All images were generated using a source frequency of 100 Hz and magnetic field amplitudes of 0.1 kA/m (top left), 7 kA/m (top right), and 10 kA/m (bottom). θ is in units of radians and $\dot{\theta}$ is in units of radians/s.	109
Figure E.1	This figure shows a borehole model slice of the seawater intrusion model illustrated in Figure 2.2. The borehole model only exposes the water in the borehole to an external magnetic field of $560 \mu T$ in the positive x-direction. The borehole has a square cross-section with side lengths of 0.1 m.	110
Figure E.2	This figure shows a larger version of the same borehole model shown in Figure E.1. The sensors are shown in the center of the borehole with 2 m spacing.	111
Figure E.3	This figure shows the forward modeled TMI anomaly for the borehole seawater intrusion model shown in Figure E.2. This figure shows a cross-section of the borehole at the sensor z location of -0.05 m. The three lines of sensors are shown with a spacing of 2 m. There is a clear difference in TMI anomaly at $x = 0$ m, where the saltwater-freshwater interface is in the model.	111
Figure E.4	This figure shows the TMI anomaly contour value along $y = 0$ m at $z = -0.05$ m in Figure E.3. A difference in TMI anomaly of 0.03 nT is apparent at $x = 0$ m, where the saltwater-freshwater interface is in the model.	112

Figure E.5	This illustration shows the borehole model at $y = 0$ m that was created for magnetic simulation of the complex seawater intrusion model in Figure 2.6. The saltwater is on the left with a gradient in χ towards the freshwater. The χ values from left to right are $\chi_{seawater} = -6.5 \times 10^{-5}$, $\chi_1 = -5 \times 10^{-5}$, $\chi_2 = -4 \times 10^{-5}$, and $\chi_{freshwater} = -3 \times 10^{-5}$	113
Figure E.6	This figure shows the TMI anomaly contour value along $y = 0$ m at $z = -0.05$ m of the forward modeled results from Figure E.5. Differences in TMI anomaly of 0.015 nT, 0.009 nT, and 0.008 nT are apparent at $x = -15$ m, $x = 0$ m, and $x = 15$ m where the gradient changes in salinity are in the model.	113
Figure E.7	This figure shows the borehole model for the mine drainage and lithium brine model. The freshwater is on the left and the metal ion solution of Fe^{2+} or Li^+ is on the right. This image shows the model of an Fe^{2+} concentration of 1000 mg/L.	114
Figure E.8	This figure shows the TMI anomaly contour value along $y = 0$ m of the forward modeled results from Figure E.7. Fe^{2+} concentrations were varied from 0 mg/L to 1000 mg/L.	115
Figure E.9	This figure shows the TMI anomaly contour value along $y = 0$ m of the forward modeled results from Figure E.7. Li^+ concentrations were varied from 0 mg/L to 1500 mg/L.	115

LIST OF SYMBOLS

AC magnetic susceptibility	χ_{AC}
Anisotropy axis unit vector	u
Anisotropy constant	K_1
Cubic anisotropy energy	w_{ca}
Curie constant	C_{mol}
DC magnetic susceptibility	χ_{DC}
Damping parameter	λ
Demagnetization energy	w_d
Demagnetization field	H_d
Domain wall width	l
Effective Bohr magneton	p_{eff}
Effective anisotropy constant	K_{eff}
Exchange constant	A
Exchange energy	w_e
Gilbert damping parameter	α
Magnetic field	H
Magnetic susceptibility	χ
Magnetization	M
Normalized magnetization	m
Saturated magnetization	M_s
Saturated magnetostriction	λ_s
Strain	ε
Total magnetic field energy	E_{tot}
Zeeman energy	w_z

LIST OF ABBREVIATIONS

Alternating Current	AC
Direct Current	DC
Distributed Fiber Optic Sensing	DFOS
Distributed Magnetic Sensing	DMS
Landau-Lifshitz-Gilbert	LLG
Pollution Load Index	PLI
Potentially Toxic Elements	PTEs
Seawater Mixing Index	SMI
Superconducting Quantum Interface Devices	SQUID
Total Dissolved Solids	TDS
Total Magnetic Intensity	TMI
Transient Electromagnetics	TEM
parts per million	ppm
parts per thousand	ppt

ACKNOWLEDGMENTS

We thank the sponsor companies of the Center for Wave Phenomena, the DOE Office of Fossil Energy grant DE-FE0091786, and the DOE Office of SBIR/STTR Programs grant DE-SC0023984 for financial support. We thank Mines RC for computing resources, and Sentek Instrument, LLC for use of the DASNova interrogator. The analyses and plots in this thesis were produced using Matlab, Matplotlib, NumPy, DASDAE, Ubermag, OOMMF, and SimPEG. ChatGPT (October 20 Version) was used to check grammar in this thesis. We would like to thank Josh Moses in the Physics department at Colorado School of Mines for providing valuable help with developing the electronic components required to run lab tests. We would also like to thank Brian Passerella for assisting us in carrying out field experiments.

I would like to thank my advisor, Dr. Eileen Martin, for all the valuable guidance she has provided me and the patience she has had when I was struggling. She has been an amazing advisor and I am happy to have been a research assistant for her. I would also like to thank my committee members, Dr. Kamini Singha and Dr. Yaoguo Li, for their guidance on the direction of my thesis. Zachary Dejneka and Dr. Daniel Homa were excellent to work with, provided me with laboratory data that guided modeling efforts, and greatly increased my understanding of how the DMS fiber works. Dr. Shihao Yuan has been an excellent colleague and helped me greatly in the analysis and collection of field and laboratory data discussed in this thesis.

CHAPTER 1

INTRODUCTION

Distributed magnetic sensing (DMS) is a new technology involving the use of magnetic sensing and distributed fiber optic sensing (DFOS) principles that can be applied in multiple contexts and that we aim to apply to the field of hydrogeology. This chapter provides background information for the research into DMS that is discussed in this thesis.

1.1 Applications of Magnetic Methods

Magnetic fields are produced by moving electric charges, permanent magnets, electromagnets, and changing electric fields. Common examples of these sources include electric currents, refrigerator magnets, generators, and antennae, respectively. One example of a magnetic field source in nature is the Earth. The Earth produces a magnetic field via the movement of electric charges within the outer core, making it a large electromagnet. This magnetic field can magnetize minerals that contain iron (such as magnetite) during their formation period. As these magnetic minerals cool during formation, they maintain their magnetization due to the Earth's magnetic field - this phenomenon is called paleomagnetism.

Geophysical magnetic methods can map magnetized minerals by identifying anomalies from the expected background field, which is Earth's magnetic field. These anomalies can be detected in total magnetic intensity (TMI) anomaly maps, as shown in Figure 1.1. In real applications, magnetic sensors can be aerial or ground-based to produce TMI anomaly maps. Magnetic sensors are also used to detect changes and anomalies in the Earth's magnetic field. For more information on geophysical magnetic methods, refer to Kaufman *et al.* (2009).

Magnetic methods in geophysics have traditionally been implemented to provide information for geologic mapping of regions, guidance for mining, detection of buried metallic objects, mapping basement structure for oil and gas exploration, understanding groundwater aquifer structure, and more (Nabighian *et al.*, 2005; Paterson & Reeves, 1985). These methods make use of Earth's magnetic field, the magnetic field produced by certain minerals, or magnetic fields from controlled sources to determine the magnetic susceptibility χ of subsurface materials. χ is a material property that determines how much a material will become magnetized when exposed to a magnetic field. Since χ varies between materials, knowledge of this property can aid in determining rock type. χ is defined as the ratio of magnetization M to applied magnetic field H (Cullity & Graham, 2009),

$$\chi = M/H. \tag{1.1}$$

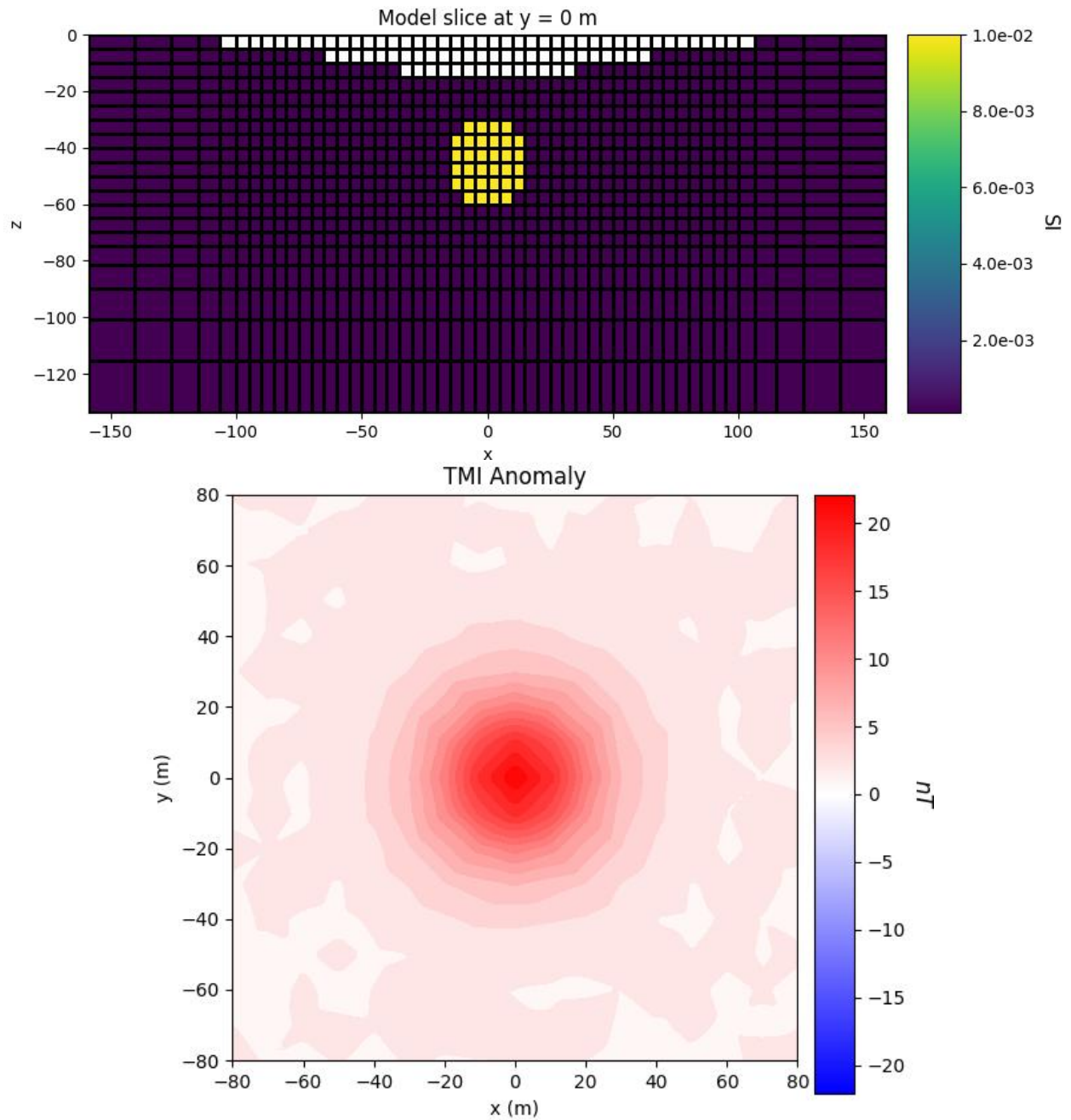


Figure 1.1 This figure shows what a magnetic anomaly looks like in aerial data captured 10 m above the surface due to a spherical block of a magnetic mineral in the subsurface. The block is centered at $x = 0$ m and $y = 0$ m with a radius of 15 m and a depth of 50 m (top). The simulated data created using SimPEG is shown in the bottom image (Cockett *et al.*, 2015).

In environmental applications, alternating current (AC) magnetic susceptibility χ_{AC} is typically used rather than direct current (DC) magnetic susceptibility χ_{DC} , which is the more traditionally used measurement in geophysics. Alternating magnetic fields are used to determine χ_{AC} , whereas constant magnetic fields are used to determine χ_{DC} . The measurement of χ_{AC} provides certain advantages over the measurement of χ_{DC} (Topping & Blundell, 2018). Additionally, χ_{AC} is effective in the detection of fine-grained magnetic molecules in samples (Kodama, 2010) and is well-suited for applications to water (Gutiérrez-Mejía & Ruiz-Suárez, 2012).

Magnetic susceptibility methods as a proxy for environmental pollution levels is a relatively newer application of the geophysical property. The application of magnetic susceptibility to environmental problems has been developing for the past ~ 25 years, with its main application in soil pollution, e.g. Bityukova *et al.* (1999); Kruglov & Menshov (2017); Petrovský *et al.* (2000). The typical methods for determining soil χ_{AC} involve the use of instruments such as the Kappabridge MFK2 and Bartington MS2, e.g. Ji *et al.* (2023); Kanu (2014); Kruglov *et al.* (2022); Schmidt *et al.* (2005). These instruments apply an alternating magnetic field to a sample and measure the induced magnetic moment, allowing calculation of χ_{AC} (Thompson & Oldfield, 1986). In a recent application to groundwater, AC methods were used to measure χ_{AC} of saline water samples in the lab (Kumar *et al.*, 2022; Rana *et al.*, 2021).

In Magiera *et al.* (2018), it was demonstrated that soil χ_{AC} has a high correlation with total iron content surrounding the Bjørnevatn iron mine in Norway and a statistically significant positive correlation with potentially toxic elements (PTEs) such as Ni, Cu, Cr, Se, Co, As, Zn, and Cd surrounding an Ni-Cu smelter in Nikel, Russia. In another study, χ_{AC} was shown to be an effective tool for determining concentrations of Zn, Pb, Fe, Cr, Ni, Cu, and the overall pollution load index (PLI) due to industrial activities and heavy traffic in Denizli, Turkey (Oudeika *et al.*, 2020). Additionally, χ_{AC} has been shown to correlate with PTE concentrations within mine tailings (e.g. Pb and As) in the Tlalpujahuá and El Oro Mining Districts in Mexico (Morales *et al.*, 2016). Correlation of χ_{AC} with certain metal concentrations within copper mine tailings (e.g. Cr, Fe, Ni, and Cu) was demonstrated in the Atacama Desert, located in Antofagasta Region, Chile (Lam *et al.*, 2020).

Applications of magnetic susceptibility methods to groundwater studies are relatively new, with only a few recent studies on the topic of seawater intrusion. However, χ_{AC} of water is measurable and changes based on the concentration of NaCl in the water (Gutiérrez-Mejía & Ruiz-Suárez, 2012). When applied to groundwater samples, bulk χ_{AC} has been shown to have a linear relationship with salinity (Rana *et al.*, 2021), demonstrating its potential utility in application to saltwater intrusion problems. In Rana *et al.* (2021), it was also shown that the water samples taken near Digha, in Contai Subdivision, Purba Medinipur District, West Bengal, India indicated decreasing salinity from bulk χ_{AC} analysis in wells

further from the ocean which was also in agreement with conductivity analysis performed on the samples. Another study in the coastal regions of Digha, Shankarpur, Tazpur, and Mandarmani (DSTM) in the East Medinipur District, West Bengal, India, demonstrated that χ_{AC} measurements have an inverse relation with salinity, conductivity, total dissolved solids (TDS), Cl^- ion concentration, seawater mixing index (SMI), and isotopes ($\delta^2\text{H}$ and $\delta^{18}\text{O}$). These were shown to be an effective proxy to delineate seawater intruded zones (Kumar *et al.*, 2022).

While the previous applications of magnetic susceptibility methods to groundwater studies have been limited to seawater intrusion problems, properties of contaminated soils suggest there is a possibility to utilize χ_{AC} for monitoring PTE groundwater concentrations in mining and urban environments. This idea is further supported by the finding that an inverse relationship exists between χ_{AC} and TDS (Kumar *et al.*, 2022). Additionally, it has been shown that iron ions change χ_{AC} of water when exposed to intensive magnetic fields (Orlyuk *et al.*, 2022). It is known that certain PTEs (e.g. Cd, Zn, Cu, and Pb) can leach into groundwater from the soil given the right soil conditions (Wang *et al.*, 2024). Suppose these ions are detectable in groundwater via magnetic susceptibility methods as they are in soils. In this case, the detection of mobile heavy metals may be another application of magnetic susceptibility in hydrogeology.

Current magnetic sensors used in geophysics range in sensitivity based on their design. Typical low-cost, miniaturized, and lightweight sensors that are used for collecting airborne magnetic data have sensitivities ranging from 0.1 nT to 100 nT. The most sensitive detectors are superconducting quantum interface devices (SQUID), which have sensitivities of about 2×10^{-5} nT for a bandwidth of 10 Hz (Accomando & Florio, 2024). The Kappabridge MFK2, discussed earlier in this section, can sense magnetic susceptibilities down to 2×10^{-8} (SI), this sensitivity is defined on its webpage. These typical sensitivities are important considerations when determining the sensitivity requirements of the DMS fiber.

1.2 Distributed Fiber Optic Sensing

Distributed fiber optic sensing (DFOS) is a collection of geophysical sensing methods that are capable of continuous monitoring over a length of optical fiber (Hartog, 2018). Three major advantages of DFOS compared to traditional geophysical surveys include increased sensor density, the ability to perform continuous monitoring with a deployed fiber, and ease of long-term deployment compared to other survey methods (Hartog, 2018). These advantages present a compelling reason to further develop fiber to be compatible with other imaging methods, such as magnetics.

One example application of DFOS is distributed acoustic sensing (DAS), which is the use of fiber to sense acoustic waves in the subsurface. Setting up DAS surveys typically involves connecting an optical fiber to an interrogator - a box that converts the fiber signal to strain or strain rate - then laying the fiber

out along the desired survey line (e.g. shallow trench, borehole, etc.). During surveys, acoustic waves travel from a source (e.g. vibration trucks, earthquakes, borehole drilling, etc...) to the fiber. When the acoustic wave reaches the fiber, the fiber is stretched parallel to the direction of travel of the wave (P-wave) or perpendicular to the wave travel direction (S-wave). The stretch in the lengthwise direction of the fiber changes the distance the light must travel in the fiber before it is scattered back to the interrogator, creating a signal in the interrogator.

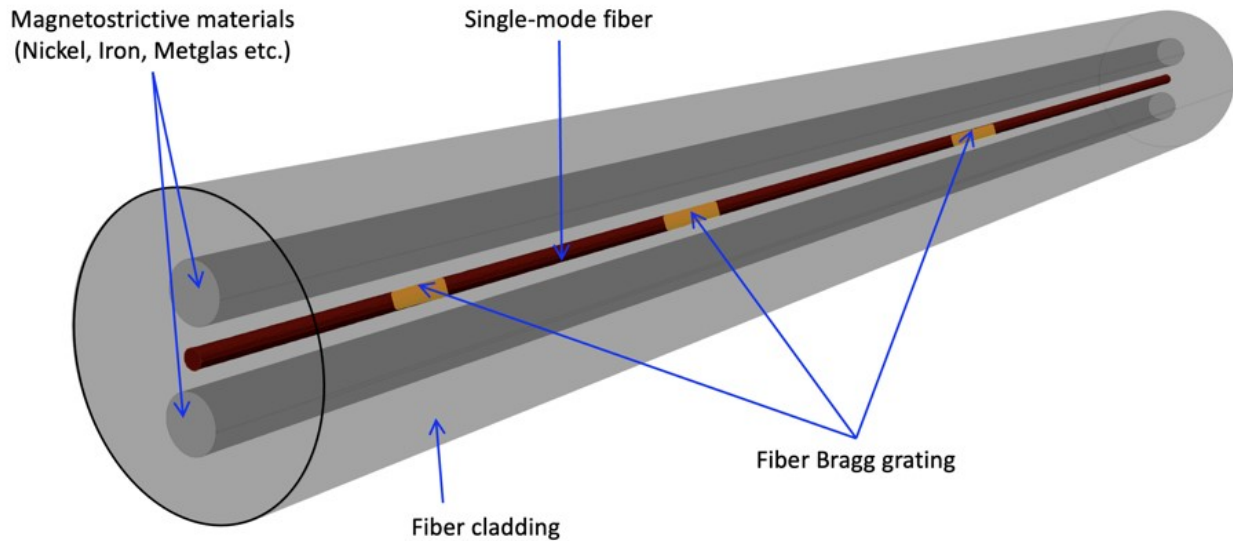


Figure 1.2 A schematic illustration of the distributed acoustic and magnetic sensing fiber is shown in this image. This illustration shows a fiber with two rods of magnetostrictive material, however, other fiber configurations have been created and tested (Hileman *et al.*, 2022).

The interrogator in DAS applications uses fiber optic principles to image sources that cause a lengthwise strain on the fiber. DAS measures the phase shift of light by sending pulses of light down the length of a fiber-optic cable, which are scattered back to the interrogator at imperfections in the glass or at Bragg gratings within the fiber (which increase the amount of light sent back to the interrogator), then uses an interferometer inside the interrogator to measure the light phase shift over a specified length of fiber called the gauge length (Hartog, 2018). From the phase shift, strain can be calculated using a linear relationship based on the materials used in the fiber.

DAS fibers can be installed in vertical or horizontal boreholes to perform seismic monitoring. In horizontal borehole deployments, surveys have been performed with and without cemented borehole casings, with at least one experimental test suggesting that borehole casings are not necessary for seismic monitoring surveys with DAS (Follett *et al.*, 2016). The application of horizontal directional drilling (HDD) in electrical and telecommunications industries targeting the top three meters of the subsurface has

seen growth in recent years, suggesting future possibilities for low-cost HDD (Allouche *et al.*, 2000; Yan *et al.*, 2018). Ongoing efforts to improve HDD and reduce the costs and risks of this type of drilling are a current topic of research (Krechowicz, 2020; Rakshith *et al.*, 2023). Application of DAS in shallow geothermal heat pumps (8 m depth and 63 m length) has also been implemented, pointing to the feasibility of long, shallow horizontal boreholes (Mohammadzadeh Bina *et al.*, 2020).

The goal of our work is to understand and use a DFOS magnetic field measurement method. Distributed magnetic sensing (DMS) is a novel technology that combines the existing capability of DAS with novel fiber-optic cables that respond to magnetic fields (Dejneka *et al.*, 2024; Hileman *et al.*, 2022). This is accomplished through coupling a fiber-optic cable to a magnetostrictive material (i.e. a material that experiences a strain when exposed to external magnetic fields), illustrated in Figure 1.2. When the magnetostrictive material expands or contracts, illustrated in Figure 1.3, a strain is induced in the fiber-optic cable, and that strain on the cable can then be measured using DAS measurement principles, e.g. Bao & Chen (2012) and Martin *et al.* (2021). The fiber-optic magnetic sensing design that we focus on in this paper is described along with initial laboratory tests in Hileman *et al.* (2022). In addition to responding to magnetostriction-induced strain, the measurements also respond to other sources of strain, e.g. temperature-related expansion or contraction (Ukil *et al.*, 2012) and mechanical strains (Shang *et al.*, 2022), so quantitative modeling of these new fiber-optic material responses is critical to data analysis and interpretation.

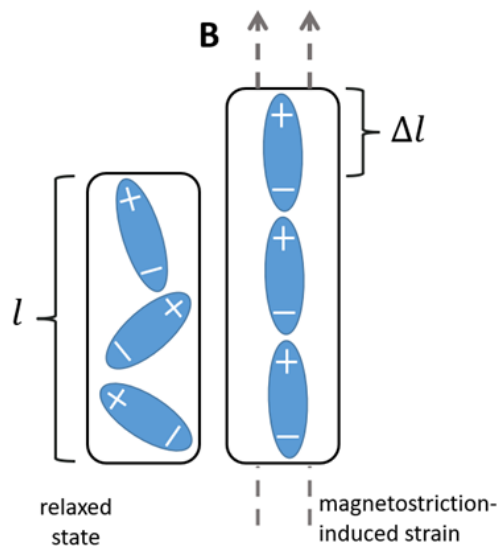


Figure 1.3 This image illustrates a change in length Δl of a magnetostrictive material due to an external magnetic field. Δl can represent an increase or decrease in length depending on material properties (image adapted from Pérez-Aparicio & Sosa 2004).

1.3 Ferromagnetism and Magnetostriction

Ferromagnetism is a phenomenon where a material is broken up into domains of magnetization within the material (Cullity & Graham, 2009). Domains are regions in the material wherein all the atoms have magnetic moments pointing in the same direction. Because the material is broken up in this way, all domains have magnetization magnitudes of the saturation magnetization value M_s , which is a material property. When all domains point in the same direction, the bulk material is considered saturated and has a magnetization of M_s .

Magnetostriction is the strain induced in a ferromagnetic material (e.g. iron, nickel, cobalt) by an effective magnetic field, \mathbf{H}_{eff} , which includes the applied magnetic field and fields generated within the material (Cullity & Graham, 2009). When a ferromagnetic material is in an ideal demagnetized state (i.e. all magnetic domain magnetization directions cancel each other out), the material exhibits a net zero external magnetic field. When an external magnetic field \mathbf{H} is applied to the material, the domain magnetic moments \mathbf{M} experience a torque per volume which aligns the overall magnetic moment of the material in the direction of \mathbf{H} if $\|\mathbf{H}\|$ is large enough to saturate the material. The Landau-Lifshitz-Gilbert (LLG) equation,

$$\frac{d\mathbf{M}}{dt} = \gamma^*(\mathbf{M} \times \mathbf{H}_{eff}) - \frac{\alpha}{M} \left(\mathbf{M} \times \frac{d\mathbf{M}}{dt} \right), \quad (1.2)$$

describes the dynamics of the total magnetic moment of a ferromagnetic material (Gilbert, 2004; Wieser, 2015), accounting for damping of the domain motion. Figure 1.4, demonstrates this magnetization process. In Equation 1.2, the constant $\gamma^* = \gamma(1 + \alpha^2)$, with $\gamma = \frac{ge}{2mc}$, where e and m are the charge and mass of the electron, c is the speed of light, and g is the spectroscopic splitting factor ($g = 2$ for electron spin); and the damping term $\alpha = \lambda/\gamma M$, where λ is an adjustable damping parameter. Note that $M = \|\mathbf{M}\|$ in Equation 1.2.

In materials that exhibit magnetostriction, the cubic crystal structure is not perfectly cubic (e.g. slightly tetragonal or rhombohedral) so the material undergoes a change in length Δl , and a subsequent strain $\lambda_s = \Delta l/l$, when the domains are reoriented. The strain experienced by a material with an anisotropic cubic crystal structure when magnetized from the ideal demagnetized state to saturation in the direction defined by the direction cosines α_1, α_2 , and α_3 (representing a normalized 3D vector) and measured in the direction defined by the direction cosines β_1, β_2 , and β_3 relative to the crystal axes is

$$\lambda_s = \frac{3}{2}\lambda_{100} \left(\alpha_1^2\beta_1^2 + \alpha_2^2\beta_2^2 + \alpha_3^2\beta_3^2 - \frac{1}{3} \right) + 3\lambda_{111}(\alpha_1\alpha_2\beta_1\beta_2 + \alpha_2\alpha_3\beta_2\beta_3 + \alpha_3\alpha_1\beta_3\beta_1), \quad (1.3)$$

where λ_{100} and λ_{111} are the saturation magnetostrictions in the [100] and [111] crystal directions (Cullity & Graham, 2009). Assuming the magnetostriction of the material is isotropic simplifies Equation 1.3 to

$$\lambda_\theta = \frac{3}{2}\lambda_s \left(\cos^2 \theta - \frac{1}{3} \right), \quad (1.4)$$

where λ_s is the isotropic saturation magnetostriction and θ is the angle between the measurement direction and the saturated direction. While magnetostriction is typically not isotropic in materials, approximating the response as isotropic works well for materials with anisotropic magnetostrictions close in value. For example, nickel has saturation magnetostriction values $\lambda_{100} = -46 \text{ ppm}$, $\lambda_{111} = -24 \text{ ppm}$, and $\lambda_s = -34 \text{ ppm}$ (Hileman *et al.*, 2022) - the negative sign indicates a decrease in length in the direction of magnetization.

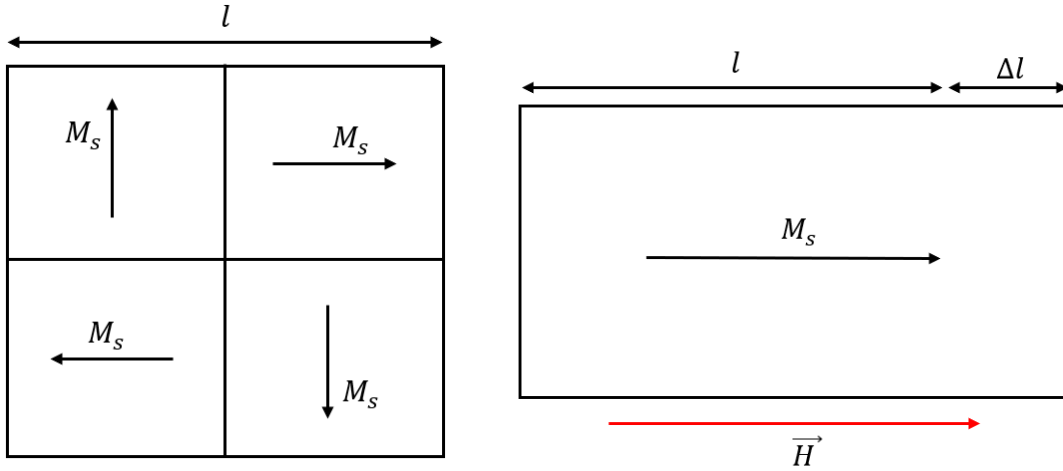


Figure 1.4 The domains within a ferromagnetic material are sections of magnetic saturation M_s , with magnetization vectors oriented in different directions. The net magnetic field outside the material due to the internal magnetic moments is zero when not magnetized by an external magnetic field (left). When a magnetic field \vec{H} is applied to the material, the magnetic dipoles align in the direction of the external field, causing a change in length Δl (right).

Computational modeling of the DMS fiber response to alternating external magnetic fields has not been performed prior to this work. It is valuable to fill this gap to provide an understanding of the mechanism behind the fiber response, survey design capabilities, signal separation tools, and geophysical inversion of data. There are multiple open-source software for modeling micromagnetic systems that implement different numerical methods to solve for the dynamics of the magnetic moments within materials (Abert, 2019). For the three-dimensional model, we make use of Ubermag (Beg *et al.*, 2022), which allows the micromagnetic modeling algorithm from the software OOMMF (Donahue, 1999) to be implemented in Python (Van Rossum & Drake, 2009). With OOMMF, it is possible to run simulations of micromagnetic responses to alternating and static magnetic fields using finite element methods. Including magnetostriction

calculations in the simulations, the program can solve for the approximate DMS fiber response.

1.4 DMS Application Background

We explore three potential application areas of the DMS fiber in this paper. This section provides an overview of three possible applications: seawater intrusion, mine drainage into groundwater, and lithium brine mining.

1.4.1 Seawater Intrusion

Seawater intrusion is one of the main threats to freshwater resources in coastal areas around the world, especially in arid regions where groundwater pumping rates are higher than the natural recharge rates (Cao *et al.*, 2021; Hussain *et al.*, 2019). The interface between seawater and freshwater is given by the Ghyben–Herzberg relation under hydrostatic conditions,

$$z = \frac{\rho_f}{\rho_s - \rho_f} h, \quad (1.5)$$

where ρ_s is the density of seawater, ρ_f is the density of freshwater, z is the depth of the interface below seawater level, and h is the height of the freshwater table above mean sea level (Anderson *et al.*, 2015). In real applications, mixing occurs between the seawater and freshwater at the interface, creating a transition zone rather than a sharp interface, as illustrated in Figure 1.5. Seawater intrusion occurs when the interface migrates inland due to high groundwater pumping rates or other aquifer stressors.

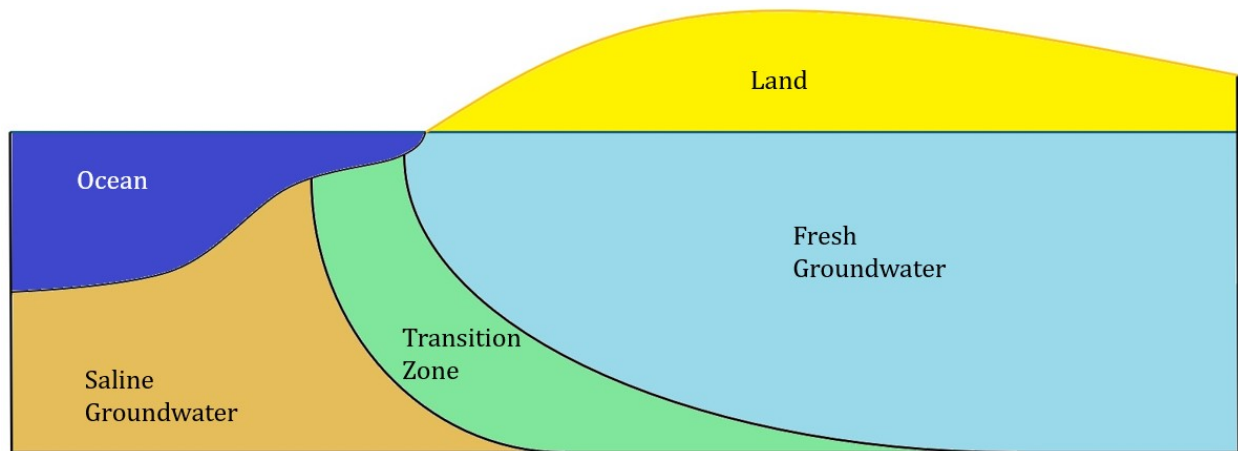


Figure 1.5 This illustration shows a typical saltwater-freshwater interface in seawater intrusion. The transition zone is a mix of saltwater and freshwater (adapted from Costall *et al.* 2020).

Monitoring methods of seawater intrusion rely on wells for chemistry and water level information, which is required for the development of groundwater models (Costall *et al.*, 2020). Geophysical methods such as electrical conductivity/resistivity, seismic, and transient electromagnetics (TEM) have been applied to

assist in monitoring seawater intrusion (Ez-zaouy *et al.*, 2023; Hasan *et al.*, 2020; Tarallo *et al.*, 2023). Magnetic susceptibility methods have only recently been applied to monitor seawater intrusion with some success (Kumar *et al.*, 2022; Rana *et al.*, 2021). A method with higher spatial resolution and the ability to perform time-lapse monitoring would improve monitoring capability.

1.4.2 Mine Drainage

Mine drainage is characterized by high concentrations of SO_4^{2-} , metals, and metalloids. Metals that are typically produced in mine drainage include Fe^{2+} and Cu^{2+} among others. Sources of mine drainage include old mine workings from abandoned mines and mine waste deposits. Groundwater pollution caused by mine drainage from these sources poses environmental concern worldwide (Tomiyaama & Igarashi, 2022). In the United States, limits on groundwater concentrations of certain metals are imposed by the United States Environmental Protection Agency (EPA).

Monitoring of mine drainage in groundwater requires analysis of the chemical composition and concentration of organic and inorganic constituents within groundwater samples (Skousen & Jacobs, 2014). If a contaminant concentration is higher than acceptable limits, all potential sources contributing to the pollution have to be identified. Electromagnetic and electrical resistivity geophysical methods have been used to help in the identification of mine drainage sources (Moreira *et al.*, 2020; Power & Almpanis, 2022). A geophysical method that is easier to set up and provides higher spatial resolution than those currently implemented would be valuable in mine drainage monitoring.

1.4.3 Lithium Brine Mining

Lithium demand has increased greatly in recent years, largely due to the increased production of lithium-ion batteries (Tabelin *et al.*, 2021). Projections indicate that demand for lithium in 2040 will be up to eight times the production amounts of 2023 (Maisel *et al.*, 2023). Much of the world’s lithium comes from the South American “Lithium Triangle”, with reports in 2021 indicating 56 percent of the world’s potential lithium resources are located in Argentina, Bolivia, and Chile (Fornillo & Lampis, 2023). The high altitude of the lithium resources in these regions promotes evaporation, leading to high lithium concentrations in brines. Examples include Salar de Olaroz and Salar del Hombre Muerto in Argentina which contain 620-690 mg/L of Li^+ while the concentration in Salar de Atacama of Chile is ≈ 1500 mg/L (Tabelin *et al.*, 2021). The U.S. also has approximately 20 lithium mine sites with past production greater than 15,000 metric tons (Karl *et al.*, 2019).

The mining process for lithium brines involves drilling boreholes into the aquifer and pumping the brine into evaporation pools on the surface. Selected recovery of Li^+ is achieved after the brine has been purified

of other ions such as Na^+ , K^+ , Ca^{2+} and Mg^{2+} (Tabelin *et al.*, 2021). Brine characterization methods involve surface water sampling, digging shallow pits, and geophysical methods (Cabello, 2021). Some geophysical methods that have been shown to be effective in brine exploration and monitoring include magnetotellurics, electrical resistivity tomography, and gravity surveys (Curcio *et al.*, 2024). Magnetic methods have not been applied to lithium brine characterization or monitoring in the literature.

1.5 Laboratory Experiment Background

Laboratory experiments are described in this thesis to determine current DMS functionality. Experiments were performed by sending alternating current through a solenoid to produce an alternating magnetic field, causing magnetostriction to occur in the fiber. Solenoids are coils of wire, Figure 3.1, that produce magnetic fields when current is sent through them. The magnetic field within a solenoid follows the equation

$$B = \frac{\mu_0 NI}{L} \quad (1.6)$$

where μ_0 is the permeability of free space, N is the number of turns in the solenoid (≈ 450 in our experiments), I is the current, and L is the length of the solenoid (Cullity & Graham, 2009). Outside of the solenoid, the magnetic field is theoretically zero; however, in practice it is non-zero, but is still orders of magnitude smaller than the magnetic field at the center of the solenoid. When an AC current is applied to a solenoid, the power depends on impedance. Since the impedance of a solenoid is proportional to the signal frequency, a current amplifier was required to produce a strong enough magnetic field for the fiber to sense at different frequencies.

1.6 Field Experiment Background

Field experiments are described in this thesis, which use transient electromagnetics (TEM) as a magnetic field source for the fiber to respond to. TEM is a geophysical method where a single transmitter loop is set up in a large square (typically 40m x 40m or 20m x 20m for the ABEM WalkTEM) and a smaller receiver loop (0.5m x 0.5m with 20 internal turns for the ABEM WalkTEM) is placed in the center of the transmitter loop. Our goal was to determine if the fiber responds to a typical geophysical method as a source. Current pulses are sent through the large loop to produce a magnetic field which is sent into the subsurface. The magnetic field then produces a weaker current in the subsurface with a larger area in the opposite direction of the current of the transmitter loop. The generated subsurface current loop then produces another current loop below that loop which is weaker, in the opposite direction, and of larger area. This current induction continues until the magnetic field is of negligible value in the subsurface to produce any significant current. The current from the transmitter is then switched off and the decay of the

magnetic field produced by the current in the subsurface is measured by the TEM receiver. When inverted, the decay time is used to calculate resistivity (Kirsch, 2006).

1.7 Motivation and Thesis Layout

The motivation behind this thesis is to provide an understanding of the physical mechanisms of DMS and understand the potential of the new technology for applications in hydrogeology.

Chapter two discusses the applications of DMS to selected problems in hydrogeology. In particular, the application of DMS for monitoring seawater intrusion, mine drainage, and lithium brine monitoring. The layout of the potential survey is discussed and a simulation is provided as preliminary proof of concept, providing an initial indication that the method could be viable. However, further testing will be required for comprehensive validation of the proposed approaches.

Chapter three discusses lab and field experiments used to determine the magnetic field sensitivity of the DMS method and its potential application with a current geophysical source. The lab experiments were performed on a fiber without Bragg gratings, using a standard DAS interrogator to determine differences in sensitivity from the Bragg grating method used by Hileman *et al.* (2022) and Dejneka *et al.* (2024).

In chapter four, computational modeling of DMS is discussed as a method of understanding the physical mechanism of DMS. Two-dimensional and three-dimensional models of the ferromagnetic material are utilized to bolster the knowledge of the DMS fiber.

In the final chapter, conclusions and future research avenues are discussed.

CHAPTER 2
FEASIBILITY OF DMS FOR HYDROGEOLOGIC PROBLEMS

Current environmental magnetic susceptibility methods involve taking samples at single points, limiting the spatial coverage of surveys. Using DMS to monitor salt and PTE concentrations in these cases could allow for higher spatial coverage and resolution than current methods as well as continuous coverage over time or time-lapse studies. This chapter covers potential applications of DMS and simulations of the applications. The code used for these simulations is provided in Appendix A. An updated version of the modeling discussed in this chapter is provided in Appendix E.

2.1 Groundwater Solution Monitoring Methods

The DMS fiber has never been applied before, creating a necessity for application design and simulation. In this section, potential applications and feasibility evaluations are discussed.

2.1.1 Design of Application

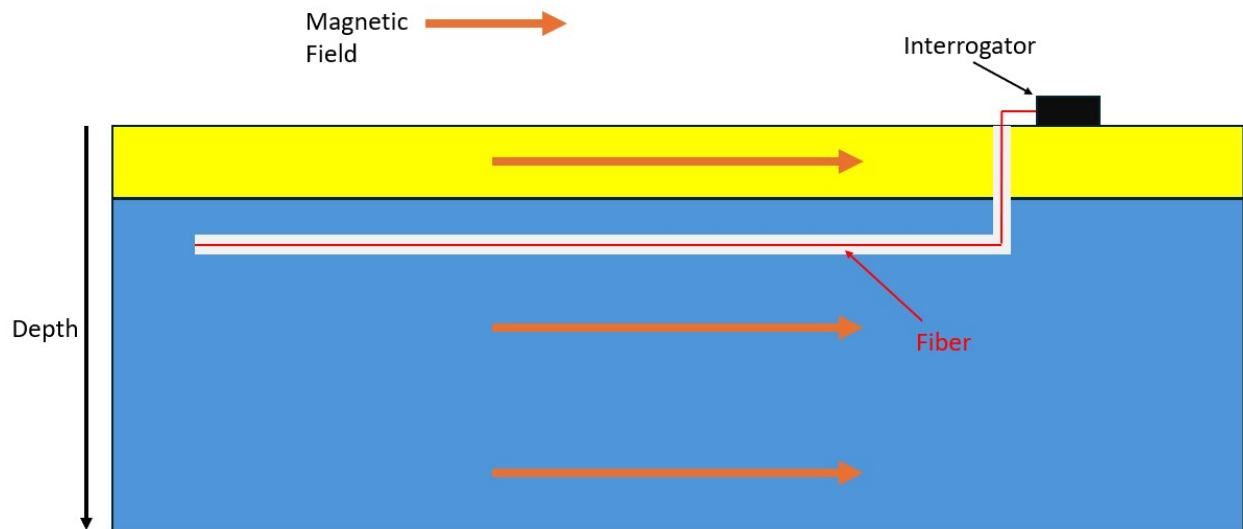


Figure 2.1 This figure shows a simple model of an application of the DMS fiber, wherein the DMS fiber is buried within the borehole and a magnetic field is applied to the whole block model. The unsaturated zone is yellow and the saturated zone is blue in this image.

Potential applications include horizontal time-lapse monitoring of seawater intrusion, mine drainage, and lithium brines. Consider a simple scenario in which a horizontal fiber is installed in a slim borehole that is allowed to collapse back on itself (so the fiber is embedded in the soil), then a constant magnetic

field is applied throughout the entire volume of interest, illustrated in Figure 2.1. Advances in drilling such slim, horizontal boreholes have made these more affordable than in the past, as discussed in section 1.2. If there is a horizontal change in χ_{AC} of the water, it would be possible to capture it using this method. Changes in the water solution such as a change in salinity, TDS, Cl^- concentration, or isotope concentration have been shown to cause such changes in χ_{AC} (Kumar *et al.*, 2022). We hypothesize that to most effectively monitor these changes, the horizontal borehole should be placed along the profile where the water solution gradient is the steepest. This would allow the DMS fiber to capture the largest differences in χ_{AC} and have the clearest signal to capture changes in the water solution.

2.1.2 Simulation

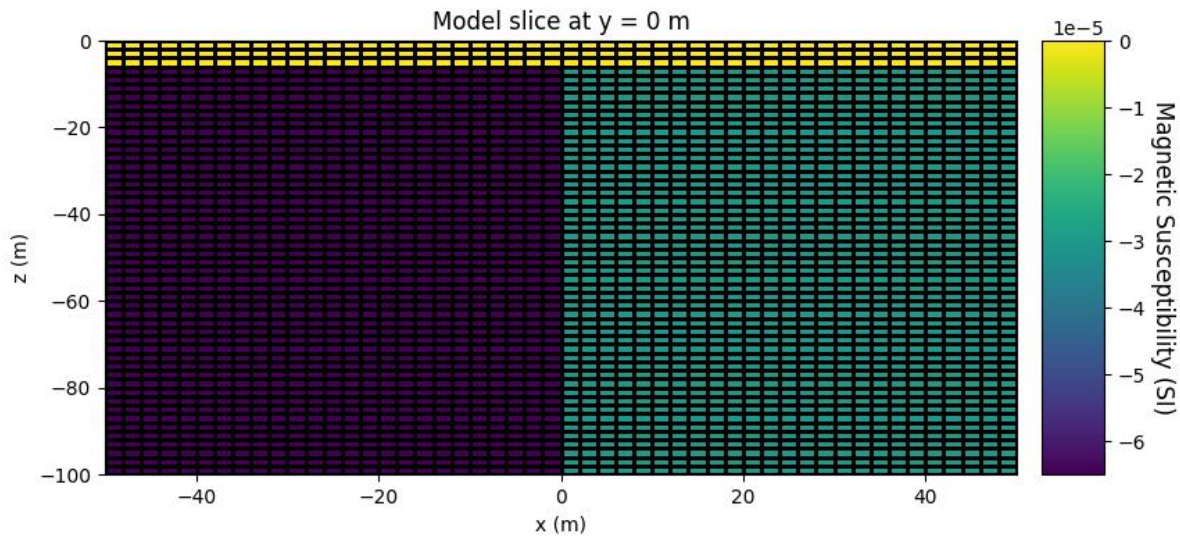


Figure 2.2 This illustration shows a simple subsurface model slice at $y = 0$ m that was created for magnetic simulation forward modeling of a simple seawater intrusion boundary. There are two blocks of different χ values (purple and green) representative of water with different solutes. These blocks are placed below five meters to represent a water table with dry soil on top (yellow layer).

Simulations were performed using the SimPEG magnetics module (Cockett *et al.*, 2015). In these simulations, a three-dimensional subsurface model of magnetic susceptibility is defined with a specified uniform magnetic field direction. The two-dimensional total magnetic intensity (TMI) anomaly data is computed using forward modeling of the subsurface model and specified sensor locations. This study focuses on changes in the expected data due to model changes, but further analysis could be carried out on the sensitivity of inversions of these data.

There are a few limitations of the SimPEG simulation package. Future modifications of the software could enable more realistic simulations. These simulations are not capable of applying an alternating

magnetic field to the subsurface. This means that the model uses values of χ_{DC} , however, some experimentally determined water χ_{AC} values are used for model setup. The applied magnetic field also must be applied to the whole subsurface model, not just inside the borehole, which would have to be the limit of application with available magnetic field sources (Appendix D provides a potential solution to this issue). Finally, multiple sensor lines were added to the model since the inversion package expects two-dimensional sensor arrays. Due to these limitations, the simulations are not used as a comprehensive proof of concept, but rather to indicate the potential viability of such surveys and a motivation for future simulations to more accurately design such surveys. These simulations may also be useful in providing support for improving the ability of DMS fiber sensing interrogators to measure DC magnetic responses.

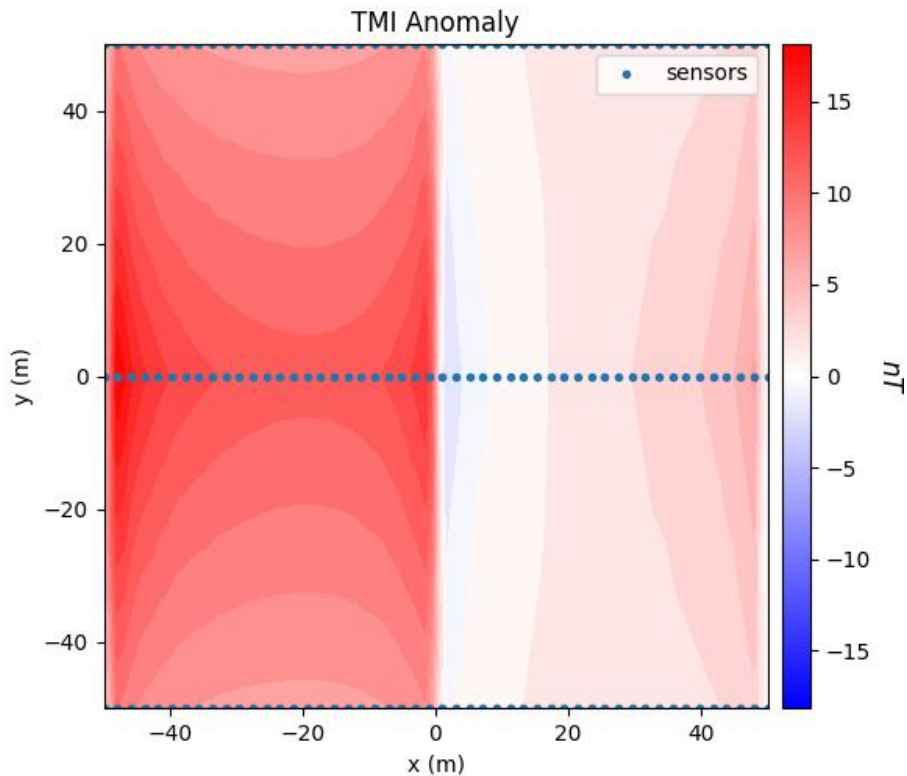


Figure 2.3 The forward modeling results of Figure 2.2 are shown in this image. The sensors are ten meters deep and are placed two meters apart to model the Bragg grating spacing of the DMS fiber. This image is a two-dimensional slice at the sensor depth of 10 m. There is a clear shift of 17 nT in the value of the TMI anomaly visible at the interface between the saltwater and freshwater.

In these simulations, a simple model with two blocks of different magnetic susceptibility was created with an upper interface five meters below the surface to simulate a water boundary with different solutes in the water on either side of the vertical boundary. Three lines of sensors were used with sensors placed two meters apart in each line to simulate the channel spacing of the Bragg grating fiber. The sensors were

placed below the water table, at the water table, and above the water table in the simulations. The horizontal location of the boundary was also changed to determine the system sensitivity to the location of the change in the water solutes. The magnetic field was applied along the length of the sensor lines with a magnitude of $560 \mu\text{T}$, which is a magnetic field strength that can be produced by common magnetic field sources. The simulation subsurface setup is illustrated in Figure 2.2. For all simulations, the yellow block was assigned $\chi_{soil} = 1 \times 10^{-5}$, a typical value for paramagnetic soils (Shirzaditabar & Heck, 2021).

2.2 Seawater Intrusion Modeling

SimPEG was used to create models of seawater intrusion. Two models, one simple and one more realistic, are modeled and discussed in this section. The simulations in this section only consider salinity to have an effect on χ_{DC} .

2.2.1 Simple Model

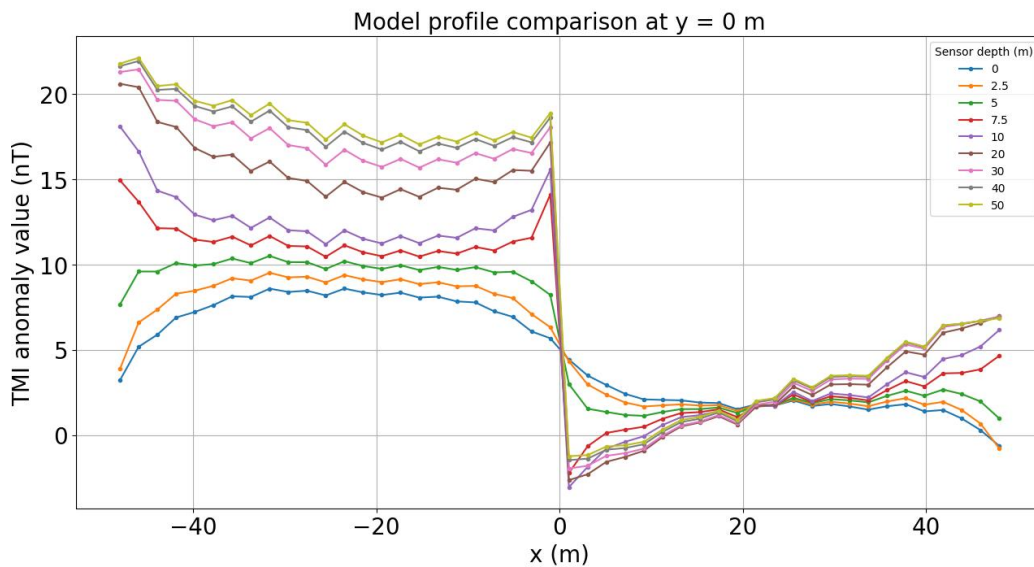


Figure 2.4 The profiles at $y = 0 \text{ m}$ of the forward modeled TMI anomaly data slice at the sensor depth, with sensors at different depths are shown in this illustration. For these models, the boundary between the saltwater and freshwater blocks was placed at $x = 0 \text{ m}$. The water table is at a depth of 5 m . We see this reflected in the simulations as the boundary resolution improves greatly when the sensors are placed below the water table at a depth of 7.5 m and deeper.

In the seawater intrusion simulation, the seawater is the purple block in Figure 2.2 with $\chi_{seawater} = -6.5 \times 10^{-5}$ (50 ppt salinity) and the freshwater is the teal block with $\chi_{freshwater} = -3 \times 10^{-5}$ (Rana *et al.*, 2021). Note that water has a negative magnetic susceptibility, indicative of its diamagnetic nature which can change based on magnetic field frequency (Gutiérrez-Mejía & Ruiz-Suárez, 2012). The

forward modeled TMI anomaly data with the sensors at a depth of ten meters is shown in Figure 2.3. There is a clear change in the value of the TMI anomaly seen in the resulting data at the boundary location of $x = 0$ m, indicating the potential for this conceptual survey design to resolve saltwater-freshwater boundaries with high resolution enabled by fiber sensing.

The depth of the survey line was changed to determine the optimal sensor placement for the delineation of the saltwater-freshwater boundary. The TMI anomaly value was extracted from the results at $y = 0$ m and plotted at its corresponding x location in Figure 2.4. The largest change in the delineation ability is apparent from 5 m depth to 7.5 m depth, or just above the water table to just below it. For improved boundary delineation, the dense sensor line should be installed below the water table.

The boundary location was adjusted to values ranging from $x = -40$ m to $x = 40$ m to assess its impact on the data. Considering a 10 m sensor depth, the contour values for TMI anomaly were extracted along $y = 0$ m and plotted against x in Figure 2.5. The boundary locations in the profiles are indicated by magnetic field differences ranging from 17 nT to 19 nT. From the modeling output, there is no apparent difference in boundary delineation ability based on the horizontal location of the saltwater-freshwater boundary. This result suggests that a dense magnetic sensing array would be able to delineate saltwater-freshwater boundaries at any location along the array.

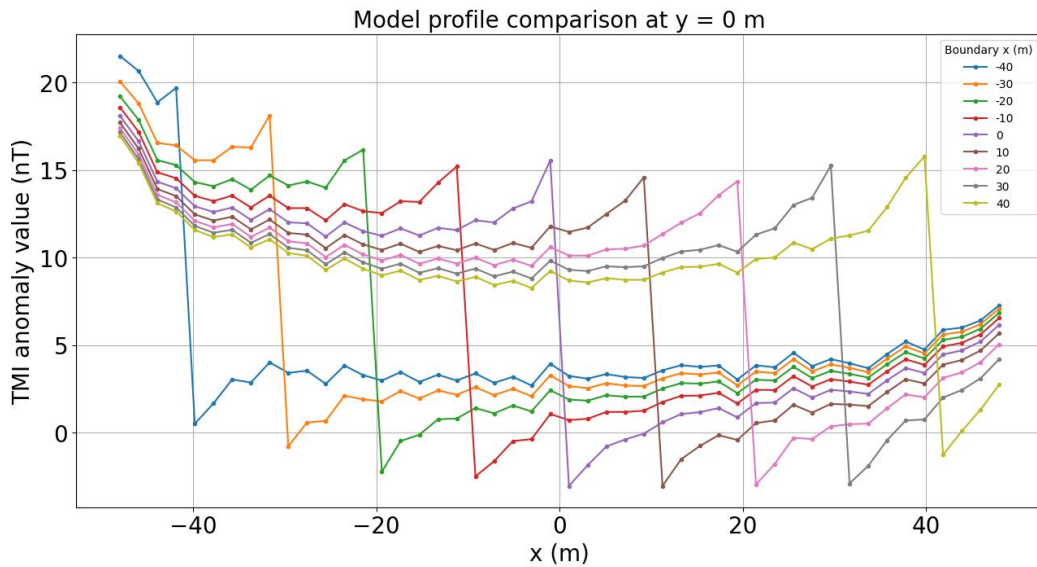


Figure 2.5 The profiles at $y = 0$ m and $z = -10$ m of the forward modeled TMI anomaly data with different saltwater-freshwater boundary locations are shown in this illustration. The sudden changes in TMI anomaly are at the same x locations as the boundary. This illustration shows that the forward-modeled data accurately represents the boundary location at any point along the profile.

2.2.2 Gradient Model

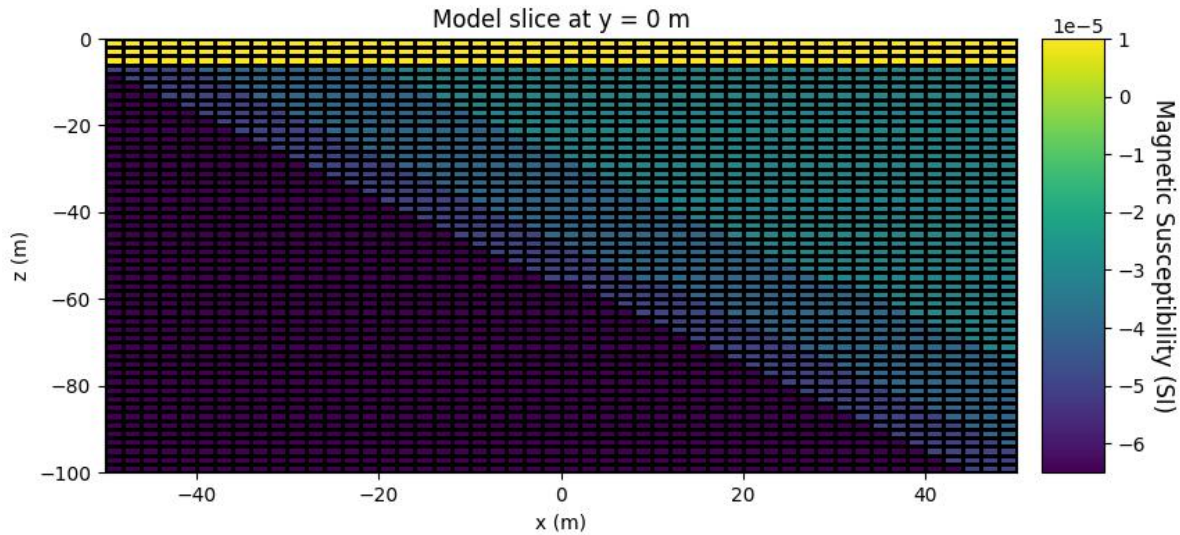


Figure 2.6 This illustration shows the subsurface model slice at $y = 0$ m that was created for magnetic simulation forward modeling of the gradient seawater intrusion model. The saltwater is on the left with a gradient in χ towards the freshwater. The χ values from left to right are $\chi_{seawater} = -6.5 \times 10^{-5}$, $\chi_1 = -5 \times 10^{-5}$, $\chi_2 = -4 \times 10^{-5}$, and $\chi_{freshwater} = -3 \times 10^{-5}$.

A more realistic model of seawater intrusion, shown in Figure 2.6, was created to assess the applicability of the fiber in a more realistic case of seawater intrusion. In reality, there is mixing at the interface between seawater and freshwater, creating a gradient of salinity. Additionally, the seawater does not travel through the subsurface as a block but rather travels along the bottom of the aquifer in more of a triangular shape as freshwater is pumped out of the system (Costall *et al.*, 2020).

In the subsurface model in Figure 2.6, the values of magnetic susceptibility are $\chi_{seawater} = -6.5 \times 10^{-5}$ (50 ppt salinity) and $\chi_{freshwater} = -3 \times 10^{-5}$. The mixed values are $\chi_1 = -5 \times 10^{-5}$ (25 ppt salinity) and $\chi_2 = -4 \times 10^{-5}$ (10 ppt salinity) to simulate a gradient. The resulting forward modeled data with the sensors at 10 m depth is shown in Figure 2.7. In the forward modeled data, the salinity changes in the water are visible as changes in the TMI anomaly value. The changes are not as abrupt as seen in the simple model results in Figure 2.3, however, the changes in TMI anomaly value coincide with changes in χ at 10 m depth.

The effect of changing the depth of the sensors on the forward modeled data is of interest, as performed for the simple model in Figure 2.4, particularly because of the vertical heterogeneity of the complex model. The TMI anomaly values along the x profile at $y = 0$ m for sensor depths of 10 m, 25 m, 50 m, and 75 m are shown in Figure 2.8. The changes in χ are visible in this figure as distinct dips in TMI anomaly ranging

from 3 nT to 6 nT in magnitude. The 25 m and 50 m profiles show three of these dips, reflecting the three shifts in χ along those profiles. These dips are visible at -32 m, -24 m, and -2 m for the 25 m profile and -10 m, 2 m, and 22 m for the 50 m profile. The first boundary at $x = -48$ m can be seen in the 10 m data, but not as well since there is only one data point in the saltwater that extends from $x = -50$ m to $x = -48$ m. Only two dips in TMI anomaly can be seen in the 75 m profile at $x = 20$ m and $x = 30$ m because there are only two changes in χ along this profile.

In real applications, gradients are smoother than the discretized zones created in the model. Gradient smoothness may introduce some challenges in data interpretation which have not been captured with this modeling, however, the modeling has shown that changes in salinity can be captured with a distributed source DC survey that has densely spaced sensors mimicking the DMS fiber. The sensors should be placed deep enough to capture the gradient changes of interest. If the sensors are placed too shallow, they will not capture the contaminant plume front fully. However, groundwater modeling could be used in conjunction with this sensor array to calculate the plume front location at deeper locations than observed by the fiber (Costall *et al.*, 2020).

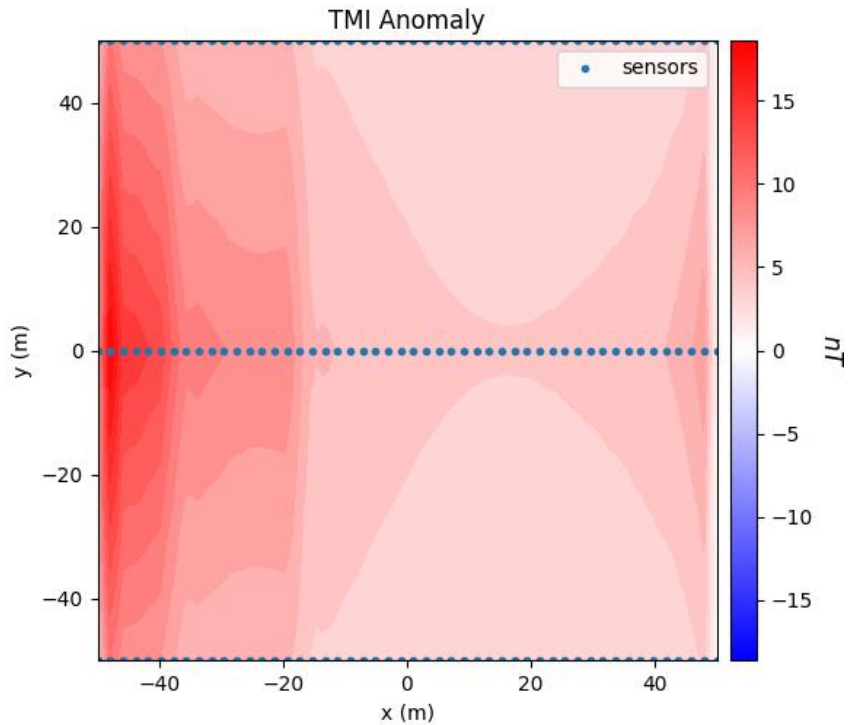


Figure 2.7 The forward modeling results of Figure 2.6 are shown in this image. The sensors are ten meters deep and are placed two meters apart to model the Bragg grating spacing of the DMS fiber. This image is a two-dimensional slice at the sensor depth of 10 m. There are two major shifts visible in this data along the x-axis that coincide with changes in χ at a depth of 10 m.

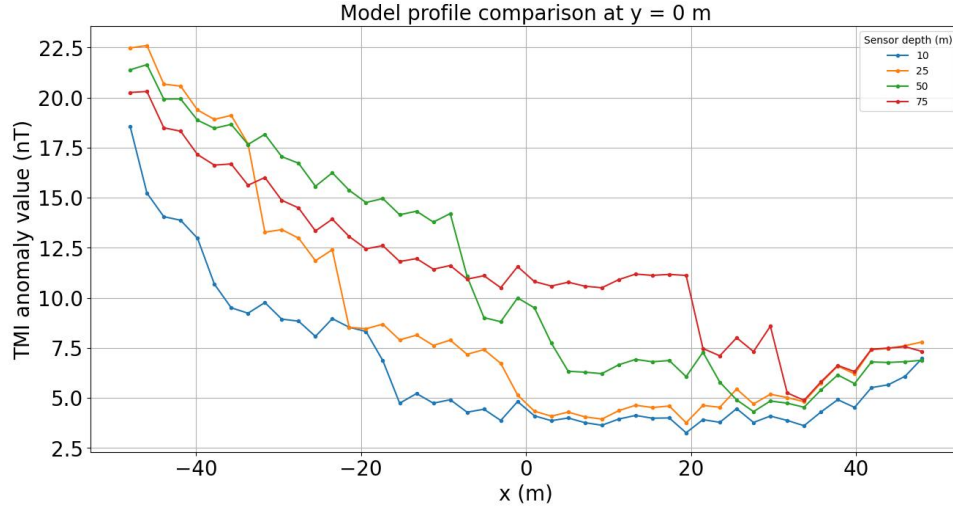


Figure 2.8 The profiles at $y = 0$ m and of the forward modeled TMI anomaly data slice at the sensor depth, with sensors at different depths of the model in Figure 2.6 are shown in this illustration. Shifts that are relatively large in the TMI anomaly data compared to the gradual slopes of the data are indicative of χ boundaries.

2.3 Mine Drainage Modeling

Mine drainage, such as metal leaching from tailings dams or other sources, can spread from the source to other areas via groundwater transport. In the case of a tailings dam, a contaminant plume spreads from the surface location of the dam downward and in the direction of groundwater flow (Lima *et al.*, 2024). To model the monitoring of iron leaching from a tailings dam with a DMS fiber, we initially used the simple model in Figure 2.2 with the χ values experimentally recorded in Orlyuk *et al.* (2022) for tap water, $\chi_{water} = -1.65 \times 10^{-5}$, and magnetized tap water, $\chi_{mag} = -1.575 \times 10^{-5}$, which is characterized by increased total iron content. However, these χ values are too similar to determine where the magnetic susceptibility changes in the forward modeled data, shown in Figure 2.9. This could be due to a low concentration of iron ions in the magnetized tap water, but we do not know because the iron concentration was not reported in this study. For this reason, the magnetic susceptibility of a solution of iron and water was calculated using a theoretical relationship,

$$\chi^{soln} = -9.0 \times 10^{-6} + cC_{mol}/T, \quad (2.1)$$

where c is concentration in mol/m^3 and T is temperature (Coey *et al.*, 2007). Note that this equation assumes $\chi_{freshwater} = -9.0 \times 10^{-6}$. C_{mol} is the Curie constant, given by

$$C_{mol} = 1.571 \times 10^{-6} p_{eff}^2, \quad (2.2)$$

where p_{eff} is the effective Bohr magneton number. For our application with iron as the solute, we used Fe^{2+} , with $p_{eff}^2 = 24$ and $T = 295$ K (Coey *et al.*, 2007).

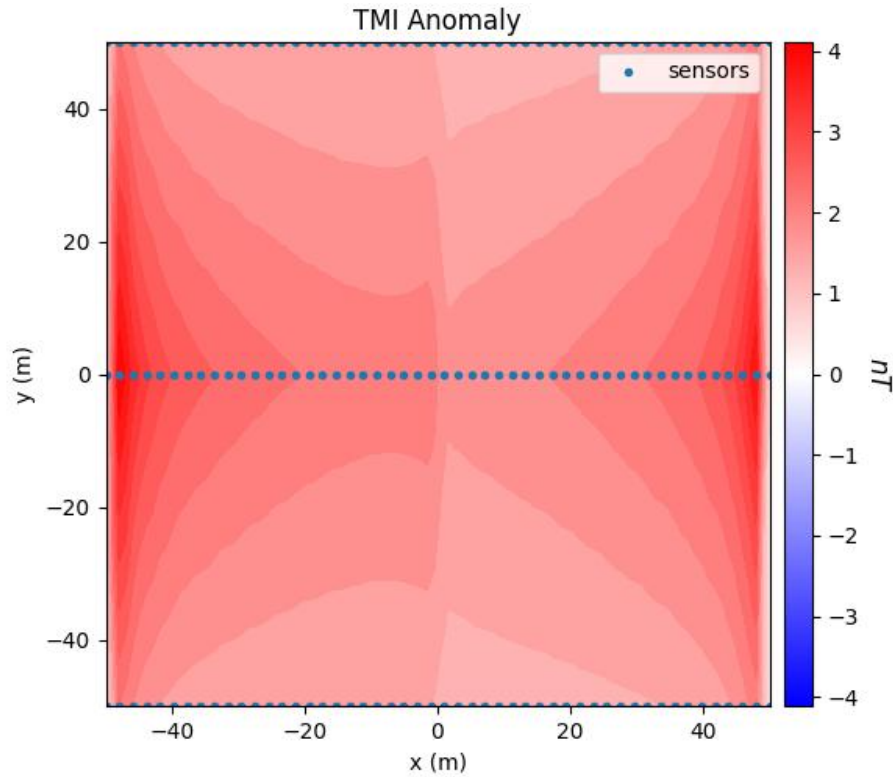


Figure 2.9 The forward modeling results with iron as a solute with χ values based on Orlyuk *et al.* (2022) are shown in this image. The sensors are ten meters deep and are placed two meters apart to model the Bragg grating spacing of the DMS fiber. This image is a two-dimensional slice at the sensor depth of 10 m. There is a slight change in TMI anomaly at the boundary between the freshwater and iron water at $x = 0$ m, but it is not as obvious as seen in the seawater intrusion model.

Using the simple geometry of the model in Figure 2.2, the purple block on the left was set to $\chi_{freshwater} = -9.0 \times 10^{-6}$ and the teal block on the right was calculated for a given concentration using Equation 2.1. The sensor depth was set to 10 m. Forward models were created for concentrations from 0 mg/L to 1000 mg/L and the TMI anomaly values along the profile $y = 0$ m were plotted in Figure 2.10. The 0 mg/L, 1 mg/L, and 10 mg/L lines overlap each other, suggesting they are indiscernible from one another. Therefore, the resulting TMI anomaly profiles suggest that Fe^{2+} concentrations of at least ≈ 100 mg/L are discernible from freshwater.

The limit on iron concentrations in freshwater set by the EPA is 0.3 mg/L. Unfortunately, this sensor array would be unable to detect iron concentration at that order of magnitude based on these simulations. However, it may be suitable for monitoring previously identified areas of concern with high iron concentrations, such as iron mine regions (Affandi *et al.*, 2018; Razowska, 2001). Other ions explored in

Coey *et al.* (2007) (Ti^{3+} , V^{2+} , V^{3+} , Cu^{2+} , Ni^{2+} , Cr^{3+} , Co^{2+} , Mn^{2+} , Mn^{3+} , and Fe^{3+}) have similar or lower values of χ^{soln} . Further studies could investigate the trade-off between the concentrations of these other ions and the potential to detect them using a similar study design.

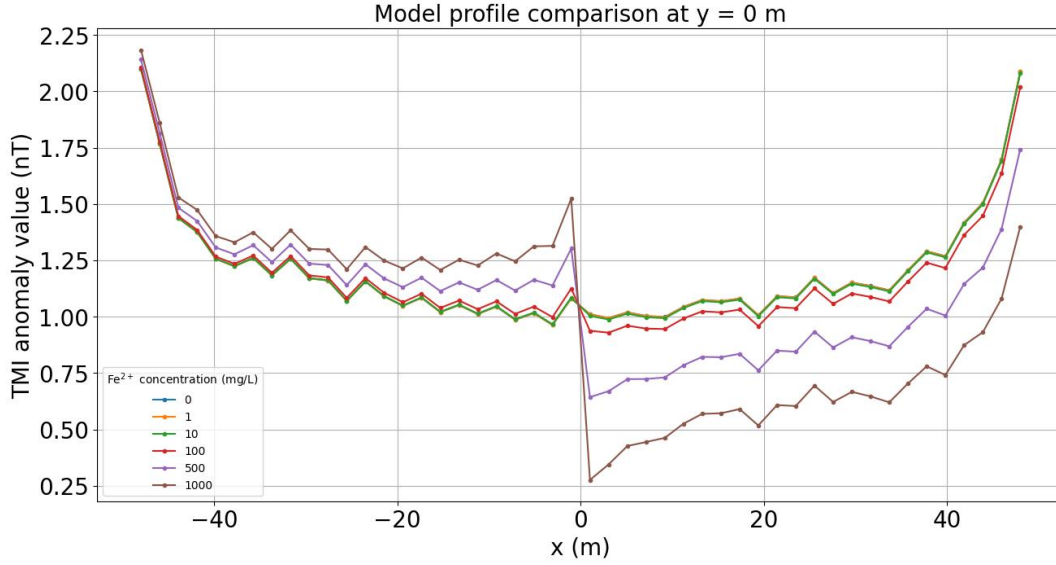


Figure 2.10 The profiles at $y = 0$ m and $z = -10$ m of the forward modeled TMI anomaly data with sensors at a depth of 10 m in the model shown in Figure 2.2 are shown in this illustration. The profiles shown are for different concentrations of Fe^{2+} in the right block with freshwater in the left block. The 0 mg/L, 1 mg/L, and 10 mg/L lines overlap nearly completely.

2.4 Lithium Brine Modeling

Lithium brines that are used for economic purposes contain high concentrations of Li^+ , reaching up to 1500 mg/L of Li^+ in the “Lithium Triangle” (Tabelin *et al.*, 2021). Lithium is a paramagnetic material with a nuclear spin of $3/2$ for ${}^7\text{Li}$, the most common isotope (Kondev *et al.*, 2021). Using the spin value of $S = 3/2$ and $p_{eff}^2 = 15$, the χ value of a Li^+ solution in water, χ_{Li} , can be calculated using Equations 2.1 and 2.2.

To determine the ability of the survey setup to detect a shift from freshwater to lithium brine, the model in Figure 2.2 was used with the left, purple block set to freshwater magnetic susceptibility, $\chi_{\text{freshwater}} = -9.0 \times 10^{-6}$, and the right, teal block set to the calculated value of χ_{Li} . The sensor depth was set to 10 m. Forward models were created for concentrations from 0 mg/L to 1500 mg/L and the TMI anomaly values along the profile $y = 0$ m were plotted in Figure 2.11.

There is a clear change in TMI anomaly at the boundary between freshwater and lithium solution for Li^+ concentrations in the economically viable range in Figure 2.11. Additionally, the difference in TMI

anomaly value between the freshwater and lithium solution increases from 1 nT to 9 nT with increasing Li^+ concentration from 100 mg/L to 1500 mg/L. These results suggest that this survey design could be useful in monitoring lithium brine mining, provided the sensors are sensitive enough to detect magnetic field changes on the order of 1 nT and larger.

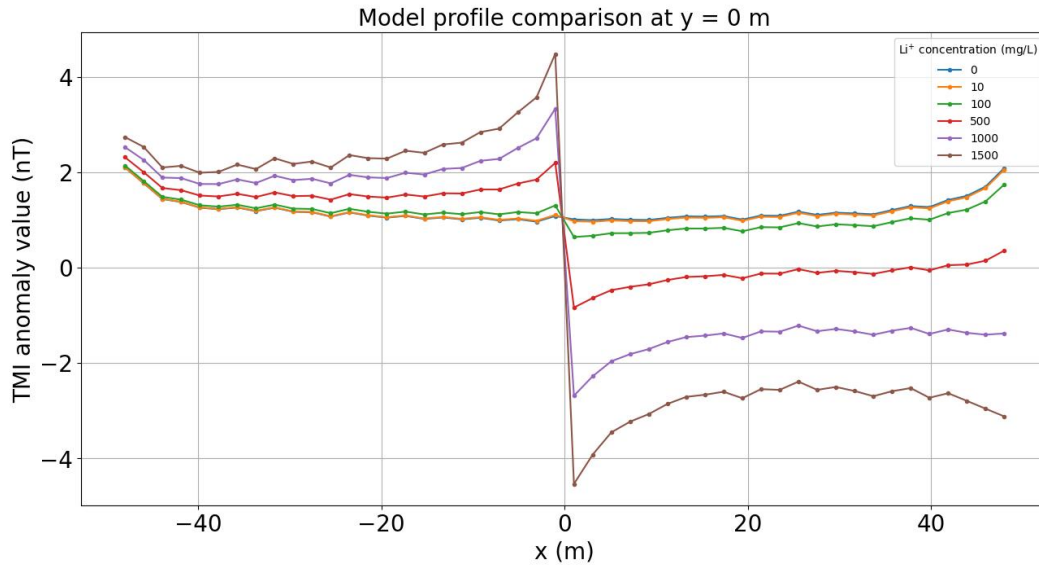


Figure 2.11 The profiles at $y = 0$ m and $z = -10$ m of the forward modeled TMI anomaly data with sensors at a depth of 10 m in the model shown in Figure 2.2 are shown in this illustration. The profiles shown are for different concentrations of Li^+ in the right block with freshwater in the left block.

2.5 Model Limitations

The modeling performed in this chapter is limited by a few factors that should be highlighted and addressed in future modeling efforts if the question of the feasibility of DMS in the application areas mentioned is to be answered appropriately.

For one, this modeling assumed concentrations of single ions in the water; however, it is important to note that groundwater in reality contains other analytes and isotopes that can change magnetic susceptibility (Kumar *et al.*, 2022). The effect of mixing additional ions in the water solution could be accounted for by using Equation 2.1 to calculate the change in χ^{soln} due to each ion. For each ion, an additional cC_{mol}/T term could be added (paramagnetic ions) or subtracted (diamagnetic ions) to Equation 2.1. This would provide a rough estimate of the net value of χ^{soln} , assuming a linear relationship. Using this method, the more paramagnetic ions are in the solution, the more positive χ^{soln} becomes; whereas the more diamagnetic ions are in the solution, the more negative χ^{soln} becomes.

Second, these simulations assume that the magnetic field is applied throughout the entire block of material. This type of field is not easily producible using available sources. This likely led to larger TMI anomaly differences in the forward modeled data than those that would be apparent in reality with easily available sources as more material is exposed to the magnetic field than would be in real application. One way to reconcile this issue would be to consider an application method wherein a solenoid is placed inside the borehole, surrounding the fiber, illustrated in Figure 2.12. With this method, a solenoid would be placed in the borehole, surrounding the fiber. An alternating current would be sent through the solenoid to produce an alternating magnetic field. The magnetic field would interact with the water in the borehole which would produce another magnetic field with an amplitude determined by the water composition. The DMS fiber would then register a response due to the solenoid magnetic field and the response of the water. The difference between the predicted fiber response solely to the solenoid magnetic field and the additional response to the water could be used to determine the magnetic susceptibility of the water. This would essentially be a long magnetic susceptibility meter capable of easier time-lapse monitoring and higher spatial coverage than is currently available. This method would be a more achievable application with available equipment. Appendix E discusses this hypothetical application method in more detail.

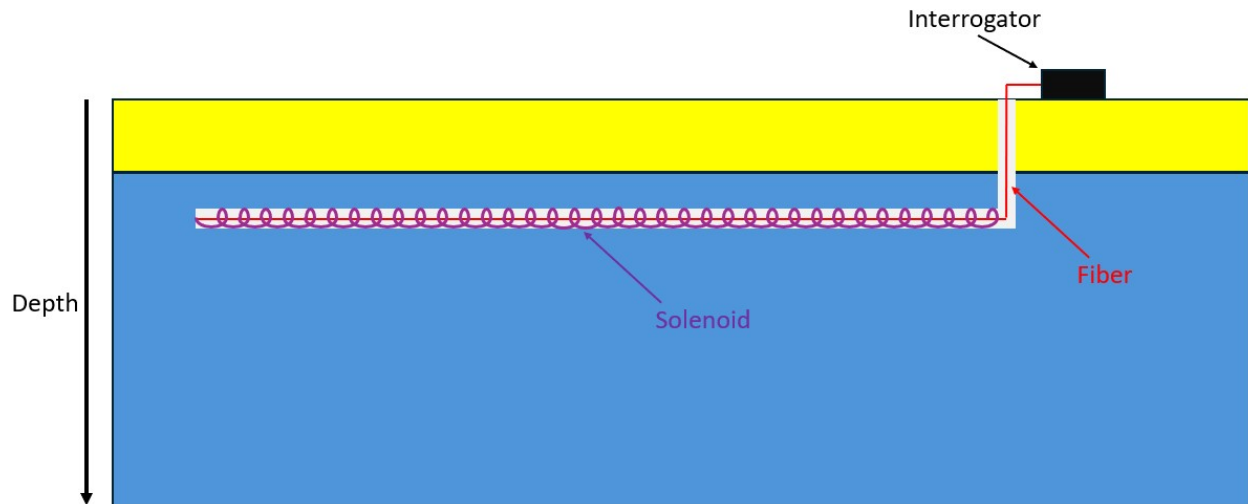


Figure 2.12 In this proposed application method, the fiber will be placed in a horizontal borehole below the water table (blue) with a solenoid surrounding it. An alternating current would be sent through the solenoid to produce an alternating magnetic field that the fiber would respond to.

Third, the models in this chapter assume the magnetic susceptibility of the groundwater beneath the water table is solely due to water and the aquifer material does not change χ . This presents an issue with the model because, in reality, the aquifer material does have a magnetic susceptibility that would influence the composite value of χ . The method of application illustrated in Figure 2.12 and outlined in Appendix E

would address this limitation.

Fourth, these simulations used a static magnetic field as the applied field, whereas real application would require an alternating magnetic field for the DMS fiber to be most sensitive. SimPEG does not have the capability to include an alternating magnetic field in models, so this may need to be resolved by using different software or by adding an alternating magnetic field to existing SimPEG code.

Fifth, these simulations assumed no noise sources to produce the TMI anomaly results. In real applications, noise sources may include power lines and the Earth's magnetic field. In real application scenarios, the Earth's magnetic field will likely be negligible since the DMS fiber is currently less sensitive to static magnetic fields than alternating magnetic fields. However, simulating both scenarios would be useful for confirmation of signal detection even in the presence of common noise sources.

Finally, this modeling was performed for a setup with a horizontal borehole; however, simulations were only performed this way due to limitations with SimPEG. Real applications could be similarly performed with a vertical borehole. If there are vertical differences in water solution, this sensor array could potentially delineate these changes in solution with similar sensitivity as the horizontal borehole sensitivity.

2.6 Conclusions

A simulated survey with three lines of magnetic sensors with 2 m spacing between sensors was created to mimic the Bragg grating DMS fiber discussed in Hileman *et al.* (2022) and Dejneka *et al.* (2024). This simulated survey was used to determine whether a dense magnetic sensor array can be applied to determine water composition changes in three different cases with a constant magnetic field throughout the entire study volume. Seawater intrusion modeling revealed it is possible to resolve a boundary between saltwater and freshwater when the sensor line is placed beneath the water table. Additionally, the sensors can detect salinity changes within a gradient of saline water to fresh water. Modeling a mine drainage solution of Fe^{2+} in water revealed that the sensors can image Fe^{2+} concentrations of 100 mg/L and higher. Modeling a lithium brine solution of Li^+ in water revealed that the sensors can image economic Li^+ concentrations of 100 mg/L and higher.

This modeling provided some indication of magnetic field differences that might occur due to boundaries between freshwater and water with different ion concentrations. If applied in a seawater intrusion scenario with no gradient between the freshwater and saline water, a magnetic field difference on the order of ~ 10 nT would be present. In a seawater intrusion scenario with a gradient between saline water and fresh water, a magnetic field difference on the order of ~ 1 nT would be present. In a mine drainage scenario with a boundary between water with Fe^{2+} ions and freshwater, a magnetic field difference on the order of ~ 0.1 nT would be present for Fe^{2+} concentrations of 100 mg/L. In a lithium

brine scenario with a boundary between water with Li^+ ions and freshwater, a magnetic field difference on the order of ~ 1 nT would be present for Li^+ concentrations of 100 mg/L.

Typical magnetic field sensors have sensitivities that can delineate the magnetic field differences determined from modeling, see section 1.1. However, before extending any of these concluding remarks to the DMS fiber application feasibility, the limitations outlined in section 2.5 must be addressed.

CHAPTER 3

LABORATORY AND FIELD EXPERIMENTS

This chapter discusses the laboratory and field experiments performed on a DMS fiber without Bragg gratings. Laboratory experiments were performed to determine the magnetic field sensitivity and time-dependent behavior of a DMS fiber without Bragg gratings. A comparison to the magnetic field sensitivity of a DMS fiber with Bragg gratings is provided to determine whether the inclusion of Bragg gratings in the DMS fiber provides increased sensitivity. Field experiments were performed with a solenoid and TEM to determine the feasibility of using the DMS fiber with different magnetic field sources. All single-sided amplitude spectra in this chapter were normalized by the number of samples. Please note that amplitude spectra are different from power spectra and that ε represents units of strain. An additional laboratory experiment that was set up but not carried out due to time constraints is outlined in Appendix B.

3.1 Laboratory Experiments

Laboratory experiments, described in Hileman *et al.* (2022) and Dejneka *et al.* (2024), were performed by our colleagues at Virginia Polytechnic Institute and State University (Virginia Tech) to determine the behavior of a DMS fiber with Bragg gratings. To determine the magnetic field sensitivity of a DMS fiber with two Metglas cladding wires and Bragg gratings, they placed a 2 m length of Bragg grating DMS fiber in a 2 m long solenoid and exposed the DMS fiber to alternating magnetic fields of different magnitudes using the solenoid as a magnetic field source. The fiber data was collected using the Sentek Instrument picoDAS interrogator, which provides high sensitivity.

The laboratory experiments outlined in this section were performed on a DMS fiber with two Metglas cladding wires without Bragg gratings to provide a comparison between the sensitivity of the Bragg grating and non-Bragg grating fibers. Additionally, an analysis of the time-dependent behavior of the DMS fiber signal is discussed in this section. A solenoid was used as the alternating magnetic field source in these experiments as well. The fiber data was collected using the Terra15 Treble DAS interrogator, which provides low noise through the active-seismic, passive-seismic, and acoustic frequency bands.

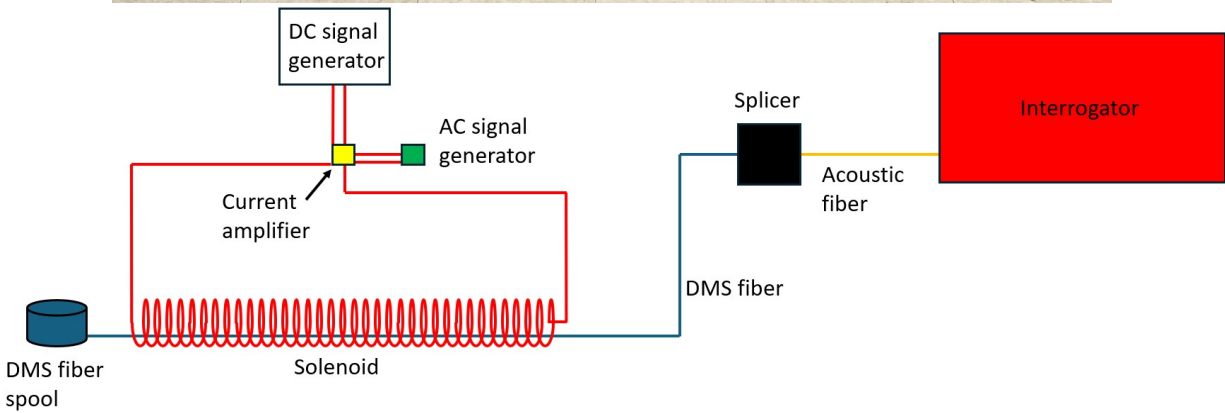


Figure 3.1 The laboratory setup for testing the DMS fiber without Bragg gratings is shown in this image. The top image shows the actual laboratory setup, while the bottom image shows a simplified diagram of the laboratory setup. The interrogator is not shown in the top image.

3.1.1 Experimental Design

The laboratory setup for the fiber without Bragg gratings is shown in Figure 3.1. We built a current amplifier capable of producing a current of 1.5 ± 0.2 A to increase the amplitude of the magnetic field produced by the solenoid. The solenoid used in the experiments was 1.5 m long with ≈ 450 wire turns. Using Equation 1.6 to calculate the approximate maximum magnetic field yields $B \approx 560$ μT for our solenoid. The current amplifier was powered by the DC source (GW Instek GPD-X303S) and the AC source (Digilent Analog Discovery 2) and was connected to the solenoid, as shown in Figure 3.2. The DMS fiber was fed through the solenoid, touching the bottom of the solenoid and under no tension, with the spool placed outside the end of the solenoid. The DMS fiber was mechanically aligned with the acoustic fiber leading to the DAS interrogator unit. The manual alignment was accomplished using the Fujikura FSM-70S Fusion Splicer with index-matching gel placed at the fiber connection point. It is difficult to achieve a high transmission with the manual alignment method - see Appendix C for more details on this. The end of the spool of DMS fiber was bent into a small loop to increase the attenuation of the light, improving the signal measured by the interrogator. For all experiments, the gauge length of the interrogator was set to 1.63 m to capture the length of the solenoid within one channel.

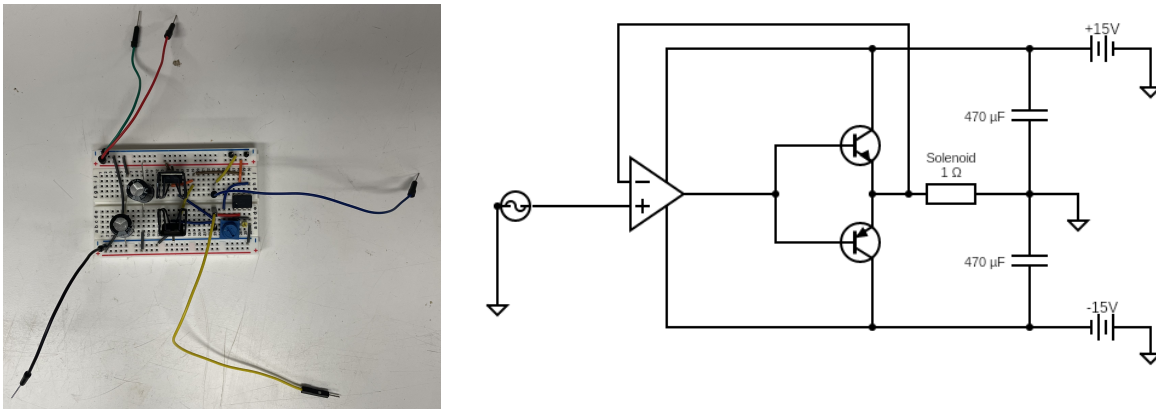


Figure 3.2 The current amplifier (left) and its circuit diagram (right) are shown in this image. The current amplifier is not attached to the solenoid in the left image, but the solenoid is shown as a 1 Ω load in the circuit diagram.

To determine the minimum magnetic field sensitivity of the DMS fiber, the AC source was set to 5.0 V initially and incrementally decreased by 1.0 V until a signal was no longer visible, at which point the AC amplitude was set to the previous value then decreased by 0.1 V increments until the signal was no longer visible. The DC source amplitude was set to values at least 4.0 V above the AC source amplitude in accordance with the limitations of the operational amplifier (op-amp). Each recording was collected for one

minute to reduce the effect of transient background noise. The 5.0 V AC amplitude recording was only run for 30s since the amplifier would overheat if it was run too long at that voltage.

The AC source was incrementally decreased because the fiber becomes slightly magnetized from the previous larger field, so when the source magnetic field is reduced there is a net initial magnetization direction in the magnetostrictive material, which increases the magnetostriction in the fiber. This is potentially a method of increasing sensitivity that could be taken advantage of in the field by initially magnetizing the fiber, then performing experiments to increase sensitivity. However, it guided our choice to pursue the decreasing field procedure.

The experiment to determine the time dependence of the signal was performed by recording a 1000 Hz frequency magnetic field produced by the solenoid for five minutes. In this experiment, the AC source was set to 3.0 V and the amplitudes of the 1000 Hz and 2000 Hz peaks produced by the fiber were recorded. While the interrogator was recording, no one moved to ensure that acoustic vibrations were kept to a minimum.

3.1.2 Data and Analysis

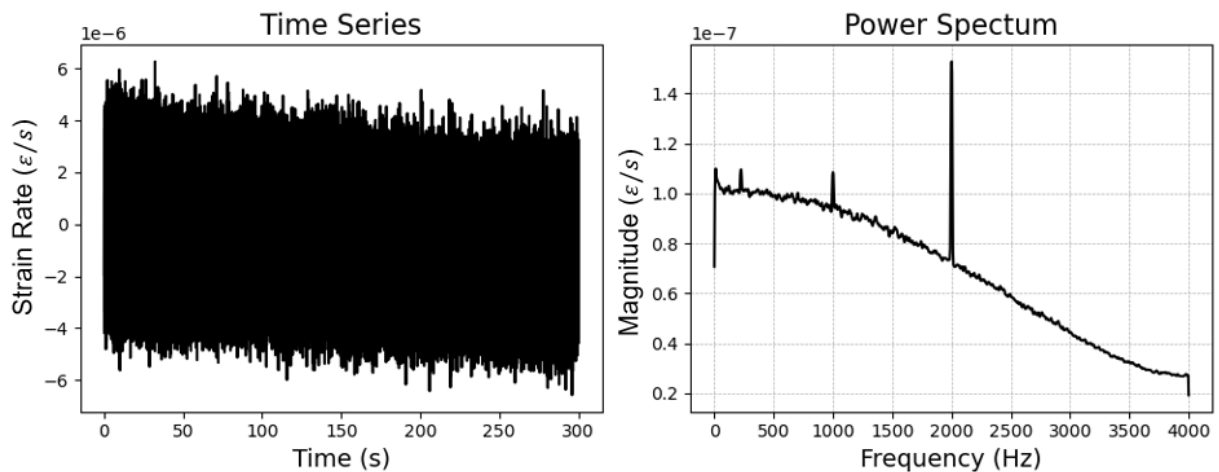


Figure 3.3 The time series (left) and power spectrum (right) output for an AC source amplitude of 3.0 V are shown in this image. The power spectrum shows a 1000 Hz and 2000 Hz fiber response, which are typical magnetostrictive responses at the source frequency and double the source frequency.

Figure 3.3 shows an example output of the DMS fiber response produced using DASCORE (Chambers *et al.*, 2024). There are 1000 Hz and 2000 Hz responses in the fiber signal which demonstrate a typical magnetostrictive response at the magnetic field source frequency and double the source frequency (Dejneka *et al.*, 2024; Hileman *et al.*, 2022). While the 2000 Hz response is larger in the image shown, it disappears from the signal at higher magnetic field strengths than the 1000 Hz response, i.e. the magnetic field

sensitivity of the 2000 Hz response is lower. Because of this, we made use of the 1000 Hz response to determine the magnetic field sensitivity. Figure 3.4 shows the variation of the 1000 Hz response to an applied magnetic field. The minimum sensitivity was identified at the magnetic field generated by the AC signal, 0.1 V above the point where the 1000 Hz signal was no longer detectable in the spectrum.

Sample sliding windows (30 s length, 5 s offset) of the 300 s signal were used to calculate the power spectrum response amplitudes and capture the variation of the power spectrum response over time. Figure 3.5 shows the results of this analysis using a magnetic field strength produced by a 3.0 V amplitude AC source at both 1000 Hz and 2000 Hz. This signal shows some variation over this time period, indicating that the power spectrum depends on time. When tested with other AC amplitudes, results were similar to those seen in Figure 3.5.

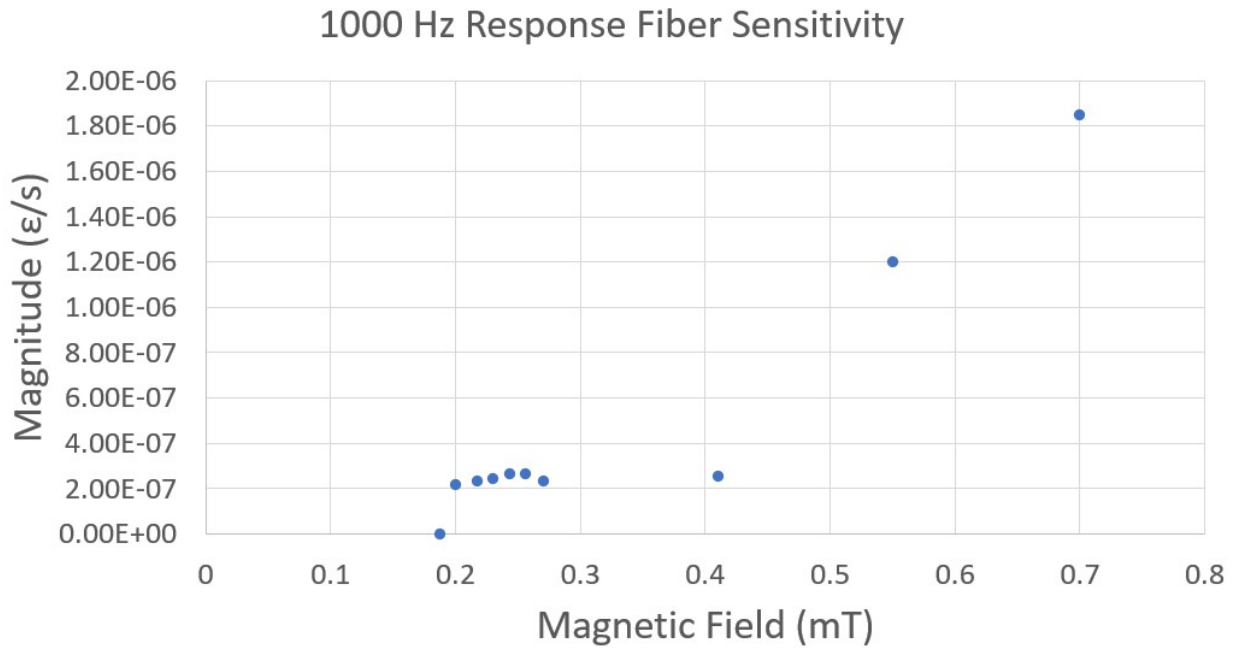


Figure 3.4 The experimental spectral response amplitudes of the fiber without Bragg gratings for the 1000 Hz response to a 1000 Hz solenoid source are plotted against magnetic field strength in this figure. The signal fades from the power spectrum at 0.2 mT.

3.1.3 Laboratory Results and Discussion

The results of the magnetic field sensitivity test, shown in Figure 3.4, demonstrated that the 1000 Hz signal was visible down to an applied magnetic field of 0.2 mT. Since this test was performed by starting at a larger magnetic field and incrementally decreasing the field, sensitivity was increased compared to the method of increasing the magnetic field incrementally from a lower field. The magnetic field sensitivity reported in Dejneka *et al.* (2024) for a fiber with two Metglas cladding wires and Bragg gratings at a

magnetic field source frequency of 100 Hz was ~ 500 nT. While these results are for different source frequencies, the 100 Hz signal for the fiber without Bragg gratings was not detectable at the minimum magnetic field determined for 1000 Hz in this experiment. Therefore, the Bragg gratings increase sensitivity by nearly three orders of magnitude.

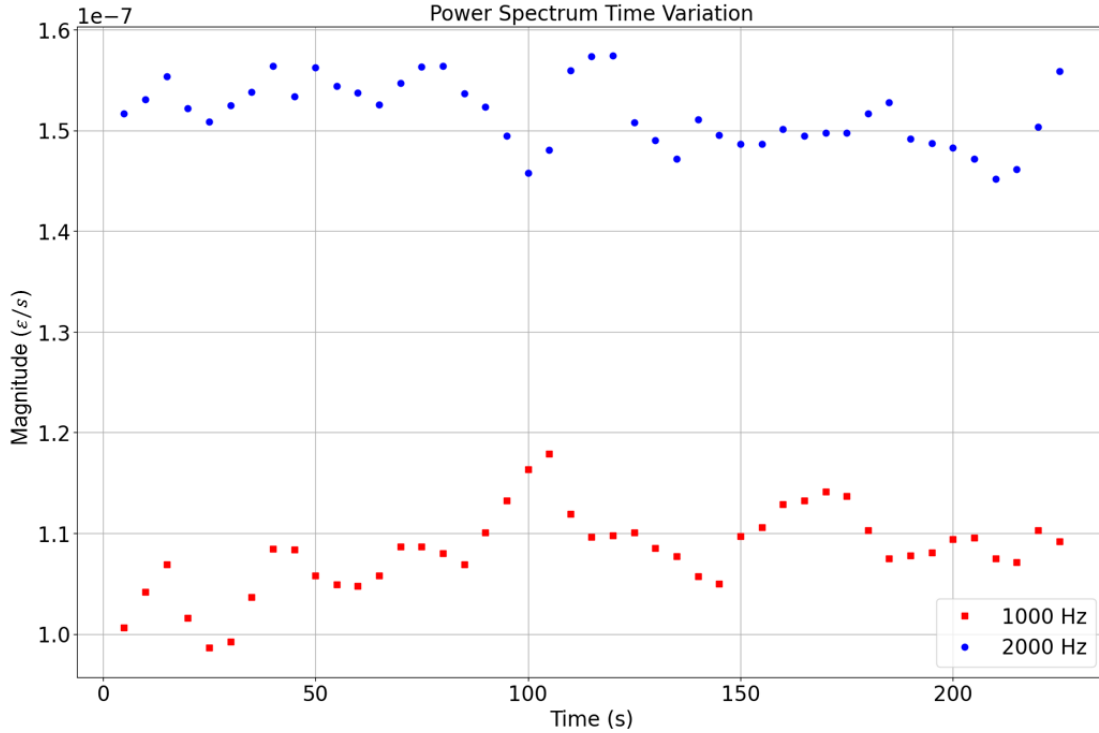


Figure 3.5 The power spectrum variation over time of the fiber response for an AC source amplitude of 3.0 V and a frequency of 1000 Hz is shown in this plot. The 1000 Hz and 2000 Hz response magnitudes were calculated using sample sliding windows (30 s length, 5 s offset) of the 300 s signal.

The variation of the power spectrum over time, shown in Figure 3.5, is significant enough that the 1000 Hz response varies between being detectable and undetectable in the power spectrum. The 2000 Hz response in this experiment never disappeared below the noise level, but did have some variation in amplitude. This shows the time variation of the signal can be important depending on whether the signal amplitude is close to the noise level. It is important to consider the noise level at a given frequency when determining what frequency to image, since sensitivity changes based on the noise level.

The experiments were limited to a 1000 Hz source because the current amplifier available to our team only performed well in a relatively narrow frequency range. Magnetic field sensitivity should be analyzed at different frequencies in the future if a current amplifier capable of operating reliably at lower frequencies is available. Additionally, sensitivity greatly depends on the fiber splice quality. The noise floor in the signal varies by orders of magnitude based on how well the fiber cores were aligned during the manual alignment

procedure. A fiber connector would greatly improve this issue if it is possible to include this with the DMS fiber in the future.

Through these experiments, the Metglas fiber without Bragg gratings was shown to be less sensitive than the Metglas fiber with Bragg gratings (Dejneka *et al.*, 2024; Hileman *et al.*, 2022). However, for applications that only require sensitivity to magnetic fields larger than ~ 0.2 mT, we see that Bragg gratings may not be necessary. Additionally, the functionality of a DMS fiber without Bragg gratings at 1000 Hz was shown in these experiments, providing some confidence that the DMS fiber can operate similarly to current magnetic susceptibility meters at one commonly used frequency, as discussed in Chapter 2.

Currently, the Kappabridge MFK2 is used in some environmental studies to determine the magnetic susceptibility of water, e.g. Rana *et al.* (2021) and Kumar *et al.* (2022). This instrument operates at magnetic fields ranging from 200 A/m to 700 A/m ($1 \text{ mT} = 795.77 \text{ A/m}$) and frequencies of 976 Hz, 3904 Hz, and 15616 Hz. Laboratory experiments testing DMS fiber operation at these frequencies would provide some confidence that the DMS fiber can perform similarly to current magnetic susceptibility meters.

3.2 Field Experiments

Field experiments were performed using two setups: (1) using a Metglas fiber with two cladding wires, Bragg gratings, and a solenoid as the magnetic field source and (2) using a Metglas fiber with two cladding wires, no Bragg gratings, and the ABEM WalkTEM as the magnetic field source. The objectives of these tests were to determine the feasibility of field tests with the Bragg grating fiber and to determine the practicality of application with a typical geophysics instrument as the magnetic field source for the fiber without Bragg gratings.

3.2.1 Field Test with Bragg Grating Fiber and Solenoid

Solenoid experiments with the Bragg grating fiber were performed in 2023 on March 28 and March 29. A trench was made wherein the Metglas DMS fiber, with two cladding wires and Bragg gratings, and DAS fiber were buried with about a centimeter of sand covering them, shown in Figure 3.6. The DAS fiber was connected to the Sentek Instrument picoDAS interrogator, placed along a 10 m length of the trench, then manually aligned with the DMS fiber at the end of the trench. The DMS fiber was then placed inside the trench along the same line as the DAS fiber with the spool of DMS fiber at the end of the line. Geophones were placed along the same line with 0.5 m spacing to provide a method of signal differentiation between the fiber magnetic and acoustic responses. Simultaneous vibration and magnetic tests did not produce usable results; however, methods of signal separation are explored further in Hileman *et al.* (2022).

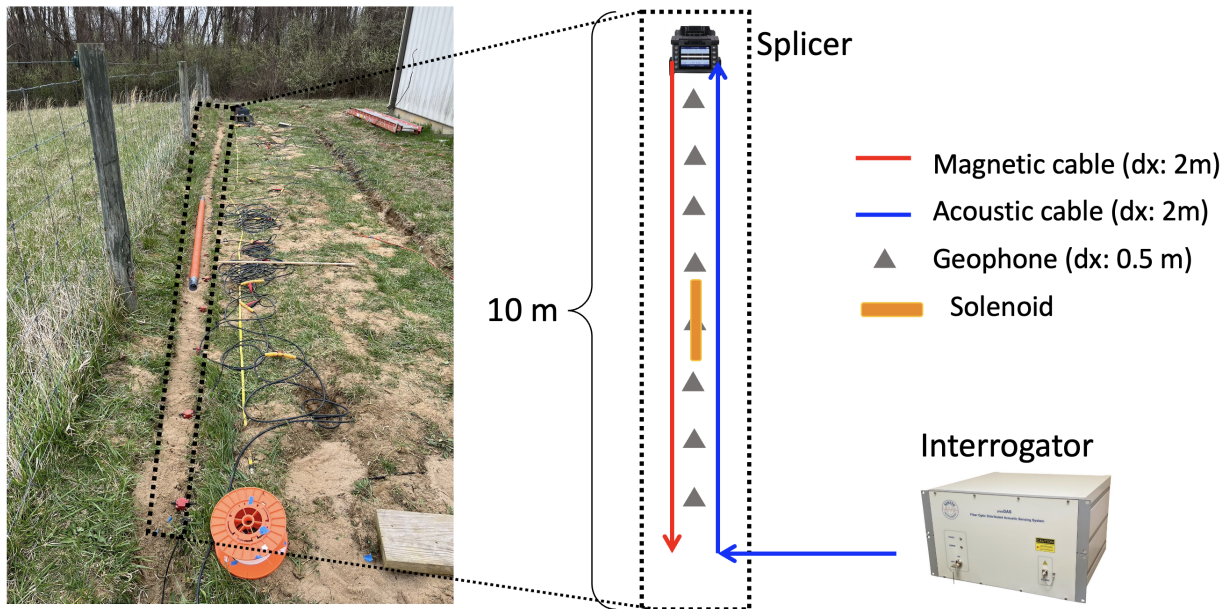


Figure 3.6 The experimental setup for the Metglas fiber with Bragg gratings is shown in this image. The fiber was lightly buried underneath the solenoid in this experimental setup (figure courtesy of Shihao Yuan).

The solenoid was placed directly on top of the buried fibers, 0.5 m right of the fibers (using Figure 3.6 for reference directions), and 1.0 m right of the fibers for each magnetic field test. The solenoid was oriented parallel to the fibers at each location and an iron rod was placed inside the solenoid to increase the strength of the magnetic field. Observing the signal from a magnetometer placed near the solenoid, the iron rod was observed to add some strong harmonics to the magnetic field signal. These harmonics may have increased the strength of the harmonics observed in the fiber responses.

Spectra recorded by a DMS fiber channel during the solenoid testing for 100 Hz and 1000 Hz sources with the solenoid on top of the fiber are shown in Figure 3.7. The most striking difference between these results is how many more peaks there are in the response to the 100 Hz source than the 1000 Hz source. Interestingly, this was also observed in the two-dimensional model when changing the frequency at the same magnetic field strength (see Chapter 4). Additionally, the 100 Hz source response only shows signals at multiples of double the applied field frequency (e.g. 200 Hz, 400 Hz, and so on...) which is also a characteristic predicted by the two-dimensional and three-dimensional models at high ratios of magnetic field strength to source frequency.

The results for a source frequency of 100 Hz with the solenoid placed on top and 0.5 m from the fiber are shown in Figure 3.8. We can see obvious decreases in the signal strength when the solenoid is placed further from the fiber. At 1.0 m away, there was no visible signal. The drastic decrease in signal with

distance is due to the magnetic field strength of the solenoid decreasing proportional to $1/r^3$ where r is distance.

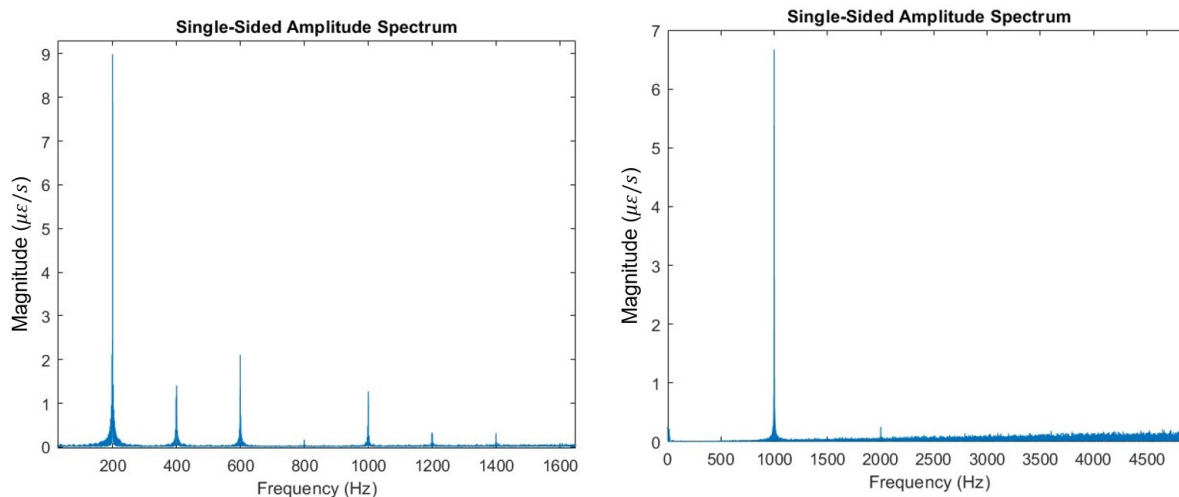


Figure 3.7 Amplitude spectra of the DMS fiber response to the solenoid on top of the fiber at 100 Hz (left) and 1000 Hz (right) are shown in this image. These spectra were calculated from channel 20 of the fiber and are normalized by the number of samples.

These tests successfully demonstrated the ability of a DMS fiber outside a solenoid to sense a magnetic field from the solenoid source. The Metglas DMS fiber with Bragg gratings is not currently sensitive enough to image the subsurface using this source. Additionally, the magnetic field generated in the soil was likely too low for the fiber to detect, considering the low χ of typical soils (Shirzaditabar & Heck, 2021). While a setup for cross-hole borehole surveys may be ideal with the fiber and a magnetic field source, the sensitivity of the fiber needs to be improved to accomplish this. However, the application method discussed in Chapter 2 may be possible since the magnetic field strength within a solenoid is much larger than outside the solenoid.

3.2.2 TEM Experiments

We carried out tests with the ABEM WalkTEM to test the feasibility of deploying a DMS fiber in conjunction with a typical geophysical source. For all field tests in this section, the less sensitive Metglas fiber without Bragg gratings was used. The WalkTEM setting used for these tests was “DualMoment_10ms_39gates”, which outputs a 30 ms period (33 Hz) square pulse signal. Figure 3.9 shows an example of the output signal recorded with the MC95A handheld magnetometer made by Magnetic Sciences. Notice how the signal contains harmonics, which contributes to increased harmonic strength in the DMS fiber signal.

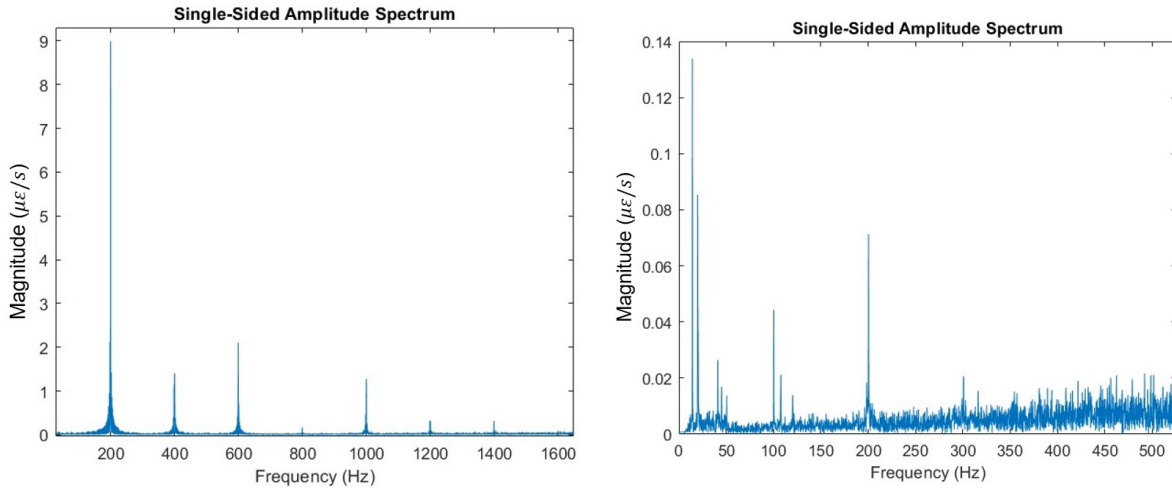


Figure 3.8 This image shows amplitude spectra recorded by the Bragg grating DMS fiber with the solenoid on top of the fiber (left), and 0.5m away from the fiber (right). These spectra were calculated from channel 20 of the fiber and are normalized by the number of samples.

3.2.2.1 First Trial

The field experiment on the North intramural field at Colorado School of Mines, Figure 3.10, was performed on October 12, 2023. A 40 m by 40 m transmitter loop was used in this experiment. The DMS fiber was manually aligned with a single-mode fiber connected to the Terra15 DAS interrogator unit. It was laid out from the splicer to the center of the 40 m by 40 m loop at 39°44'59"N, 105°13'31"W, with the spool placed next to the receiver loop. The interrogator and splicer were powered by a portable generator and the interrogator display was output onto a monitor. A cable and some cases were laid out next to the bare DMS fiber to mark its location. The interrogator was set to record with a 1.63 m gauge length, a 24.783 kHz sampling rate, and a fiber length of 89.8 m. Three tests were run with the TEM while the interrogator recorded over a period of 6 minutes and 12 seconds.

The results of the tests, shown in Figure 3.11, reveal a broad spectrum below 1000 Hz and a signal at 2265 Hz. The power spectrum of channel 12 (19.6 m) reveals that the lower frequency content contains a 33 Hz peak (the frequency of the TEM pulse), as expected, and peaks at 165 Hz, 264 Hz, and 363 Hz. Interestingly, the peaks at higher frequencies than the source frequency correspond to the fifth, eighth, and eleventh harmonics of the 33 Hz source frequency. In the field experiments with the fiber with Bragg gratings (e.g. Figure 3.7), it was found that sometimes higher harmonics were higher amplitude than lower harmonics, which could be what is seen here as well. It is possible that other harmonics that cannot be seen in the data are below the noise level created by the wind during this bare fiber surface deployment.

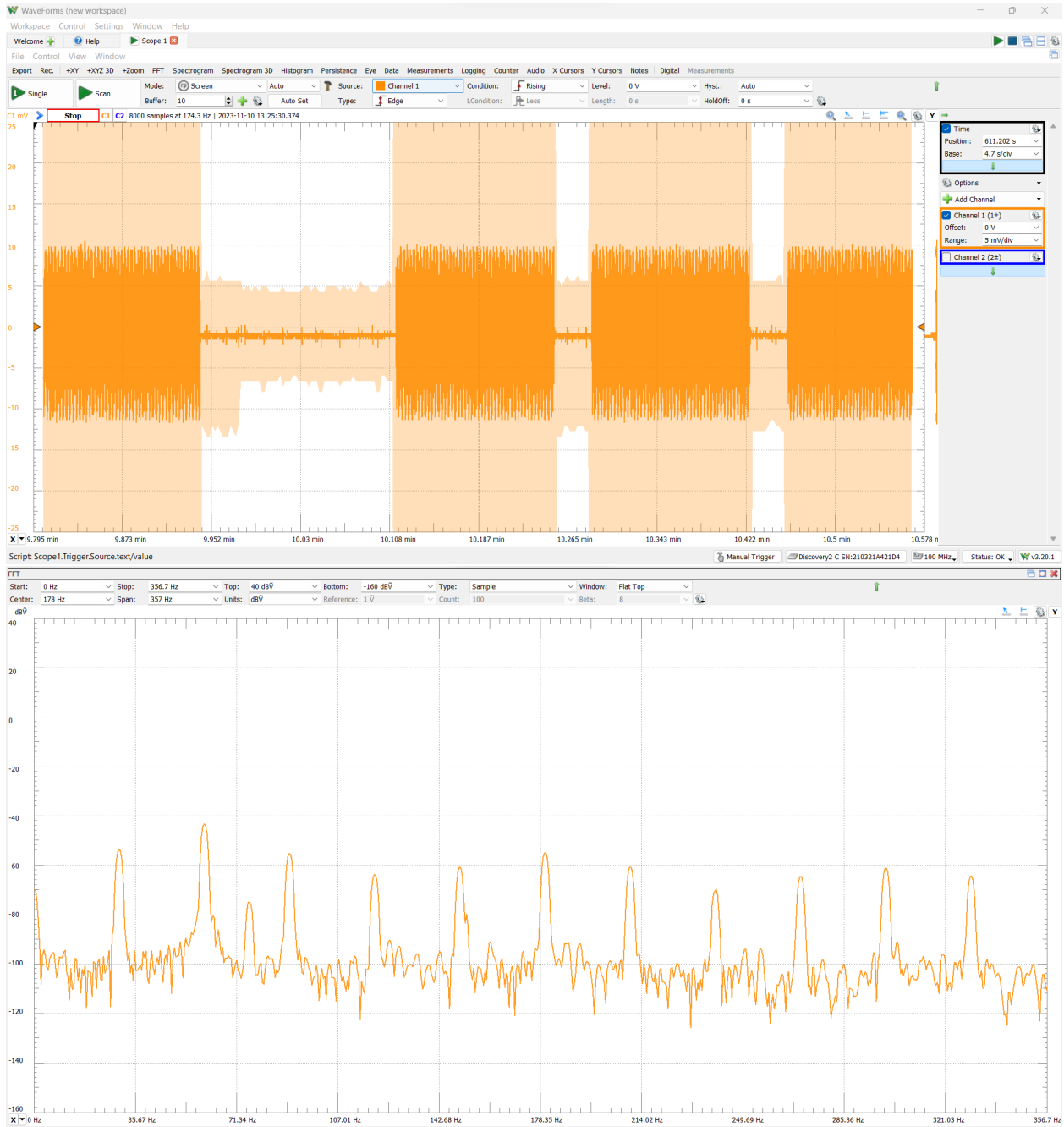


Figure 3.9 This image shows the signal from the TEM unit in the time domain (top) and the frequency domain (bottom). The frequency domain signal shows an initial peak around 33 Hz and harmonics at higher frequencies.

It is unclear what the source of the peak at 2265 Hz is. The use of a magnetometer in the field at a later date to determine if there was a background magnetic field at this frequency revealed no such field. It is a possibility that some electronics were running on the day of the survey that were not running on the date of return testing with the magnetometer.

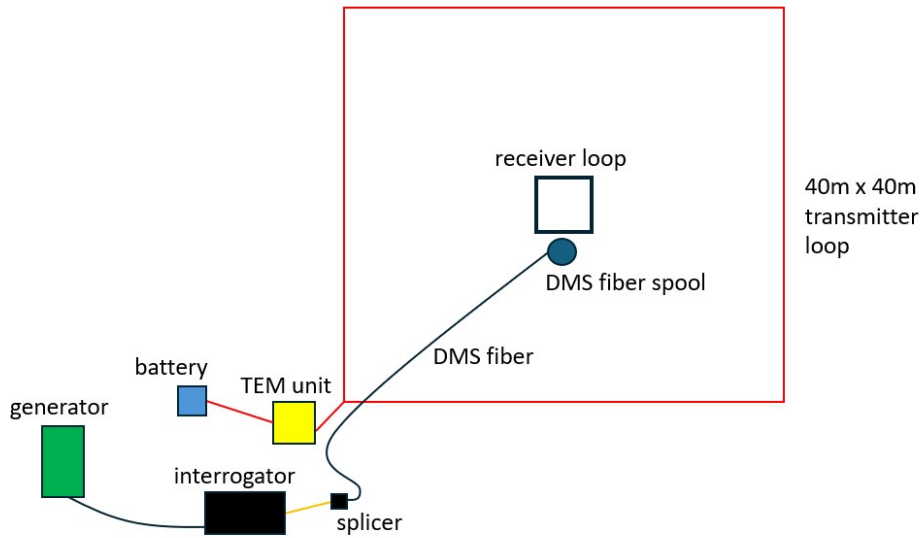


Figure 3.10 The top images show the first trial field setup. A diagram of the field setup is shown in the bottom image.

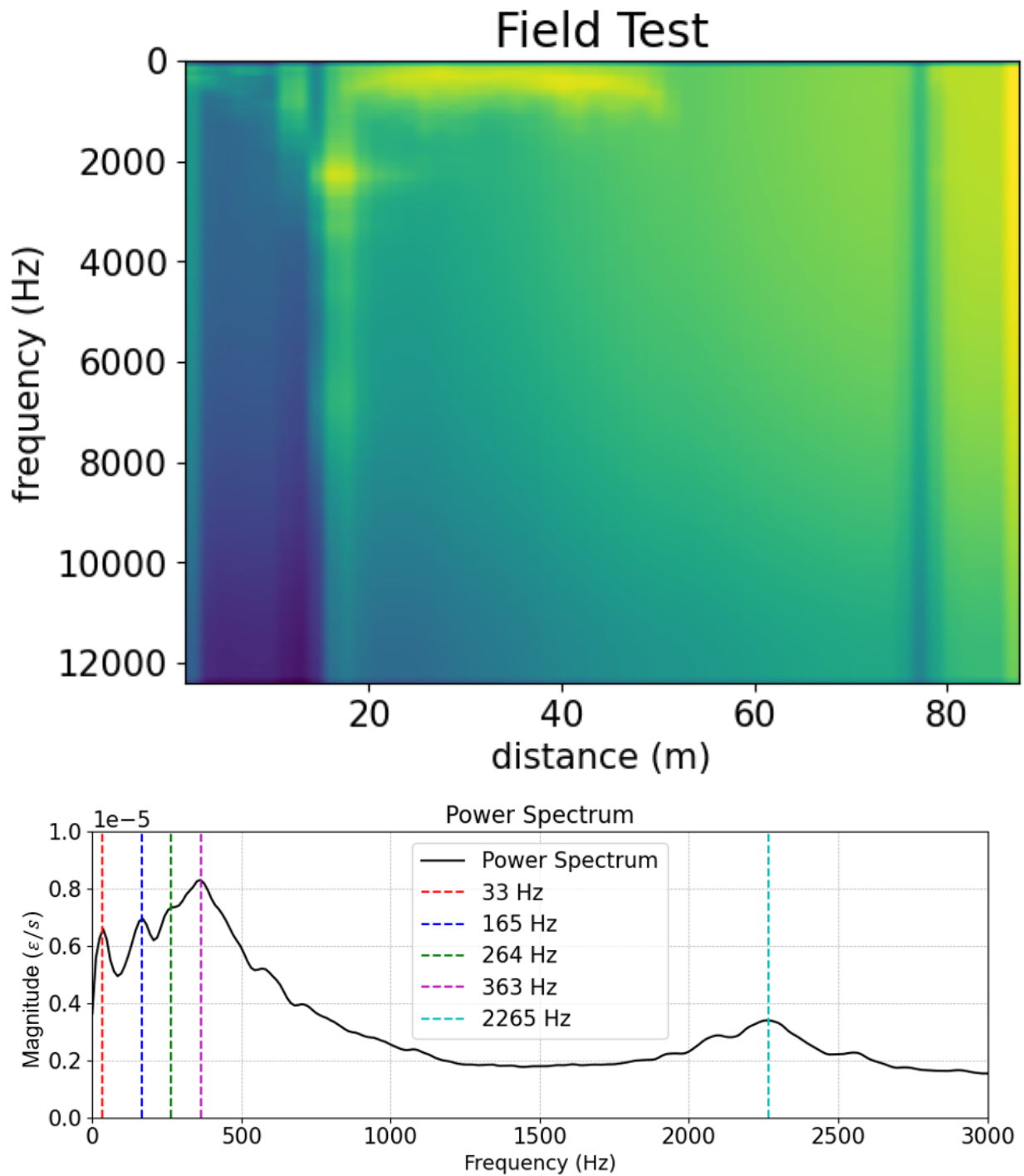


Figure 3.11 The frequency response of the entire length of the fiber (top) and power spectrum of channel 12 at 19.6 m (bottom) for the first trial are shown in this image.

3.2.2.2 Second Trial

The field experiment on Kafadar Commons at Colorado School of Mines, shown in Figure 3.12, was performed on November 10, 2023. We used a 20 m by 20 m loop with the WalkTEM in this experiment. The DMS fiber was laid out from the splicer to the center of the loop at $39^{\circ}44'59.0''\text{N}$, $105^{\circ}13'31.0''\text{W}$ to the corner of the loop due west of the interrogator, where the spool was set down. The interrogator was recording for a 25 minute period while TEM surveys were run multiple times.

The results of the test, shown in Figure 3.13, show some peaks that are slightly offset from the expected frequencies, as shown in Figure 3.11. For example, the expected 33 Hz peak is at 39 Hz, the expected 66 Hz peak is at 83 Hz, and the expected 99 Hz peak is at 126 Hz (closer to the next harmonic at 132 Hz). Each peak corresponds to a signal from a source with a frequency of ~ 40 Hz, however, the TEM source does not contain a magnetic field signal of this frequency. The cause of this offset is unknown, however, one possibility is a time shift due to an offset of the reported sampling rate of the interrogator.

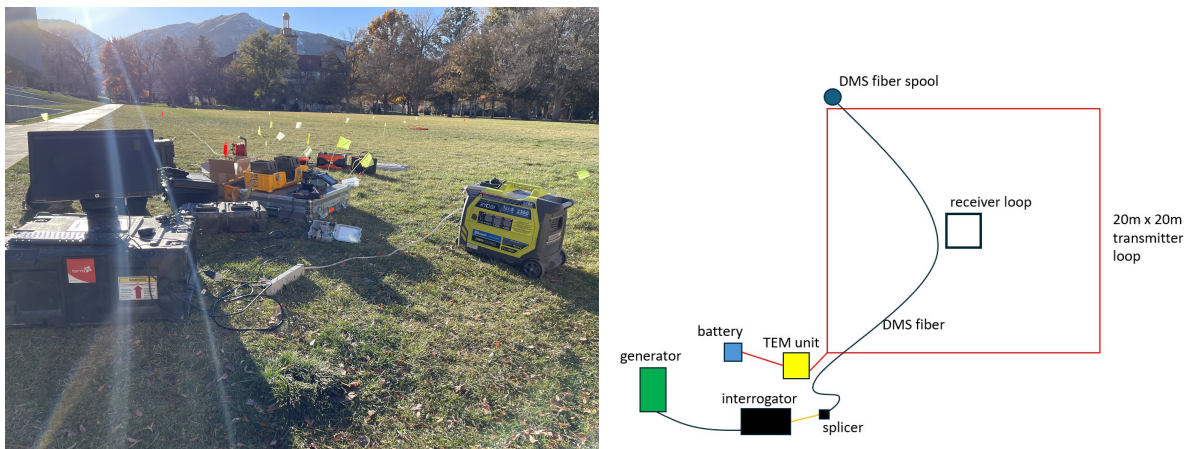


Figure 3.12 The field setup for the second trial (left) and a simplified diagram of the field setup (right) are shown in this image.

3.2.3 Field Experiment Results and Discussion

The results from the solenoid field experiments with the DMS fiber with Bragg gratings demonstrate that the DMS fiber is capable of reading a signal from solenoids. This is useful for future experiment design using the DMS fiber, setting goals for improving the DMS fiber sensitivity, and determining what applications the fiber can be used for. To image a signal from the soil, the sensitivity of the DMS fiber will need to be improved since typical soil magnetic susceptibilities (without magnetic minerals) are on the order of parts per million of the applied magnetic field (Shirzaditabar & Heck, 2021). Another solution would be to increase the source magnetic field strength; however, the strength would need to be increased a

few orders of magnitude which would limit where surveys could be performed due to safety and operational concerns.

The TEM experiments with the DMS fiber without Bragg gratings produced results with too much uncertainty to definitively say that a DMS fiber without Bragg gratings is capable of sensing a TEM signal. The power spectra in Figure 3.11 and Figure 3.13 contained peaks that were not at consistent harmonics of the TEM signal in the first trial and contained peaks that were offset from the expected signal in the second trial. Further experiments should be performed to determine how well a DMS fiber without Bragg gratings can sense the TEM signal. Additionally, experiments with a Bragg grating DMS fiber could be performed to determine if the Bragg gratings allow for better sensitivity of TEM signals.

There are currently some drawbacks with both sources which could be resolved in future studies. The solenoid produces relatively low magnetic fields outside of the coil when compared to the field strength inside the coil. This heavily limits the distance the DMS fiber can be placed from the solenoid. The TEM source has harmonics in the source, which causes signals to appear in the fiber response at those harmonic frequencies. Since these harmonics are not the result of a single source frequency, the source harmonics would have to be taken into account during data processing. Additionally, it is unclear what the frequency offset seen from the TEM source was caused by in the second TEM trial. More research into sources to be used with DMS is necessary to determine suitable data acquisition designs.

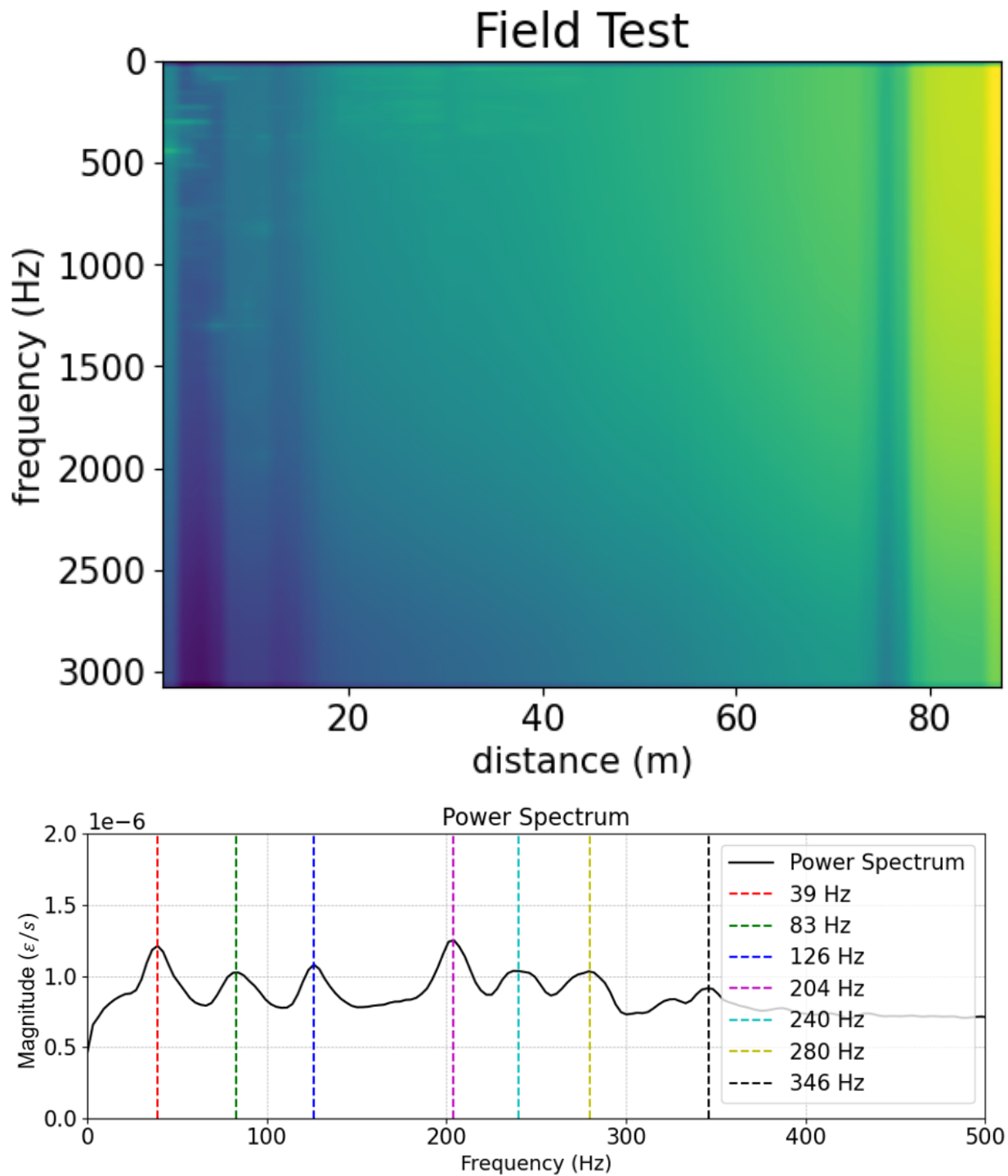


Figure 3.13 The frequency response of the entire length of the fiber (top) and power spectrum of channel 15 at 24.5 m (bottom) for the second trial are shown in this image.

CHAPTER 4
COMPUTATIONAL MODELING OF DMS

The theory to model DMS involves a combination of micromagnetics and DFOS principles. The computational modeling that was performed for this thesis focuses on micromagnetic concepts. The mechanical effects and optical response of the cable were excluded due to software limitations. We carry out two-dimensional and three-dimensional modeling, as well as sensitivity studies to a variety of parameters including initial conditions. Magnetic field amplitudes are in SI units (kA/m) in this chapter since the modeling equations required SI unit inputs, $1 \text{ mT} = 0.79577 \text{ kA/m}$. All single-sided amplitude spectra in this chapter are normalized by the number of samples and ε represents units of strain. The code used for the computational modeling in this chapter is provided in Appendix A.

4.1 Two-Dimensional Model

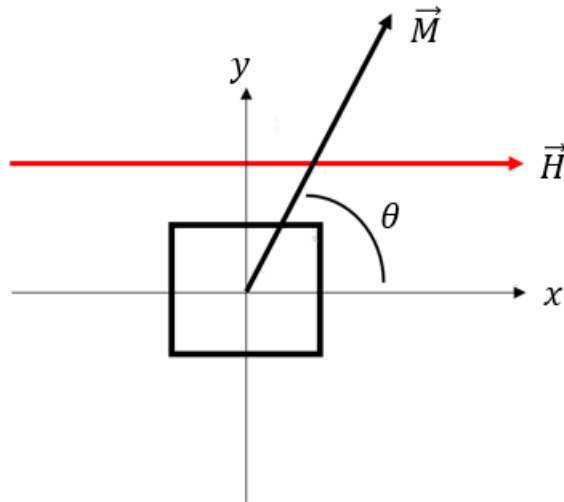


Figure 4.1 A visualization of the 2D model setup is shown in this image. The x direction is also the strain measurement direction, with saturation occurring in the direction of \vec{M} , where $\|\vec{M}\| = M_s$.

The single-domain model of magnetostriction assumes a piece of material in two dimensions that is magnetostrictively isotropic and homogeneous. For the simulations, nickel properties were used as the material properties. Consider a simple external magnetic source: a uni-directional, spatially uniform, alternating sinusoidal magnetic field, which is in the same direction as the strain measurement, as in

Figure 4.1. These assumptions simplify Equation 1.2 to

$$\frac{d\theta}{dt} = -\gamma \frac{1 + \alpha^2}{1 + \alpha} H_0 \sin(\omega t - \phi) \sin \theta. \quad (4.1)$$

Here, as in Equation 1.4, θ represents the angle between the measurement direction and the saturation direction. The two equations can be combined to solve for magnetostriction along a single axis. The other variables are the magnetic field amplitude of the source H_0 , source angular frequency ω , and phase of the source ϕ . To solve Equation 4.1, the Dormand-Prince method of solving ordinary differential equations (Dormand & Prince, 1980) is implemented with ode45 in MATLAB (The MathWorks, Inc., 2022). The resulting θ is then substituted into Equation 1.4 to solve for the strain response. A similar approach to solving for the dynamic magnetostriction response was used in Shoemaker (2018), with a different method to solve for θ , which was successful at predicting frequency doubling. However, we observe harmonics in real data - as seen in Chapter 3, Dejneka *et al.* (2024), and Hileman *et al.* (2022) - that were not modeled in Shoemaker (2018).

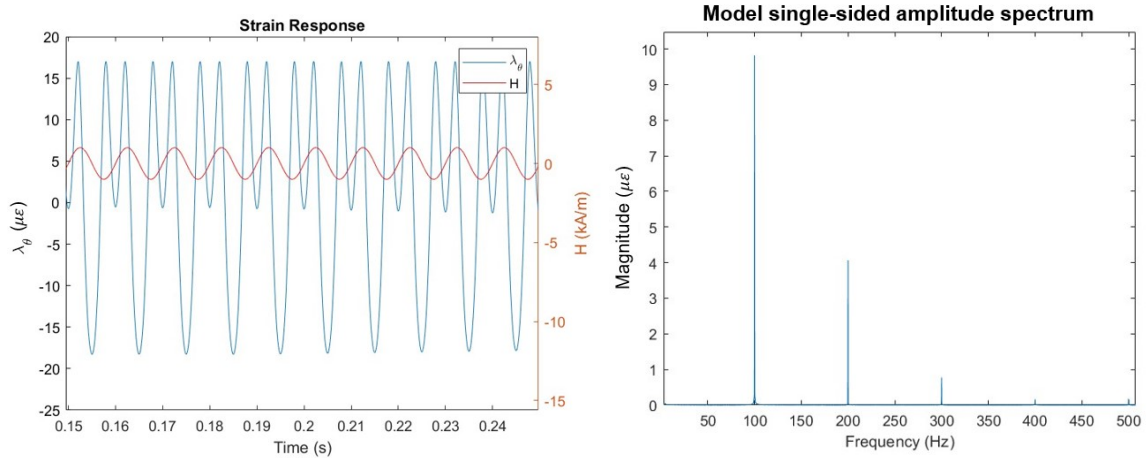


Figure 4.2 This figure shows an example of the modeled strain response to a source with a frequency of 100 Hz in the time domain (left) and the frequency domain (right). In the time domain, frequency doubling is apparent as two oscillations occur within 0.01 s. In the frequency domain, the spectrum shows clear peaks at 100 Hz, 200 Hz, and 300 Hz. Peaks at 400 Hz and 500 Hz are also present, though much smaller.

An example of the strain response of Nickel to a 100 Hz source with amplitude 1 kA/m and a phase of zero is shown in Figure 4.2. The initial angle was set to $\theta_0 = \pi/3$. The amplitude spectrum of the magnetostrictive response reveals strain oscillations occurring at the source frequency, double the source frequency, and at harmonics of the source frequency. The source frequency and double frequency responses are due to angular motions of the domain. The source frequency response is seen because the domain is rotating back and forth as the magnetic field source exerts a torque on the magnetic moment that changes direction. The double frequency response only occurs once a certain threshold ratio of the source frequency

and driving amplitude is met, for a given initial condition. If the threshold ratio is met or exceeded, the magnetic moment of the domain rotates a full π radians which, due to the geometry of the domain, causes there to be two peaks within a single period of the driving source. The harmonics can be explained through the non-linearity of the domain dynamics (Lakshmanan, 2011; Taylor, 2005). The number of harmonics that appear varies with the applied magnetic field strength, the source frequency, and the initial angle.

4.1.1 Applied Magnetic Field Sensitivity

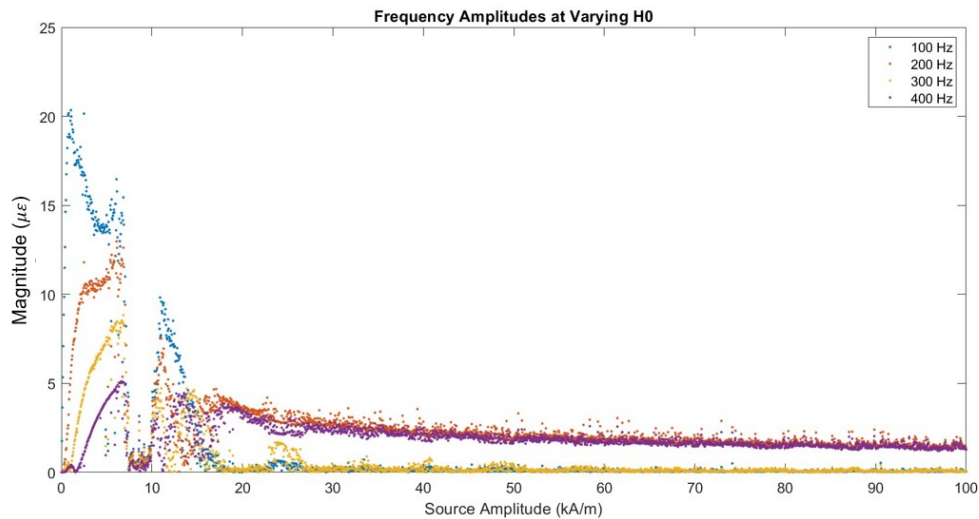


Figure 4.3 This image shows the variation of the response amplitudes at 100 Hz, 200 Hz, 300 Hz, and 400 Hz to a source with $f_s = 100$ Hz and magnetic field amplitude H_0 . All frequencies examined have peak amplitudes below 8 kA/m with a sudden drop in amplitude between 8 kA/m and 10 kA/m. All signals then increase at 10 kA/m then the even integer frequencies (i.e. $2f_s = 200$ Hz and $4f_s = 400$ Hz) dominate the signal for increasing H_0 .

The amplitudes of the signals in the amplitude spectrum are highly sensitive to changes in H_0 , the initial angle between \mathbf{M} and \mathbf{H} , θ_0 , and the source frequency, f_s . The response frequencies also have significant dependence on f_s . To demonstrate the dependence of the response amplitudes on H_0 , a suite of simulations showing the response amplitudes at several frequencies and many values of H_0 are shown in Figure 4.3. In these simulations, $f_s = 100$ Hz and $\theta_0 = \pi/3$. At values of H_0 below 8 kA/m, the response amplitudes generally show the harmonics increasing in amplitude as the 100 Hz response (i.e. the response at the driving frequency) decreases. Between 8 kA/m and 10 kA/m, all the response amplitudes decrease by approximately a factor of 10. Between 10 kA/m and about 18 kA/m, the response amplitudes increase again but evolve in a different manner. The harmonics lack an obvious trend in this region. At magnetic fields larger than 18 kA/m, the even harmonics (i.e. $2f_s = 200$ Hz and $4f_s = 400$ Hz) dominate the signal while the odd harmonics (only $3f_s = 300$ Hz in this example) have some spikes in amplitude at certain

values of H_0 . Since the response is largest and fairly predictable on the interval $1 \text{ kA/m} < H_0 < 8 \text{ kA/m}$, this suggests a favorable external magnetic field amplitude to target for future real measurements.

4.1.2 Initial Angle Sensitivity

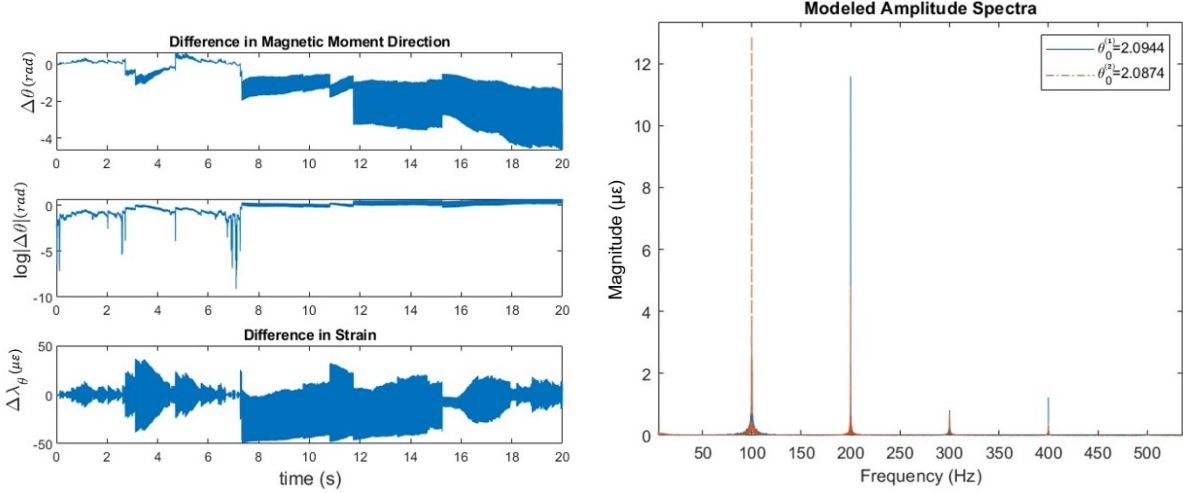


Figure 4.4 This figure demonstrates the difference in the response of two different initial conditions $\theta_0^{(1)} = 2\pi/3$ and $\theta_0^{(2)} = 2\pi/3.01$. The left image shows the difference of the magnetic moment direction over time for two simulations with the different initial conditions mentioned $\Delta\theta$, the log of the difference $\log|\Delta\theta|$ to show small scale variation, and the difference between the strain responses $\Delta\lambda_\theta$. The right image shows the amplitude spectra of both strain responses plotted on top of each other.

The nonlinear nature of the LLG equation causes the observed sensitivity to the source amplitude (Taylor, 2005). In addition, nonlinear equations can exhibit high sensitivity to initial conditions, θ_0 , in this model (Taylor, 2005). To demonstrate this sensitivity, the difference between the trajectories of θ over time between two different initial conditions $\theta_0^{(1)} = 2\pi/3$ and $\theta_0^{(2)} = 2\pi/3.01$ for $f_s = 100 \text{ Hz}$ and $H_0 = 10 \text{ kA/m}$ is shown in Figure 4.4. The trajectory of the magnetic dipole moments are similar initially, however, after about 7.5 s they begin to diverge. This also results in a difference in the strain response and amplitude spectra of the two simulations.

This is a typical trait of nonlinear systems (Taylor, 2005), suggesting that the system we are studying may be difficult to predict under certain conditions. More research into this needs to be performed to determine whether or not this system exhibits chaos. Some studies have demonstrated chaos arising from the LLG equation under certain conditions, e.g. Lakshmanan (2011) and Smith *et al.* (2010). It will be important to understand this response to interpret data from the fiber when it is deployed for real measurements. Since the response is more similar for different initial conditions within the first few seconds, it might be useful to take advantage of this time frame and record measurements for five or fewer

seconds when using a 100 Hz source.

4.1.3 Frequency Sensitivity

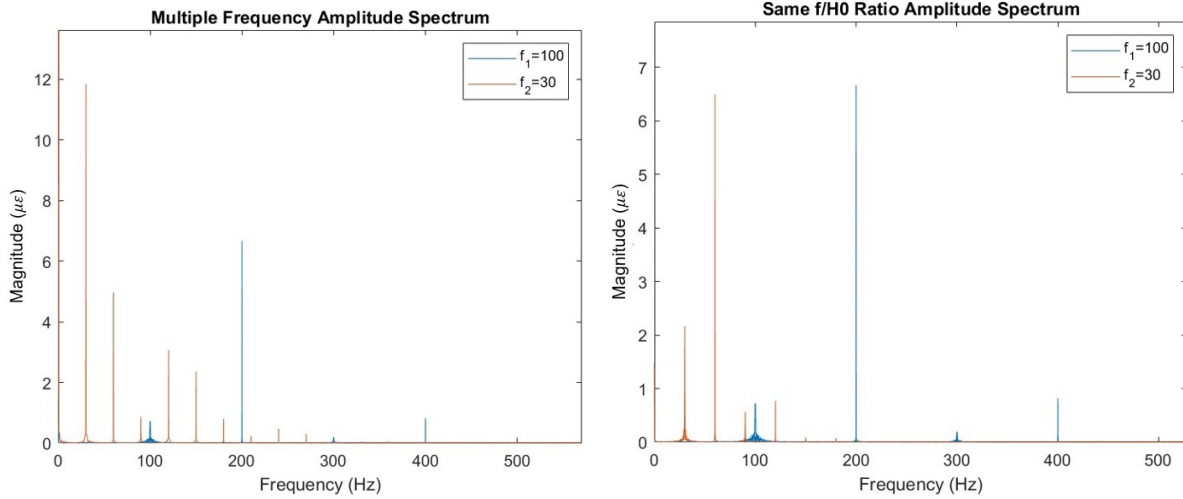


Figure 4.5 Amplitude spectra for two different source frequencies, f_1 and f_2 , are shown in this figure. The amplitude spectra with the same H_0 for each source frequency are shown on the left. There is a clear difference in the amplitude of the source frequency response, double frequency response, and harmonics. The amplitude spectra with the same ratio of f_s/H_0 are shown on the right. The f_1 and f_2 responses are similar with the same amount of significant harmonics.

The modeled responses exhibit an expected peak frequency dependence on f_s but also, interestingly, the dependence of the response *magnitude* on f_s . Two amplitude spectra for different source frequencies, $f_1 = 100$ Hz and $f_2 = 30$ Hz, at $H_0 = 1$ kA/m and $\theta_0 = 2\pi/3$ are shown in Figure 4.5. The response frequency dependence is apparent with responses to f_1 and f_2 at 100 Hz and 30 Hz, respectively, and harmonics at integer multiples of the source frequencies. There is an obvious difference in the amplitude of the fundamental frequency responses (100 Hz and 30 Hz) and the first harmonics (double-frequency, 200 Hz, and 60 Hz) responses with ratios of 0.06 and 1.3, respectively. There are also differences in the harmonic amplitudes between f_1 and f_2 in addition to the number of harmonics present - the response to f_2 shows five more harmonics than f_1 .

In the right panel of Figure 4.5, the amount of harmonics present in the amplitude spectra is similar for $f_1 = 100$ Hz and $f_2 = 30$ Hz, with $H_1 = 10$ kA/m and $H_2 = 3$ kA/m, i.e. for each simulation, the ratio of $f_s/H_0 = 10$. Both responses have the same number of significant response peaks; however, there are some small amplitude harmonics in the response to f_2 at 150 Hz and 180 Hz (≈ 0.08 amplitude) that are not visible in the response to f_1 . In addition, the relative amplitudes of the response frequencies are different, but much closer in magnitude than the first simulation where f_s/H_0 differs between source 1 and source 2.

The double frequency responses of the two sources are much closer in amplitude than the source frequency responses, suggesting the double frequency response may be less sensitive to changes in f_s/H_0 than to changes in the source frequency response. From this observation, we hypothesize that sources with similar ratios of f_s/H_0 may produce similar harmonic quantities in the amplitude spectrum; however, more research needs to be performed into this to confirm our hypothesis.

4.1.4 Discussion of the Two-Dimensional Model

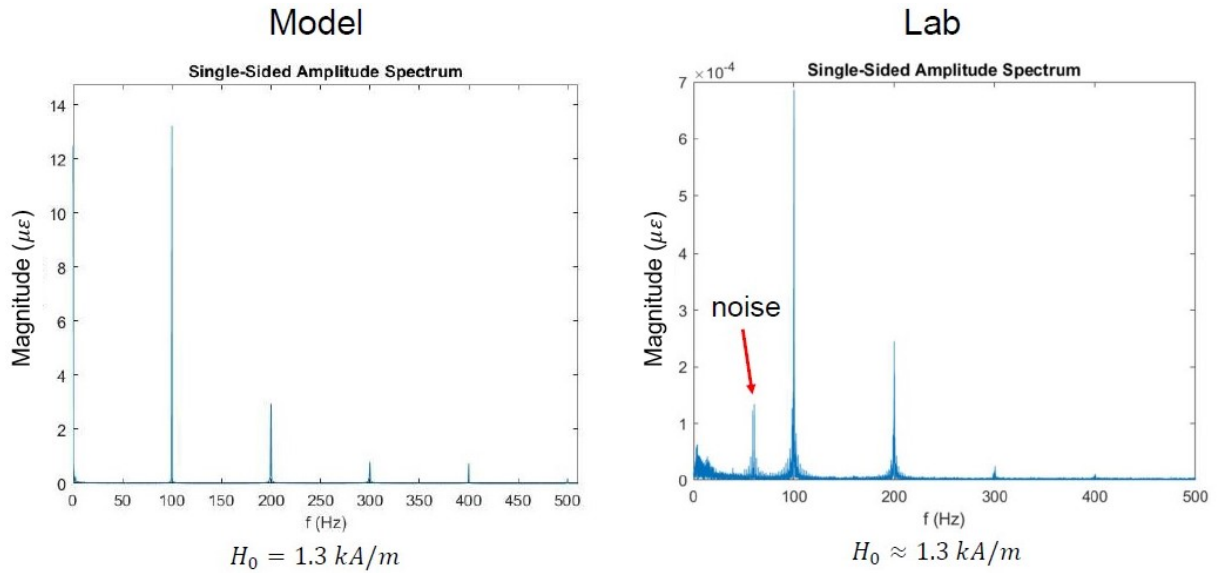


Figure 4.6 A two-dimensional model amplitude spectrum (left) and laboratory amplitude spectrum (right) of the fiber with two Nickel cladding wires and Bragg gratings to a 1.3 kA/m magnetic field ($1 \text{ mT} = 0.79577 \text{ kA/m}$) are shown in this figure. The noise in the lab response is at 60 Hz and is attributable to electrical noise from the building. The base noise level in the laboratory amplitude spectrum is $\sim 10^{-5} \mu\text{E}$. Note the difference in magnitude scale between the model and laboratory amplitude spectra (the laboratory amplitude spectrum is courtesy of Zachary Dejneka).

An example comparison between the model amplitude spectrum and laboratory results for a DMS fiber with Bragg gratings is shown in Figure 4.6. While the model predicts a response with peaks at the same frequencies as the laboratory, there is one main difference observed: the model prediction of the relative amplitude between the peak at the source frequency, $f_1 = 100 \text{ Hz}$, and double the source frequency, $f_2 = 200 \text{ Hz}$, is $|P1(f_1)|/|P1(f_2)| \approx 4.5$, which is larger than observed in the laboratory, $|P1(f_1)|/|P1(f_2)| \approx 2.5$. While this two-dimensional modeling begins to show some of the features observed in the laboratory and field, further analysis is needed to carry out quantitative predictive modeling of the data we expect to record in any controlled-source experiment. Such predictive modeling is an essential element of any inversion procedure.

These model limitations are thought to be attributable to the lack of multiple domains in the two-dimensional model, which excludes domain interactions from the model. In reality, many domain interactions occur, changing the overall response of the ferromagnetic material to magnetic fields. To account for the domain interactions, including multiple domains in the two-dimensional model or using a three-dimensional model is necessary. This spurred us to build a three-dimensional model with current software capable of doing so. The three-dimensional model is discussed in the following section. Further analysis of the two-dimensional model was performed and is discussed in Appendix D.

4.2 Three-Dimensional Model

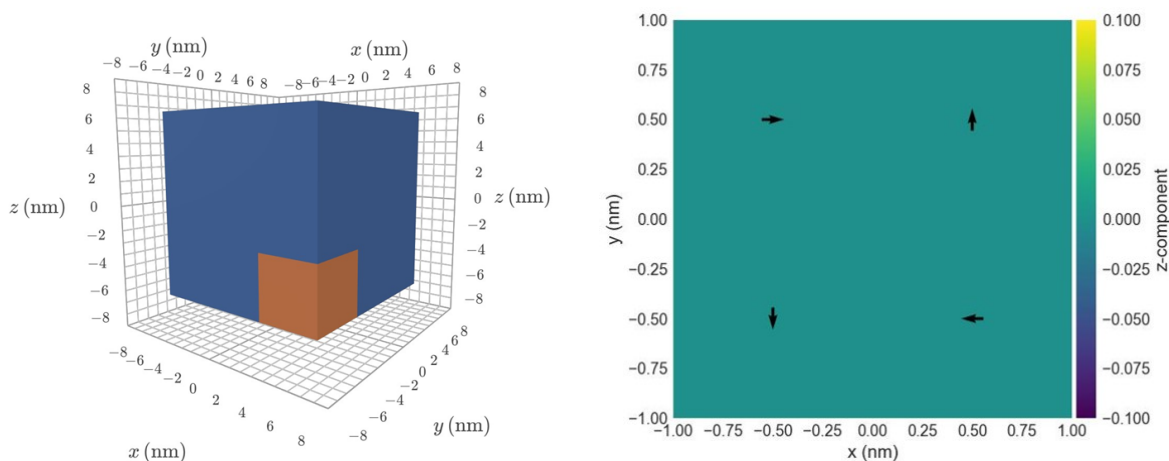


Figure 4.7 This figure shows a mesh of three-dimensional cells defined in Ubermag (left) and a slice of the model at $z = 0$ nm (right). The slice shows the demagnetized case, with all magnetic dipole moments adding to a net zero moment.

Ubermag is an open-source micromagnetic three-dimensional modeling package (Beg *et al.*, 2022) that includes more complex modeling capabilities than those implemented in the two-dimensional model. In the two-dimensional model we did not specify the geometry of the material, the size of the domains, or the other fields that make up the effective field. In Ubermag, it is possible to define a three-dimensional grid of domains and run simulations from an initially demagnetized state, as shown in Figure 4.7. This capability allows the model to account for domain interactions within a material along with material geometry. Ubermag also includes the demagnetization field, anisotropy field, exchange field, and the Zeeman (applied) field in the effective field. These fields arise in bulk materials in magnetics and are important to include because they change the dynamics of the magnetic moments, and thus the magnetostrictive response.

The mathematical forms of the field energies are (Beg *et al.*, 2022):

$$w_z = -\mu_0 M_s \mathbf{m} \cdot \mathbf{H}, \quad (4.2)$$

$$w_e = A(\nabla \mathbf{m})^2, \quad (4.3)$$

$$w_{ca} = -K_1 [(\mathbf{m} \cdot \mathbf{u}_1)^2(\mathbf{m} \cdot \mathbf{u}_2)^2 + (\mathbf{m} \cdot \mathbf{u}_2)^2(\mathbf{m} \cdot \mathbf{u}_3)^2 + (\mathbf{m} \cdot \mathbf{u}_1)^2(\mathbf{m} \cdot \mathbf{u}_3)^2], \quad (4.4)$$

$$w_d = \frac{1}{2} \mu_0 M_s \mathbf{m} \cdot \mathbf{H}_d. \quad (4.5)$$

The energies are the Zeeman energy w_z , the exchange energy w_e , the cubic anisotropy energy w_{ca} , and the demagnetization energy w_d . In addition, $\mathbf{m} = \mathbf{M}/M_s$ is the normalized magnetization vector, A is the exchange constant, K_1 is the anisotropy constant, \mathbf{H} is the external magnetic field, \mathbf{u} is the direction of the axis of anisotropy, and \mathbf{H}_d is the demagnetizing field. To solve for the effective field from the energy, we substitute the total energy E_{tot} into

$$\mathbf{H}_{eff} = -\frac{1}{\mu_0 M_s} \frac{\partial E_{tot}}{\partial \mathbf{m}}, \quad (4.6)$$

as in Liang *et al.* (2014). Substituting the result for \mathbf{H}_{eff} from Equation 4.6 into Equation 1.2 at each time-step allows us to solve for \mathbf{M} at each timestep. The resulting magnetic moment magnitudes are substituted into a version of Equation 1.3 replacing all α_i with m_i ,

$$\lambda_{si} = \frac{3}{2} \lambda_{100} \left(m_1^2 \beta_1^2 + m_2^2 \beta_2^2 + m_3^2 \beta_3^2 - \frac{1}{3} \right) + 3 \lambda_{111} (m_1 m_2 \beta_1 \beta_2 + m_2 m_3 \beta_2 \beta_3 + m_3 m_1 \beta_3 \beta_1), \quad (4.7)$$

to solve for strain, then the magnitude of the discrete Fourier transform (DFT) is calculated to create an amplitude spectrum of the strain response (COMSOL, 2023).

One limitation of the three-dimensional model is that the spatial scale of the cells must be smaller than the width of domain walls in the material (Abert, 2019)

$$l = \sqrt{\frac{A}{K_{eff}}}, \quad (4.8)$$

where A is the exchange constant and K_{eff} is the effective anisotropy constant. For nickel, l is on the order of $\sim 10^{-7}$ m, meaning the cell sizes must have sides smaller than ~ 100 nm. This presents an issue for modeling the fiber response since the magnetostrictive wires have diameters on the order of $\sim 10 \mu\text{m}$ and the complexity of the three-dimensional model increases on the order of n^2 , where n is the number of cells, due to the long-range nature of the demagnetization field (Abert, 2019). Being limited to small cell sizes, modeling the actual size of the fiber may be infeasible with this model, but modeling smaller elements may provide initial insights into the trends we expect to observe in real data. Additionally, the timestep used in the solver must be sufficiently small to satisfy the Nyquist sampling condition of two samples per period of

the magnetization vector precessional motion (Scholz *et al.*, 2003), which has a Larmor frequency of

$$\omega = \gamma \mathbf{H}_{eff}. \quad (4.9)$$

The magnetic field strengths tested in the lab are 2 kA/m and lower, resulting in a Larmor frequency on the order of 5000 Hz, meaning the sampling rate must be 10000 Hz to model the physics correctly. In practice, we implement higher sampling frequencies than the Nyquist limit to ensure numerical accuracy. For lower magnetic field strengths, the sampling rate can be decreased according to the Larmor frequency.

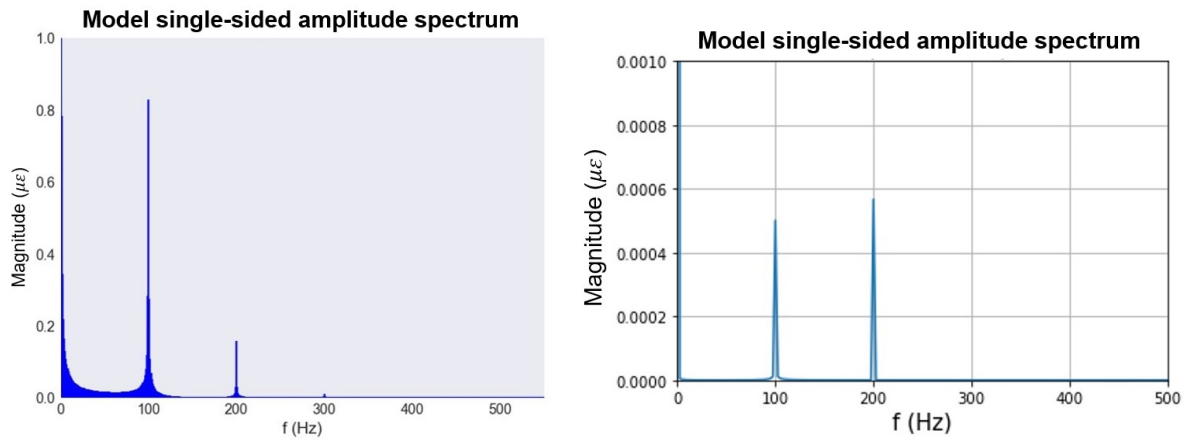


Figure 4.8 This figure shows amplitude spectra produced from the three-dimensional model for a magnetized block (left) and demagnetized block (right). The source frequency was 100 Hz with an amplitude of 1.3 kA/m. The demagnetized amplitude spectrum contains lower amplitude peaks than the magnetized amplitude spectrum, closer to the amplitudes seen in the laboratory results for the same magnetic field source, shown in Figure 4.6.

Example amplitude spectra are shown in Figure 4.8 for a source of amplitude 1.3 kA/m and frequency 100 Hz applied along the z-axis. These spectra show responses to demagnetized and magnetized initial conditions. In the demagnetized scenario, domain magnetic moments point in different directions initially, summing to a net zero initial magnetization. In the magnetized scenario, all domain magnetic moments point in the same direction, creating an initial magnetization of M_s . In both cases, there is a clear peak at the source frequency (100 Hz) along with a double frequency peak (200 Hz). The magnetized amplitude spectrum contains one harmonic at 300 Hz, whereas the demagnetized case contains no harmonics.

The demagnetized amplitude spectrum contains peaks on a lower order of magnitude, $\sim 10^{-4} \mu E$ than the magnetized amplitude spectrum. Additionally, the amplitude spectrum does not contain any harmonics, which is inconsistent with laboratory results. Larger magnetic fields of about ten times those used to create the amplitude spectrum in Figure 4.8 are required to generate harmonics in the amplitude spectrum of the demagnetized block. On the other hand, the magnetized amplitude spectrum contains one harmonic at 300 Hz. These initial results lead us to explore the parameter sensitivity of the model,

discussed further in this chapter, to generate amplitude spectra with more accurate prediction capabilities.

Sensitivity analysis to the applied magnetic field and the Gilbert damping parameter, α , are explored further. α changes with the material temperature (Cochran *et al.*, 1991; Mankovsky *et al.*, 2013) and the amplitude of the applied magnetic field (Djordjevic *et al.*, 2006). To account for temperature changes, the experimental relationship between α and temperature was used based on Mankovsky *et al.* (2013). Changes of α with the amplitude of the applied magnetic field were not accounted for in this model.

4.2.1 Applied Magnetic Field Sensitivity

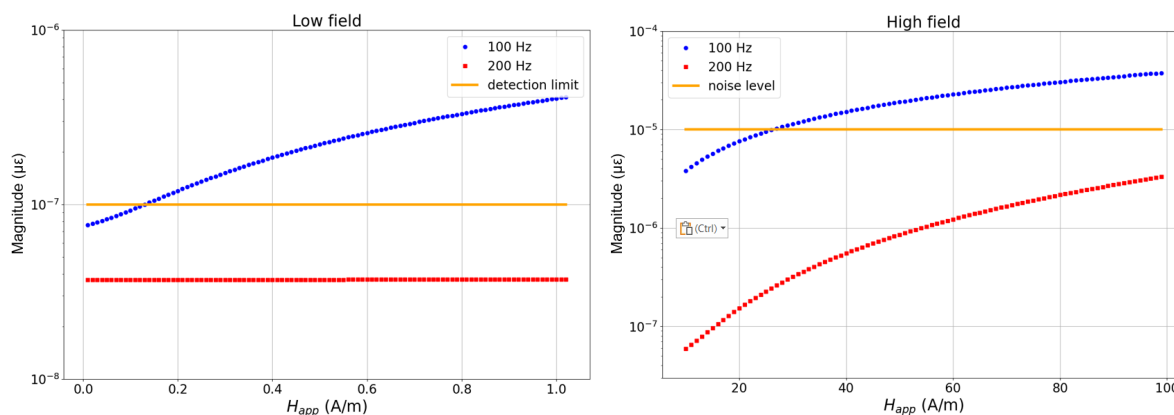


Figure 4.9 These plots show the variation of the 100 Hz and 200 Hz peaks for 0.01 A/m to 1.02 A/m (left) and 10 A/m to 98 A/m (right) from three-dimensional model outputs. The orange line in the low field case is indicative of the magnetic field amplitude at which the 100 Hz signal is visible in the model amplitude spectrum. The orange line in the high field case indicates the magnetic field strength at which the 100 Hz signal matches the noise level.

Simulations were performed for a three-dimensional block of material given the properties of nickel, eight cubic domains, and a domain side length of 1 nm. The model applied different magnetic field strengths to the material and the magnitudes of the modeled 100 Hz and 200 Hz responses are shown in Figure 4.9. The 100 Hz signal appeared in the model at a magnetic field strength of 0.14 A/m, however, the 100 Hz signal magnitude was equal to a noise level of $\sim 10^{-5} \mu\epsilon$, shown in Figure 4.6, at a magnetic field amplitude of 26 A/m ($1 \text{ mT} = 795.77 \text{ A/m}$). The minimum magnetic field amplitude that the nickel DMS fiber with two cladding wires and Bragg gratings has been shown to sense in the lab is $\sim 80 \text{ A/m}$ ($\sim 0.1 \text{ mT}$), which is a 100 Hz amplitude spectrum response to a 100 Hz source frequency (Hileman *et al.*, 2022). The 100 Hz amplitude is detectable at higher magnetic fields than the model predicts. The model also predicts that the 100 Hz response appears at lower magnetic fields than the 200 Hz response, which matches laboratory observations discussed in Chapter 3 and Dejneka *et al.* (2024).

The models that have been run likely are not capable of exactly predicting the correct magnetic field strength because of a scale issue - the model is about 1000 orders of magnitude smaller than the fiber magnetic wires. Because of this scale difference, it is not possible to include the number of domains that would be present in the nickel cladding wires in reality. Since the domains have a magnetic field that has the lowest energy state when all domains are aligned, more domains in a system mean that the material is less susceptible to lower external magnetic fields due to skin depth (Cullity & Graham, 2009). This is part of the reason why the model with only eight domains shows a response to lower magnetic fields than the lab experiments do.

4.2.2 Damping Parameter Sensitivity

The Gilbert damping parameter is not a constant material property, so parameter sensitivity simulations were performed to determine how much the results depend on α . In these simulations, the amplitudes of the 100 Hz, 200 Hz, 300 Hz, 400 Hz, and 500 Hz amplitude spectrum responses to a 100 Hz source of amplitude 10 kA/m were recorded and plotted against α , as in Figure 4.10.

Increasing the damping parameter varies the number of peaks that appear in the amplitude spectrum of the three-dimensional model results, as shown in Figure 4.10. The number of peaks seems unpredictable for a given damping parameter. The variation in the number of peaks does not show a clear trend with some time domain signal issues at certain values of the damping parameter. In cases where there is a time domain signal issue, the time domain response demonstrates random oscillations with no discernible periodic behavior. Calculating the amplitude spectrum of these cases produces results that do not show a clear signal in the amplitude spectrum.

From the results, it seems that the model is highly sensitive to changes in α . This is slightly problematic for modeling the DMS fiber response accurately because the exact value of α varies substantially, depending on temperature, material geometry, and magnetic field strength. The next section will discuss sensitivity to temperature changes, however, additional studies must be performed to understand the role of material geometry and magnetic field strength.

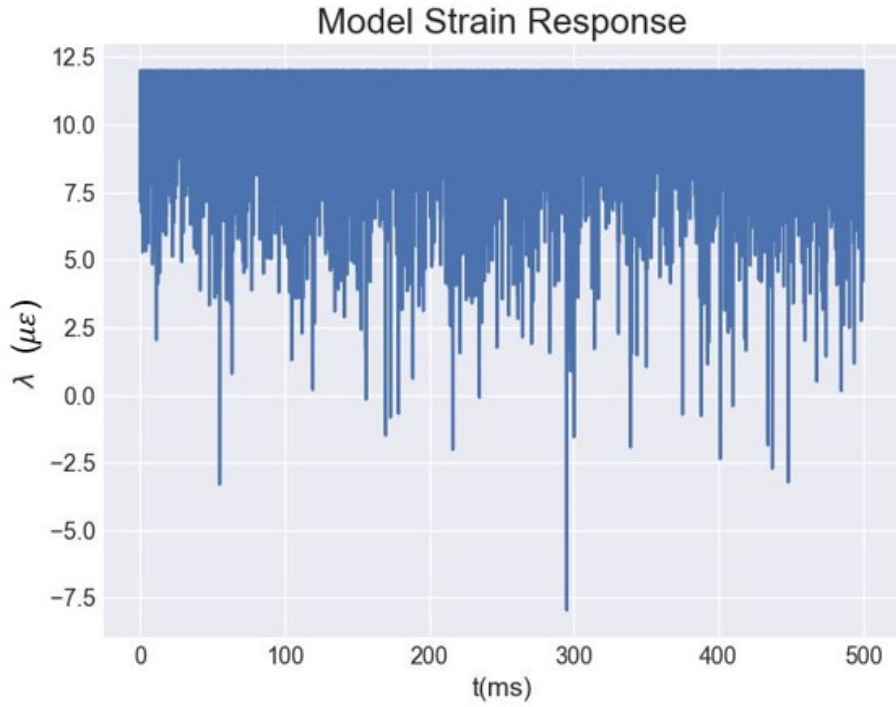
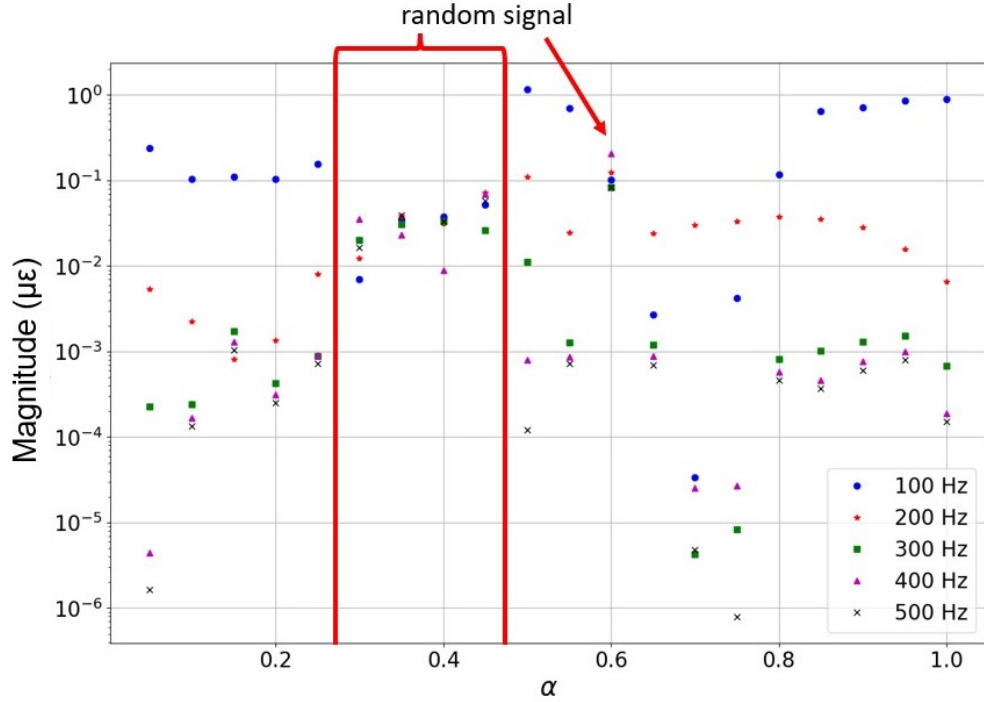


Figure 4.10 Changing the damping parameter can result in the appearance of more or less harmonics in the three-dimensional model ($H_0 = 10$ kA/m). This figure shows how the amplitudes of the peaks in the amplitude spectrum change based on α (top). Some signal issues appear at certain values of α , producing a random time domain signal, as indicated in the top image. An example random time domain signal is shown in the bottom image.

4.2.3 Temperature Dependence

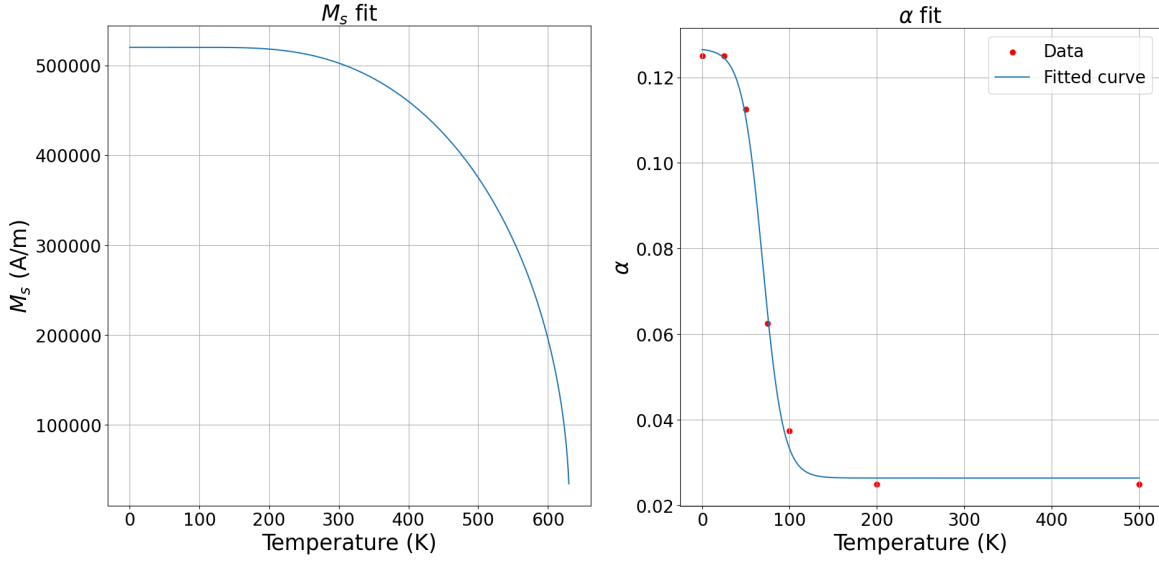


Figure 4.11 These plots show the modeled relationship between temperature and M_s (left), adapted from Cullity & Graham (2009), and temperature and α (right), adapted from Mankovsky *et al.* (2013), for nickel.

Temperature modeling of the DMS fiber was performed using known relationships between M_s and α with temperature (Cullity & Graham, 2009; Mankovsky *et al.*, 2013). The data from the sources cited was unavailable to us, so values for M_s were calculated for a given temperature using

$$M_s = M_0 [m - \tanh(m/t)], \quad (4.10)$$

where M_0 is the magnetization saturation at 0K, $m = M_s/M_0$, and $t = T/T_c$ with T_c representing the Curie temperature. The data for α as a function of temperature was fit to a Sigmoid function, resulting in the relationship for nickel

$$\alpha(T) = 0.12677279 - \frac{0.10035642}{(1 + e^{-0.0851499(T-69.35616788)})}. \quad (4.11)$$

Figure 4.11 shows the plots resulting from equations 4.10 and 4.11. These functions approximate the data reasonably well when compared to the original images. The amplitudes of the first two peaks of the amplitude spectrum produced by the temperature model for Nickel at an applied magnetic field amplitude of $H = 10$ kA/m and a frequency of 100 Hz are shown in Figure 4.12. There is not a significant amount of variation in the amplitude spectrum over the temperature range tested, which suggests that the signal does not show high dependence on temperature fluctuations from -40°C to 50°C .

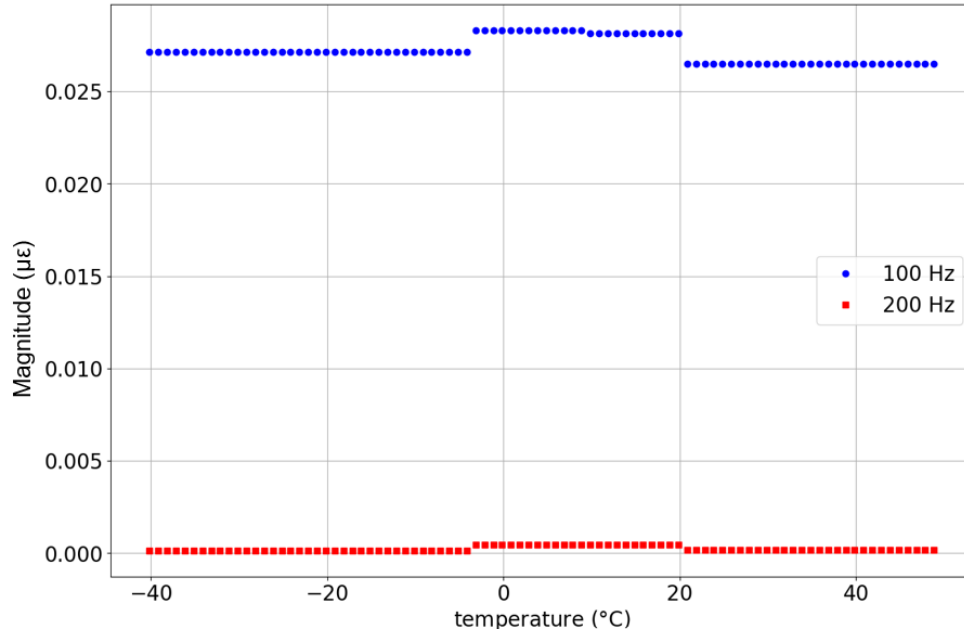


Figure 4.12 The amplitudes of the 100 Hz and 200 Hz peaks in the amplitude spectrum for simulations at different temperatures are shown in this image. The field amplitude was set to 10 kA/m and a source frequency of 100 Hz. There are only small variations in these peak amplitudes from -40°C to 50°C

4.2.4 Discussion of the Three-Dimensional Model

Comparison of the three-dimensional model amplitude spectra in Figure 4.8 to the laboratory spectrum in Figure 4.6, reveals that the three-dimensional model is better at predicting relative amplitudes than the two-dimensional model for a nickel DMS fiber with Bragg gratings. However, it does not come without its limitations. These include longer computation time than the two-dimensional model and model size limitations. Another limitation in application is uncertainty in the value of a high sensitivity parameter, α . The uncertainty of α also applies to the two-dimensional model, but the two-dimensional model does not show high sensitivity to α .

The computation time of the three-dimensional model is on the order of minutes to hours as opposed to the few seconds that the two-dimensional model takes to run. This limits how many simulations can be performed by the three-dimensional model in the same amount of time. Additionally, if a larger model is required than the simple cube model discussed in this section, the computation time increases greatly, making it difficult to model the actual scale of the fiber. It is possible that future studies could address this through implementation with parallel computing.

The uncertainty in the value of α is perhaps the most concerning issue. One way of solving this issue without waiting for new research to be published in this area might be to optimize the value of alpha based

on input data from the lab. This would only work if all other parameters are known well and if the simulations produce amplitude spectra that represent the lab data well. Future efforts could be dedicated to the development of α optimization code.

CHAPTER 5

SUMMARY AND CONCLUSION

In this thesis, four key aspects of DMS were explored: (1) potential application areas for DMS were evaluated using magnetic simulation methods, (2) laboratory experiments were performed to determine the sensitivity and time dependence of the signal from a two Metglas cladding wire DMS fiber without Bragg gratings, (3) field tests were performed with a DMS fiber with Bragg gratings and without Bragg gratings to determine feasibility in field application, and (4) computational modeling of DMS was performed to increase the understanding of the physical mechanisms that produce a signal in a DMS fiber.

5.1 Summary of Results

Chapter 2 provides insight into some potential application areas of DMS: seawater intrusion monitoring, mine drainage monitoring, and lithium brine mining. A survey design involving the deployment of a DMS fiber into a horizontal borehole to create a long was proposed. Through simulations, it was found that a dense array of magnetic field sensors placed beneath the groundwater table is capable of imaging boundaries between freshwater and (1) seawater, (2) a solution of Fe^{2+} ions with a concentration greater than 100 mg/L, and (3) a solution of Li^+ ions with concentrations typical of economical brines (200 mg/L to 1500 mg/L).

Section 3.1 discusses laboratory experiments with DMS fiber with two Metglas cladding wires and no Bragg gratings. These experiments found the magnetic field sensitivity of the fiber to be 0.2 mT, which is lower than the sensitivity of a prototype fiber with Bragg gratings of 500 nT (Dejneka *et al.*, 2024). Experiments were also performed to determine the variation of the signal from the fiber without Bragg gratings over time. It was found that peak amplitudes change over time in the amplitude spectrum. Depending on the noise level, these changes can be large enough to make the signal undetectable at some points in time even though it is detectable at other times.

Section 3.2 discusses field experiments performed with the DMS fiber with two Metglas cladding wires. Field experiments with a solenoid and the fiber with Bragg gratings demonstrated that a solenoid elicits a response in the DMS fiber up to 0.5 m away from the solenoid. Field experiments with TEM as a source and a DMS fiber without Bragg gratings produced results with too much uncertainty to definitively say that a DMS fiber without Bragg gratings is capable of sensing a TEM signal.

Chapter 4 provides insight into the physical mechanisms behind the DMS fiber response through two-dimensional and three-dimensional computational modeling. Model sensitivities to external magnetic

field strengths, initial conditions, source frequency, temperature, and the Gilbert damping parameter were explored. Comparisons of the three-dimensional and two-dimensional model to laboratory results for a DMS fiber with two nickel cladding wires and Bragg gratings reveal that the three-dimensional model performs better at predicting the relative magnitude of peaks in the amplitude spectrum. However, the three-dimensional model requires more computational time than the two-dimensional. Both models predict harmonics in the amplitude spectrum, as seen in laboratory experiments.

5.2 Future Work

Further research into DMS that could build on the work discussed in this thesis includes avenues of application simulation, laboratory tests, field tests, and computational modeling.

Applications in seawater intrusion monitoring, mine drainage monitoring, and lithium brine monitoring were considered in this thesis. The models could be improved to represent more realistic application conditions in a few ways. For all applications considered, future models could incorporate alternating magnetic fields to replicate optimal conditions for the DMS fiber. Models can also include gradients of concentration for the mine drainage and lithium brine monitoring application areas to simulate more realistic conditions. Future models could also include potential noise sources in the TMI anomaly results. It would be of interest to create a model for a vertical borehole as well since vertical boreholes are more commonly implemented in hydrogeology. Most importantly, future models should apply an external magnetic field only to the borehole to simulate where the magnetic field would be applied in real applications given an easily available solenoid source, discussed further in Appendix E. Finally, further application areas mentioned in Dejneka *et al.* (2024) can be modeled to support the feasibility of DMS surveys in these application areas.

Laboratory tests to determine the magnetic field sensitivity of the DMS fiber with two Metglas cladding wires without Bragg gratings were only performed for a source frequency of 1000 Hz in this thesis due to laboratory equipment limitations. Future testing could determine sensitivity at lower source frequencies with appropriate laboratory equipment. Of particular interest, magnetic field sensitivity could also be determined at the operational frequencies of commercial magnetic susceptibility meters, e.g. the Kappabridge MFK2 which operates at 976 Hz, 3904 Hz, and 15616 Hz. Laboratory experiments to determine the fiber response when the fiber is in water with different concentrations of salt, Fe^{2+} , or Li^{+} would provide support for the application areas simulated in this thesis. Finally, the method of manual fiber alignment in the laboratory made it difficult to perform tests. Refinement of the manual fiber alignment method or the use of fiber connectors could solve this issue.

Field tests of the Metglas DMS fiber with Bragg gratings and a TEM source can be performed in the future. The higher sensitivity of the Bragg grating fiber may clarify uncertainties in field test results found in the results produced by the fiber without Bragg gratings. Other geophysical sources should be considered as well for future field tests. Testing of the DMS fiber in the application areas explored with simulations would also be valuable, provided the sensitivity of the DMS fiber improves with future research.

Further computational modeling efforts of the DMS response would be valuable for improving the modeled fiber response and integration into geophysical schemes. These efforts may be best directed toward the refinement of the three-dimensional model. Including realistic cladding wire geometry and refinement of the Gilbert damping parameter, α , with an α optimization code may be promising research avenues. Additional efforts could include DAS principles in the modeling code.

REFERENCES

- Abert, Claas. 2019. Micromagnetics and spintronics: models and numerical methods. *The European Physical Journal B*, **92**(120).
- Accomando, Filippo, & Florio, Giovanni. 2024. Applicability of Small and Low-Cost Magnetic Sensors to Geophysical Exploration. *Sensors*, **24**(21).
- Affandi, Fatin, Mohd Kusin, Faradiella, Sulong, Nur, & Madzin, Zafira. 2018. Hydrogeochemical assessment of mine-impacted water and sediment of iron ore mining. *IOP Conference Series: Earth and Environmental Science*, **140**(04), 012023.
- Allouche, Erez N., Ariaratnam, Samuel T., & Lueke, Jason S. 2000. Horizontal Directional Drilling: Profile of an Emerging Industry. *Journal of Construction Engineering and Management*, **126**(1), 68–76.
- Anderson, Mary P., Woessner, William W., & Hunt, Randall J. 2015. Chapter 4 - Model Dimensionality and Setting Boundaries. *Pages 117–180 of: Anderson, Mary P., Woessner, William W., & Hunt, Randall J. (eds), Applied Groundwater Modeling (Second Edition)*, second edition edn. San Diego: Academic Press.
- Bao, Xiaoyi, & Chen, Liang. 2012. Recent Progress in Distributed Fiber Optic Sensors. *Sensors*, **12**(7), 8601–8639.
- Beg, Marijan, Lang, Martin, & Fangohr, Hans. 2022. Ubermag: Towards more effective micromagnetic workflows. *IEEE Transactions on Magnetics*, **58**(2), 1–5.
- Bityukova, L., Scholger, R., & Birke, M. 1999. Magnetic susceptibility as indicator of environmental pollution of soils in Tallinn. *Physics and Chemistry of the Earth, Part A: Solid Earth and Geodesy*, **24**(9), 829–835.
- Cabello, José. 2021. Lithium brine production, reserves, resources and exploration in Chile: An updated review. *Ore Geology Reviews*, **128**, 103883.
- Cao, Tianzheng, Han, Dongmei, & Song, Xianfang. 2021. Past, present, and future of global seawater intrusion research: A bibliometric analysis. *Journal of Hydrology*, **603**, 126844.
- Chambers, Derrick, Jin, Ge, Tourei, Ahmad, Saeed Issah, Abdul Hafiz, Lellouch, Ariel, Martin, Eileen, Zhu, Donglin, Girard, Aaron, Yuan, Shihao, Cullison, Thomas, Snyder, Tomas, Kim, Seunghoo, Danes, Nicholas, Punithan, Nikhil, Boltz, M. Shawn, & Mendoza, Manuel M. 2024. DASCORE: a Python Library for Distributed Fiber Optic Sensing. *Seismica*, **3**(2).
- Cochran, J. F., Rudd, J. M., Muir, W. B., Trayling, G., & Heinrich, B. 1991. Temperature dependence of the Landau–Lifshitz damping parameter for iron. *Journal of Applied Physics*, **70**(10), 6545–6547.
- Cockett, Rowan, Kang, Seogi, Heagy, Lindsey J, Pidlisecky, Adam, & Oldenburg, Douglas W. 2015. SimPEG: An open source framework for simulation and gradient based parameter estimation in geophysical applications. *Computers & Geosciences*.
- Coey, J M D, Rhen, Fernando, Dunne, Peter, & McMurry, S. 2007. The magnetic concentration gradient force—Is it real? *Journal of Solid State Electrochemistry*, **11**(06), 711–717.

- COMSOL. 2023. Magnetostrictive Material. *COMSOL Documentation*.
- Costall, A. R., Harris, B. D., Teo, B., Schaa, R., Wagner, F. M., & Pigois, J. P. 2020. Groundwater Throughflow and Seawater Intrusion in High Quality Coastal Aquifers. *Scientific Reports*, **10**(1), 9866.
- Cullity, B.D., & Graham, C.D. 2009. *Introduction to Magnetic Materials*. 2 edn. John Wiley & Sons, Inc.
- Curcio, Ana, Chanampa, Eliana, Cabanillas, Luis, & Piethe, Ricardo. 2024. An effective multiphysics toolkit for lithium prospecting: From geophysics to the static reservoir model in the Pozuelos salt flat, Argentina. *Interpretation*, **12**(2), T105–T117.
- Dejneka, Zach, Homa, Daniel, Buontempo, Joshua, Crawford, Gideon, Martin, Eileen, Theis, Logan, Wang, Anbo, & Pickrell, Gary. 2024. Magnetic Field Sensing via Acoustic Sensing Fiber with Metglas® 2605SC Cladding Wires. *Photonics*, **11**(4).
- Djordjevic, Marija, Eilers, Gerrit, Parge, Anne, Münzenberg, Markus, & Moodera, J. S. 2006. Intrinsic and nonlocal Gilbert damping parameter in all optical pump-probe experiments. *Journal of Applied Physics*, **99**(8), 08F308.
- Donahue, Michael. 1999 (1999-09-01). *OOMMF User's Guide, Version 1.0*.
- Dormand, J.R., & Prince, P.J. 1980. A family of embedded Runge-Kutta formulae. *Journal of Computational and Applied Mathematics*, **6**(1), 19–26.
- Ez-zaouy, Yassine, Bouchaou, Lhoussaine, Schreiber, Henrik, Montcoudiol, Nelly, Kalberkamp, Ulrich, Danni, Saadou Oumarou, Touab, Amine, Abourrig, Fatima, & Hssaisoune, Mohammed. 2023. Combined geophysical methods to investigate seawater intrusion in the Souss-Massa coastal area, Morocco. *Groundwater for Sustainable Development*, **21**, 100915.
- Follett, Jon R. La, Yang, Zhaohui, Lopez, Jorge, Grandi, Samantha, & Hornman, Kees. 2016. *Maturing the buried cross-spread concept for land seismic monitoring: Borehole source tests*. SEG. Pages 5446–5450.
- Fornillo, Bruno, & Lampis, Andrea. 2023. From the Lithium Triangle to the Latin American quarry: The shifting geographies of de-fossilisation. *The Extractive Industries and Society*, **15**, 101326.
- Gilbert, Thomas L. 2004. A phenomenological theory of damping in ferromagnetic materials. *IEEE Transactions on Magnetics*, **40**, 3443–3449.
- Gutiérrez-Mejía, F., & Ruiz-Suárez, J.C. 2012. AC magnetic susceptibility at medium frequencies suggests a paramagnetic behavior of pure water. *Journal of Magnetism and Magnetic Materials*, **324**(6), 1129–1132.
- Hartog, A.H. 2018. *An Introduction to Distributed Optical Fibre Sensors*. Fiber Optic Sensors. CRC Press, Taylor & Francis group.
- Hasan, Muhammad, Shang, Yanjun, Jin, Weijun, Shao, Peng, Yi, Xuetao, & Akhter, Gulraiz. 2020. Geophysical Assessment of Seawater Intrusion into Coastal Aquifers of Bela Plain, Pakistan. *Water*, **12**(12).
- Hileman, Zachary, Homa, Daniel, Ma, Lingmei, Dong, Bo, Martin, Eileen, Pickrell, Gary, & Wang, Anbo. 2022. Development of a Multimaterial Optical Fiber for Fully Distributed Magnetic Sensing Applications. *IEEE Sensors Letters*, **6**(1), 1–4.

- Hussain, Mohammed S., Abd-Elhamid, Hany F., Javadi, Akbar A., & Sherif, Mohsen M. 2019. Management of Seawater Intrusion in Coastal Aquifers: A Review. *Water*, **11**(12).
- Ji, Meiyang, Ling, Hongying, Liu, Liang, Yang, Yuying, Chen, Ming, Yang, Deyu, & Liu, Hongyuan. 2023. Comparison of magnetic susceptibility probes relevantly used in soil contamination applications. *Environmental Monitoring and Assessment*, **195**(6), 677.
- Kanu, M. O. 2014. Comparative study of top soil magnetic susceptibility variation based on some human activities. *Geofísica Internacional*, **53**(4), 411–423.
- Karl, Nick A, Mauk, Jeffrey L, Reyes, Tyler A, & Scott, Patrick C. 2019. *Lithium deposits in the United States*.
- Kaufman, Alexander A., Hansen, R. O., & Kleinberg, Robert L. K. 2009. *Principles of the magnetic methods in geophysics*. Methods in geochemistry and geophysics ; 42. Amsterdam ;: Elsevier. Includes bibliographical references and index.
- Kirsch, R. 2006. *Groundwater Geophysics: A Tool for Hydrogeology*. Springer Berlin Heidelberg.
- Kodama, Kazuto. 2010. A new system for measuring alternating current magnetic susceptibility of natural materials over a wide range of frequencies. *Geochemistry, Geophysics, Geosystems*, **11**(11).
- Kondev, F.G., Wang, M., Huang, W.J., Naimi, S., & Audi, G. 2021. The NUBASE2020 evaluation of nuclear physics properties *. *Chinese Physics C*, **45**(3), 030001.
- Krechowicz, Maria. 2020. Comprehensive Risk Management in Horizontal Directional Drilling Projects. *Journal of Construction Engineering and Management*, **146**(5), 04020034.
- Kruglov, O., & Menshov, O. 2017. To the soil magnetic susceptibility application in modern soil science. *16th International Conference on Geoinformatics - Theoretical and Applied Aspects*, **2017**(1), 1–6.
- Kruglov, O., Menshov, O., Horoshkova, L., Tonkha, O., Andreeva, O., Kruhlov, B., & Zhuravel, O. 2022. Soil Sampling and Magnetic Susceptibility Determination in Soil Science: Methodological Aspect. *16th International Conference Monitoring of Geological Processes and Ecological Condition of the Environment*, **2022**(1), 1–5.
- Kumar, Prashant, Biswas, Arkoprovo, Banerjee, Sayandeep, Rathore, Sanny, Rana, Virendra, Ram, Kirpa, & Acharya, Tapas. 2022. Integrating magnetic susceptibility, hydrogeochemical, and isotopic data to assess the seawater invasion in coastal aquifers of Digha, West Bengal, India. *Environmental Science and Pollution Research*, **29**(16), 23474–23503.
- Lakshmanan, M. 2011. The fascinating world of the Landau–Lifshitz–Gilbert equation: an overview. *Philosophical Transactions of the Royal Society A: Mathematical, Physical and Engineering Sciences*, **369**(1939), 1280–1300.
- Lam, Elizabeth J., Carle, Rodrigo, González, Rodrigo, Montofré, Ítalo L., Veloso, Eugenio A., Bernardo, Antonio, Cánovas, Manuel, & Álvarez, Fernando A. 2020. A Methodology Based on Magnetic Susceptibility to Characterize Copper Mine Tailings. *Minerals*, **10**(11).
- Liang, Cheng-Yen, Keller, Scott M, Sepulveda, Abdon E, Bur, Alexandre, Sun, Wei-Yang, Wetzlar, Kyle, & Carman, Gregory P. 2014. Modeling of magnetoelastic nanostructures with a fully coupled mechanical-micromagnetic model. *Nanotechnology*, **25**(43), 435701.

- Lima, Victor Hugo Sarrazin, Moura, João Paulo, Pissarra, Teresa Cristina Tarlé, do Valle Junior, Renato Farias, de Melo Silva, Maytê Maria Abreu Pires, Valera, Carlos Alberto, De Melo, Marília Carvalho, Fernandes, Luís Filipe Sanches, Da Costa, Adriana Monteiro, & Pacheco, Fernando António Leal. 2024. Groundwater flow and transport of metals under deposits of mine tailings: A case study in Brumadinho, Minas Gerais, Brazil. *Case Studies in Chemical and Environmental Engineering*, **9**, 100690.
- Magiera, Tadeusz, Zawadzki, Jarosław, Szuszkiewicz, Marcin, Fabijańczyk, Piotr, Steinnes, Eiliv, Fabian, Karl, & Miszczak, Ewa. 2018. Impact of an iron mine and a nickel smelter at the Norwegian/Russian border close to the Barents Sea on surface soil magnetic susceptibility and content of potentially toxic elements. *Chemosphere*, **195**, 48–62.
- Maisel, Franziska, Neef, Christoph, Marscheider-Weidemann, Frank, & Nissen, Nils F. 2023. A forecast on future raw material demand and recycling potential of lithium-ion batteries in electric vehicles. *Resources, Conservation and Recycling*, **192**, 106920.
- Mankovsky, Sergiy, Koedderitzsch, D., Woltersdorf, Georg, & Ebert, H. 2013. First-principles calculation of the Gilbert damping parameter via the linear response formalism with application to magnetic transition-metals and alloys. *Physical Review B*, **87**(01).
- Martin, Eileen R., Lindsey, Nathaniel J., Ajo-Franklin, Jonathan B., & Biondi, Biondo L. 2021. *Introduction to Interferometry of Fiber-Optic Strain Measurements*. American Geophysical Union (AGU). Chap. 9, pages 111–129.
- Mohammadzadeh Bina, Saeid, Fujii, Hikari, Tsuya, Shunsuke, Kosukegawa, Hiroyuki, Naganawa, Shigemi, & Harada, Retsu. 2020. Evaluation of utilizing horizontal directional drilling technology for ground source heat pumps. *Geothermics*, **85**, 101769.
- Morales, Juan, Hernández-Bernal, Maria del Sol, Corona-Chavez, Pedro, Gogichaishvili, Avto, & Bautista, Francisco. 2016. Further evidence for magnetic susceptibility as a proxy for the evaluation of heavy metals in mining wastes: case study of Tlalpujahua and El Oro Mining Districts. *Environmental Earth Sciences*, **75**(02).
- Moreira, Cesar Augusto, Casagrande, Matheus Felipe Stanfoca, de Siqueira Büchi, Fernanda Miranda, & Targa, Débora Andrade. 2020. Hydrogeological characterization of a waste rock pile and bedrock affected by acid mine drainage from geophysical survey. *SN Applied Sciences*, **2**(7), 1236.
- Nabighian, M. N., Grauch, V. J. S., Hansen, R. O., LaFehr, T. R., Li, Y., Peirce, J. W., Phillips, J. D., & Ruder, M. E. 2005. The historical development of the magnetic method in exploration. *GEOPHYSICS*, **70**(6), 33ND–61ND.
- Orlyuk, M., Kurnikov, Yu., Drukarenko, V., & Yakuhno, V. 2022. Experimental Study of Magnetic Parameters of the Magnetized Water. *16th International Conference Monitoring of Geological Processes and Ecological Condition of the Environment*, **2022**(1), 1–5.
- Oudeika, Mohamed Salem, Altinoglu, Fatma Figen, Akbay, Fatih, & Aydin, Ali. 2020. The use of magnetic susceptibility and chemical analysis data for characterizing heavy metal contamination of topsoil in Denizli city, Turkey. *Journal of Applied Geophysics*, **183**, 104208.
- Paterson, Norman R., & Reeves, Colin V. 1985. Applications of gravity and magnetic surveys: The state-of-the-art in 1985. *GEOPHYSICS*, **50**(12), 2558–2594.

- Petrovský, E., Kapička, A., Jordanova, N., Knab, M., & Hoffmann, V. 2000. Low-field magnetic susceptibility: a proxy method of estimating increased pollution of different environmental systems. *Environmental Geology*, **39**(3), 312–318.
- Power, Christopher, & Almpanis, Angelos. 2022. Improved imaging efficiency of large mine waste rock piles with integrated electrical and electromagnetic geophysical techniques. *Journal of Applied Geophysics*, **206**, 104824.
- Rakshith, Shetty, Samaniuk, Joseph, & Mooney, Michael. 2023. Development of annular pump to enhance drilling distance and cuttings return in horizontal directional drilling. *Tunnelling and Underground Space Technology*, **140**(10), 105324.
- Rana, Virendra, Kumar, Prashant, Banerjee, Sayandeep, & Biswas, Arkoprovo. 2021. Magnetic susceptibility investigation of the saline water intrusion problem: The LAMP-BHU protocol. *Journal of Earth System Science*, **130**(3), 140.
- Razowska, L. 2001. Changes of groundwater chemistry caused by the flooding of iron mines (Czestochowa Region, Southern Poland). *Journal of Hydrology*, **244**(1), 17–32.
- Schmidt, Armin, Yarnold, Richard, Hill, Matt, & Ashmore, Mike. 2005. Magnetic susceptibility as proxy for heavy metal pollution: a site study. *Journal of Geochemical Exploration*, **85**(3), 109–117.
- Scholz, Werner, Fidler, Josef, Schrefl, Thomas, Suess, Dieter, Dittrich, Rok, Forster, Hermann, & Tsiantos, Vassilios. 2003. Scalable parallel micromagnetic solvers for magnetic nanostructures. *Computational Materials Science*, **28**(2), 366–383. Proceedings of the Symposium on Software Development for Process and Materials Design.
- Shang, Ying, Sun, Maocheng, Wang, Chen, Yang, Jian, Du, Yuankai, Yi, Jichao, Zhao, Wenan, Wang, Yingying, Zhao, Yanjie, & Ni, Jiasheng. 2022. Research Progress in Distributed Acoustic Sensing Techniques. *Sensors*, **22**(08), 6060.
- Shirzaditabar, Farzad, & Heck, Richard J. 2021. Characterization of soil magnetic susceptibility: a review of fundamental concepts, instrumentation, and applications. *Canadian Journal of Soil Science*, **102**(2), 231 – 251.
- Shoemaker, Katherine. 2018. *The Mathematical Modeling of Magnetostriction*. Master's Thesis, Bowling Green State University, Bowling Green, OH.
- Skousen, Jeff, & Jacobs, James. 2014. *Acid Mine Drainage, Rock Drainage, and Acid Sulfate Soils: Causes, Assessment, Prediction, Prevention, and Remediation*. John Wiley and Sons, Inc. Pages 105–118.
- Smith, Ryan K., Grabowski, Marek, & Camley, R.E. 2010. Period doubling toward chaos in a driven magnetic macrospin. *Journal of Magnetism and Magnetic Materials*, **322**(15), 2127–2134.
- Tabelin, Carlito Baltazar, Dallas, Jessica, Casanova, Sophia, Pelech, Timothy, Bournival, Ghislain, Saydam, Serkan, & Canbulat, Ismet. 2021. Towards a low-carbon society: A review of lithium resource availability, challenges and innovations in mining, extraction and recycling, and future perspectives. *Minerals Engineering*, **163**, 106743.
- Tarallo, D., Alberico, I., Cavuoto, G., Pelosi, N., Punzo, M., & Di Fiore, V. 2023. Geophysical assessment of seawater intrusion: the Volturmo Coastal Plain case study. *Applied Water Science*, **13**(12), 234.
- Taylor, John R. 2005. *Classical Mechanics*. University Science Books.

- The MathWorks, Inc. 2022. *MATLAB version: 9.13.0 (R2022b)*.
<https://www.mathworks.com/products/matlab>. R2022b.
- Thompson, Roy, & Oldfield, Frank. 1986. *Magnetic properties of natural materials*. Dordrecht: Springer Netherlands. Pages 21–38.
- Tomiyama, Shingo, & Igarashi, Toshifumi. 2022. The potential threat of mine drainage to groundwater resources. *Current Opinion in Environmental Science and Health*, **27**, 100347.
- Topping, C V, & Blundell, S J. 2018. A.C. susceptibility as a probe of low-frequency magnetic dynamics. *Journal of Physics: Condensed Matter*, **31**(1), 013001.
- Ukil, Abhisek, Braendle, Hubert, & Krippner, Peter. 2012. Distributed Temperature Sensing: Review of Technology and Applications. *IEEE Sensors Journal - IEEE SENS J*, **12**(05), 885–892.
- Van Rossum, Guido, & Drake, Fred L. 2009. *Python 3 Reference Manual*. Scotts Valley, CA: CreateSpace.
- Wang, Fei, Li, Wei, Wang, Hao, Hu, Yuanan, & Cheng, Hefa. 2024. The leaching behavior of heavy metal from contaminated mining soil: The effect of rainfall conditions and the impact on surrounding agricultural lands. *Science of The Total Environment*, **914**, 169877.
- Wieser, Robert. 2015. Description of a dissipative quantum spin dynamics with a Landau-Lifshitz/Gilbert like damping and complete derivation of the classical Landau-Lifshitz equation. *The European Physical Journal B*, **88**(77).
- Yan, Xufeng, Ariaratnam, Samuel T., Dong, Shun, & Zeng, Cong. 2018. Horizontal directional drilling: State-of-the-art review of theory and applications. *Tunnelling and Underground Space Technology*, **72**, 162–173.

APPENDIX A
MODELING CODE

The code used to run the application simulations, two-dimensional model, and three-dimensional model are listed here. They are also accessible on my Github at:

<https://github.com/quasiStellar45/Magnetostriction> (DOI: 10.5281/zenodo.14194765)

Listing A.1: The seawater intrusion simulation code.

```
"""
Seawater intrusion model
=====

The seawater intrusion model is run with this script.
It can be set to be a simple model with a single boundary
or a realistic (complex) model with a gradient, dipping
boundary.
"""

#####
# Import Modules
# -----
#

import numpy as np
from scipy.interpolate import LinearNDInterpolator
import matplotlib as mpl
import matplotlib.pyplot as plt
import os
import sys

sys.path.append(r'C:\Users\Tomas\simpeg')
from discretize import TensorMesh
from discretize.utils import mkvc, active_from_xyz
from SimPEG.utils import plot2Ddata
from SimPEG import maps
from SimPEG.potential_fields import magnetics

#####
# User Input
# -----
#
# Define code directions and certain variables here.
# For further edits, you may need to edit the code below this section.
#
write_output = True # True to output the forward model results
output_location = 'test' # output folder within 'outputs'
gradient = True # True if you want a gradient boundary
simple = True # True for simple model, False for complex
boundary = -5 # define the boundary for the simple model, this is not
               used in the complex model
suffix = '75m' # output file suffix
```

```

depth = 75                # define the sensor depth

#####
# Topography
# -----
#
# Surface topography is defined as an (N, 3) numpy array. We create it here but
# topography could also be loaded from a file.
#

[x_topo, y_topo] = np.meshgrid(np.linspace(-50, 50, 100), np.linspace(-50, 50, 100))
z_topo = np.sqrt((x_topo)**2+(y_topo)**2)
x_topo, y_topo, z_topo = mkvc(x_topo), mkvc(y_topo), mkvc(z_topo)
xyz_topo = np.c_[x_topo, y_topo, z_topo]

#####
# Defining the Survey
# -----
#
# Here, we define survey that will be used for the simulation. Magnetic
# surveys are simple to create. The user only needs an (N, 3) array to define
# the xyz locations of the observation locations, the list of field components
# which are to be modeled and the properties of the Earth's field.
#

# Define the observation locations as an (N, 3) numpy array or load them.
xr = np.linspace(-50, 50, 50)
yr = np.linspace(-50, 50, 3)
x, y = np.meshgrid(xr, yr)
x, y = mkvc(x.T), mkvc(y.T)
fun_interp = LinearNDInterpolator(np.c_[x_topo, y_topo], z_topo)
z = - depth*np.ones(len(y)) # Sensor location in m below surface.
receiver_locations = np.c_[x, y, z]

# Define the component(s) of the field we want to simulate as a list of strings.
# Here we simulation total magnetic intensity data.
components = ["tmi"]

# Use the observation locations and components to define the receivers. To
# simulate data, the receivers must be defined as a list.
receiver_list = magnetics.receivers.Point(receiver_locations, components=components)

receiver_list = [receiver_list]

# Define the inducing field H0 = (intensity [nT], inclination [deg], declination [
deg])
inclination = 0
declination = 90
strength = 560000

source_field = magnetics.sources.UniformBackgroundField(
    receiver_list=receiver_list,
    amplitude=strength,
    inclination=inclination,
    declination=declination,
)

# Define the survey
survey = magnetics.survey.Survey(source_field)

```

```

#####
# Defining a Tensor Mesh
# -----
#
# Here, we create the tensor mesh that will be used for the forward simulation.
#

dh = 2
hx = [(dh, 50)]
hy = [(dh, 50)]
hz = [(dh, 50)]
mesh = TensorMesh([hx, hy, hz], "CCN")

#####
# Defining a Susceptibility Model
# -----
#
# Here, we create the model that will be used to predict magnetic data
# and the mapping from the model to the mesh. The model
# consists of a susceptible sphere in a less susceptible host.
#

# Define susceptibility values for each unit in SI
background_susceptibility = 1e-5
fresh_susceptibility = -3e-5
saline_susceptibility = -6.5e-5
mixed_susceptibility1 = -5e-5
mixed_susceptibility2 = -4e-5

# Find cells that are active in the forward modeling (cells below surface)
ind_active = active_from_xyz(mesh, xyz_topo)

# Define the model
model = background_susceptibility * np.ones(ind_active.sum())

# Define mapping from model to active cells
nC = int(ind_active.sum())
model_map = maps.IdentityMap(nP=nC) # model is a vlue for each active cell

# Define model blocks
ii = 0
if simple:
    xr = [boundary]
for e in xr: # for simple boundary with gradient, replace xr with [boundary]
    including the brackets

    ind_saline = (
        (mesh.gridCC[ind_active, 0] >= min(x))
        & (mesh.gridCC[ind_active, 0] <= e)
        & (mesh.gridCC[ind_active, 2] < -5 + ii)
    )
    if gradient:
        ind_mix1 = (
            (mesh.gridCC[ind_active, 0] > e)
            & (mesh.gridCC[ind_active, 0] <= e+10)
            & (mesh.gridCC[ind_active, 2] < -5 + ii)
        )

```

```

    )

    ind_mix2 = (
        (mesh.gridCC[ind_active, 0] > e+10)
        & (mesh.gridCC[ind_active, 0] <= e+30)
        & (mesh.gridCC[ind_active, 2] < -5 + ii)
    )

    ind_fresh = (
        (mesh.gridCC[ind_active, 0] > e+30)
        & (mesh.gridCC[ind_active, 0] <= max(x))
        & (mesh.gridCC[ind_active, 2] < -5 + ii)
    )

    model[ind_mix1] = mixed_susceptibility1
    model[ind_mix2] = mixed_susceptibility2
else:
    ind_fresh = (
        (mesh.gridCC[ind_active, 0] > e)
        & (mesh.gridCC[ind_active, 0] <= max(x))
        & (mesh.gridCC[ind_active, 2] < -5 + ii)
    )

    model[ind_saline] = saline_susceptibility
    model[ind_fresh] = fresh_susceptibility
    ii += -2

# Plot Model
fig = plt.figure(figsize=(9, 4))

plotting_map = maps.InjectActiveCells(mesh, ind_active, np.nan)
ax1 = fig.add_axes([0.1, 0.12, 0.73, 0.78])
mesh.plot_slice(
    plotting_map * model,
    normal="Y",
    ax=ax1,
    ind=int(mesh.shape_cells[1] / 2),
    grid=True,
    clim=(np.min(model), np.max(model)),
)
ax1.set_title("Model_slice_at_y=-0.0m")
ax1.set_xlabel("x(m)")
ax1.set_ylabel("z(m)")

ax2 = fig.add_axes([0.85, 0.12, 0.05, 0.78])
norm = mpl.colors.Normalize(vmin=np.min(model), vmax=np.max(model))
cbar = mpl.colorbar.ColorbarBase(ax2, norm=norm, orientation="vertical")
cbar.set_label("Magnetic_Susceptibility_(SI)", rotation=270, labelpad=15, size=12)

plt.show()

#####
# Simulation: TMI Data for a Susceptibility Model
# -----
#
# Here we demonstrate how to predict magnetic data for a magnetic
# susceptibility model using the integral formulation.

```

```

#

# Define the forward simulation. By setting the 'store_sensitivities' keyword
# argument to "forward_only", we simulate the data without storing the sensitivities
simulation = magnetics.simulation.Simulation3DIntegral(
    survey=survey,
    mesh=mesh,
    model_type="scalar",
    chiMap=model_map,
    ind_active=ind_active,
    store_sensitivities="forward_only"
)

# Compute predicted data for a susceptibility model
dpred = simulation.dpred(model)

# Plot
fig = plt.figure(figsize=(6, 5))
v_max = np.max(np.abs(dpred))

ax1 = fig.add_axes([0.1, 0.1, 0.8, 0.85])
plot2Ddata(
    receiver_list[0].locations,
    dpred,
    ax=ax1,
    ncontour=30,
    clim=(-v_max, v_max),
    contourOpts={"cmap": "bwr"},
)

p1 = ax1.plot(x,y, '.', label='sensors')
ax1.set_title("TML Anomaly")
ax1.set_xlabel("x (m)")
ax1.set_ylabel("y (m)")
ax1.legend(handles= p1)

ax2 = fig.add_axes([0.87, 0.1, 0.03, 0.85])
norm = mpl.colors.Normalize(vmin=-np.max(np.abs(dpred)), vmax=np.max(np.abs(dpred)))
cbar = mpl.colorbar.ColorbarBase(
    ax2, norm=norm, orientation="vertical", cmap=mpl.cm.bwr
)
cbar.set_label("$nT$", rotation=270, labelpad=15, size=12)

plt.show()
#####
# Optional: Export Data
# -----
#
# Write the data and topography
#

if write_output:
    dir_path = os.path.dirname(__file__).split(os.path.sep)
    dir_path.extend(["outputs"])
    dir_path.extend([output_location])
    dir_path = os.path.sep.join(dir_path) + os.path.sep

    if not os.path.exists(dir_path):
        os.mkdir(dir_path)

```

```
fname = dir_path + "magnetics_topo_" + suffix + ".txt"
np.savetxt(fname, np.c_[xyz_topo], fmt="%.4e")

np.random.seed(211)
maximum_anomaly = np.max(np.abs(dpred))
noise = 0.02 * maximum_anomaly * np.random.randn(len(dpred))
fname = dir_path + "magnetics_data_" + suffix + ".obs"
np.savetxt(fname, np.c_[receiver_locations, dpred + noise], fmt="%.4e")
```

Listing A.2: The mine drainage and lithium brine simulation code.

```

"""
Mine drainage/Lithium model
=====

This model can be used to simulate lithium and mine
drainage scenarios. The output is a TMI anomaly plot.
"""

#####
# Import Modules
# -----
#

import numpy as np
from scipy.interpolate import LinearNDInterpolator
import matplotlib as mpl
import matplotlib.pyplot as plt
import os
import sys

sys.path.append(r'C:\Users\Tomas\simpeg')
from discretize import TensorMesh
from discretize.utils import mkvc, active_from_xyz
from SimPEG.utils import plot2Ddata
from SimPEG import maps
from SimPEG.potential_fields import magnetics

#####
# User Input
# -----
#
# Define code directions and certain variables here.
# For further edits, you may need to edit the code below this section.
#
write_output = False      # True to output the forward model results
output_location = 'test'  # output folder within 'outputs'
gradient = False          # True if you want a gradient boundary
simple = True              # True for simple model, False for complex
boundary = 0              # define the boundary for the simple model, this is not
                          # used in the complex model
suffix = '1500m'         # output file suffix
depth = 10                # define the sensor depth
metal_concentration = 1500 # mg/L
amu = 6.9410              # g/mol (Li), Fe: 55.845
p2 = 15 # Li, Fe:24

#####
# Topography
# -----
#
# Surface topography is defined as an (N, 3) numpy array. We create it here but
# topography could also be loaded from a file.
#

[x_topo, y_topo] = np.meshgrid(np.linspace(-50, 50, 100), np.linspace(-50, 50, 100))
z_topo = np.sqrt((x_topo)**2+(y_topo)**2)

```

```

x_topo, y_topo, z_topo = mkvc(x_topo), mkvc(y_topo), mkvc(z_topo)
xyz_topo = np.c_[x_topo, y_topo, z_topo]

#####
# Defining the Survey
# -----
#
# Here, we define survey that will be used for the simulation. Magnetic
# surveys are simple to create. The user only needs an (N, 3) array to define
# the xyz locations of the observation locations, the list of field components
# which are to be modeled and the properties of the Earth's field.
#

# Define the observation locations as an (N, 3) numpy array or load them.
xr = np.linspace(-50, 50, 50)
yr = np.linspace(-50, 50, 3)
x, y = np.meshgrid(xr, yr)
x, y = mkvc(x.T), mkvc(y.T)
fun_interp = LinearNDInterpolator(np.c_[x_topo, y_topo], z_topo)
z = - depth*np.ones(len(y)) # Sensor location in m below surface.
receiver_locations = np.c_[x, y, z]

# Define the component(s) of the field we want to simulate as a list of strings.
# Here we simulation total magnetic intensity data.
components = ["tmi"]

# Use the observation locations and components to define the receivers. To
# simulate data, the receivers must be defined as a list.
receiver_list = magnetics.receivers.Point(receiver_locations, components=components)

receiver_list = [receiver_list]

# Define the inducing field H0 = (intensity [nT], inclination [deg], declination [
    deg])
inclination = 0
declination = 90
strength = 560000

source_field = magnetics.sources.UniformBackgroundField(
    receiver_list=receiver_list,
    amplitude=strength,
    inclination=inclination,
    declination=declination,
)

# Define the survey
survey = magnetics.survey.Survey(source_field)

#####
# Defining a Tensor Mesh
# -----
#
# Here, we create the tensor mesh that will be used for the forward simulation.
#

dh = 2
hx = [(dh, 50)]
hy = [(dh, 50)]

```

```

hz = [(dh, 50)]
mesh = TensorMesh([hx, hy, hz], "CCN")

#####
# Defining a Susceptibility Model
# -----
#
# Here, we create the model that will be used to predict magnetic data
# and the mapping from the model to the mesh. The model
# consists of a susceptible sphere in a less susceptible host.
#

# Define susceptibility values for each unit in SI
background_susceptibility = 1e-5
fresh_susceptibility = -1.65e-5 #-9e-6
concentration = metal_concentration/(amu*1000) # Moles/L
c = concentration*1000 # moles/m^3
cmol = 1.571e-6*p2
tt = 295 # temperature in K
iron_susceptibility = -1.575e-5 #fresh_susceptibility + c*cmol/tt
mixed_susceptibility1 = -1.625e-5
mixed_susceptibility2 = -1.6e-5

# Find cells that are active in the forward modeling (cells below surface)
ind_active = active_from_xyz(mesh, xyz_topo)

# Define the model
model = background_susceptibility * np.ones(ind_active.sum())

# Define mapping from model to active cells
nC = int(ind_active.sum())
model_map = maps.IdentityMap(nP=nC) # model is a value for each active cell

# Define model blocks
ii = 0
if simple:
    xr = [boundary]
for e in xr: # for simple boundary with gradient, replace xr with [boundary]
    including the brackets

    ind_fresh = (
        (mesh.gridCC[ind_active, 0] >= min(x))
        & (mesh.gridCC[ind_active, 0] <= e)
        & (mesh.gridCC[ind_active, 2] < -5 + ii)
    )
    if gradient:
        ind_mix1 = (
            (mesh.gridCC[ind_active, 0] > e)
            & (mesh.gridCC[ind_active, 0] <= e+10)
            & (mesh.gridCC[ind_active, 2] < ii)
        )

        ind_mix2 = (
            (mesh.gridCC[ind_active, 0] > e+10)
            & (mesh.gridCC[ind_active, 0] <= e+30)
            & (mesh.gridCC[ind_active, 2] < ii)
        )

```

```

    ind_iron= (
        (mesh.gridCC[ind_active, 0] > e+30)
        & (mesh.gridCC[ind_active, 0] <= max(x))
        & (mesh.gridCC[ind_active, 2] < ii)
    )

    model[ind_mix1] = mixed_susceptibility1
    model[ind_mix2] = mixed_susceptibility2
else:
    ind_iron = (
        (mesh.gridCC[ind_active, 0] > e)
        & (mesh.gridCC[ind_active, 0] <= max(x))
        & (mesh.gridCC[ind_active, 2] < -5 + ii)
    )

    model[ind_iron] = iron_susceptibility
    model[ind_fresh] = fresh_susceptibility
    ii += -2

# Plot Model
fig = plt.figure(figsize=(9, 4))

plotting_map = maps.InjectActiveCells(mesh, ind_active, np.nan)
ax1 = fig.add_axes([0.1, 0.12, 0.73, 0.78])
mesh.plot_slice(
    plotting_map * model,
    normal="Y",
    ax=ax1,
    ind=int(mesh.shape_cells[1] / 2),
    grid=True,
    clim=(np.min(model), np.max(model))
)
ax1.set_title("Model_slice_at_y=-0.0m")
ax1.set_xlabel("x(m)")
ax1.set_ylabel("z(m)")

ax2 = fig.add_axes([0.85, 0.12, 0.05, 0.78])
norm = mpl.colors.Normalize(vmin=np.min(model), vmax=np.max(model))
cbar = mpl.colorbar.ColorbarBase(ax2, norm=norm, orientation="vertical")
cbar.set_label("Magnetic_Susceptibility_(SI)", rotation=270, labelpad=15, size=12)

plt.show()

#####
# Simulation: TMI Data for a Susceptibility Model
# -----
#
# Here we demonstrate how to predict magnetic data for a magnetic
# susceptibility model using the integral formulation.
#
# Define the forward simulation. By setting the 'store_sensitivities' keyword
# argument to "forward_only", we simulate the data without storing the sensitivities
simulation = magnetics.simulation.Simulation3DIntegral(
    survey=survey,
    mesh=mesh,

```

```

        model_type="scalar",
        chiMap=model_map,
        ind_active=ind_active,
        store_sensitivities="forward_only"
    )

# Compute predicted data for a susceptibility model
dpred = simulation.dpred(model)

# Plot
fig = plt.figure(figsize=(6, 5))
v_max = np.max(np.abs(dpred))

ax1 = fig.add_axes([0.1, 0.1, 0.8, 0.85])
plot2Ddata(
    receiver_list[0].locations,
    dpred,
    ax=ax1,
    ncontour=30,
    clim=(-v_max, v_max),
    contourOpts={"cmap": "bwr"},
)

p1 = ax1.plot(x,y, '.', label='sensors')
ax1.set_title("TMI Anomaly")
ax1.set_xlabel("x_(m)")
ax1.set_ylabel("y_(m)")
ax1.legend(handles= p1)

ax2 = fig.add_axes([0.87, 0.1, 0.03, 0.85])
norm = mpl.colors.Normalize(vmin=-np.max(np.abs(dpred)), vmax=np.max(np.abs(dpred)))
cbar = mpl.colorbar.ColorbarBase(
    ax2, norm=norm, orientation="vertical", cmap=mpl.cm.bwr
)
cbar.set_label("$nT$", rotation=270, labelpad=15, size=12)

plt.show()
#####
# Optional: Export Data
# -----
#
# Write the data and topography
#

if write_output:
    dir_path = os.path.dirname(__file__).split(os.path.sep)
    dir_path.extend(["outputs"])
    dir_path.extend([output_location])
    dir_path = os.path.sep.join(dir_path) + os.path.sep

    if not os.path.exists(dir_path):
        os.mkdir(dir_path)

    fname = dir_path + "magnetics_topo_" + suffix + ".txt"
    np.savetxt(fname, np.c_[xyz_topo], fmt="%.4e")

    np.random.seed(211)
    maximum_anomaly = np.max(np.abs(dpred))
    noise = 0.02 * maximum_anomaly * np.random.randn(len(dpred))

```

```
fname = dir_path + "magnetics_data_" + suffix + ".obs"  
np.savetxt(fname, np.c_[receiver_locations, dpred + noise], fmt="%.4e")
```

Listing A.3: The contour plotting code for the simulation codes.

```

'''
TMI anomaly contour plotting script
'''



---




---



This script is used to plot contours along y = 0m.
All output files desired should be placed in the
same folder. The ending of a file should be a number
followed by 'm'. For example, magnetics_data_30m.obs
'''

import os
import numpy as np
import matplotlib.pyplot as plt
import sys
import re

sys.path.append(r'C:\Users\Tomas\simpeg')
# input plot title here
plot_title = r'Li$^{+}$ concentration (mg/L)'

def break_string_at_underscore_and_dot(s):
    # Use regex to split the string at both _ and .
    return re.split(r'[_\.](m)', s)

def convert_to_float(s):
    num = float(s)
    if num.is_integer():
        return int(num)
    else:
        return num

# files to work with
dir_path = os.getcwd() + '\\outputs\\lithium_concentration\\'
file_list = os.listdir(dir_path)
# retrieve all file suffixes
suffix = []
for file in file_list:
    s = break_string_at_underscore_and_dot(file)
    suffix.append(s[3])
# retrieve unique values in suffix list and order them in ascending order
suffix = list(set(suffix))
float_list = [convert_to_float(s.replace('_',',','.')) for s in suffix]
float_list = sorted(float_list)
suffix = [str(f) for f in float_list]
# plot all results
fig = plt.figure(figsize=(10, 8))
plt.ylabel('TMI anomaly value (nT)', size=20)
plt.xlabel('x (m)', size=20)
plt.xticks(fontsize=20)
plt.yticks(fontsize=20)
plt.title("Model profile comparison at y = 0 m", size=20)
plt.grid()
for e in suffix:
    e = e.replace('_',',','.')
    topo_filename = dir_path + "magnetics_topo-" + e + ".m.txt"

```

```

data_filename = dir_path + "magnetics_data_" + e + "m.obs"

topo_xyz = np.loadtxt(str(topo_filename))
dobs = np.loadtxt(str(data_filename))

receiver_locations = dobs[:, 0:3]
dobs = dobs[:, -1]

x = receiver_locations[:,0]
y = receiver_locations[:,1]
ydata = []
for ii in range(0, len(y)):
    if y[ii] == 0:
        ydata.append((x[ii], dobs[ii]))
xvals = [x for x, y in ydata]
cdata = [y for x, y in ydata]

e = e.replace('_', '.', '.')
plt.plot(xvals[1:-1], cdata[1:-1], marker='.', linestyle='-', label=e)

plt.legend(title=plot_title)
plt.show()

```

Listing A.4: Two-dimensional magnetostriction model code in MATLAB.

```

%% Model of Isotropic, 2D, Single Domain Magnetostrictive Response
% The assumptions are that the material is homogeneous and isotropic,
% there are 2 dimensions, there is one domain, the magnetic field is
% uniform in space, the strain measurement direction is in the same
% direction as the magnetic field, and the magnetic moment torque response
% is instantaneous. The source is sinusoidal with changeable phase and
% frequency. The damping parameter is unknown and can be altered to
% examine changes in the response.
clear;
close all

%% Which Plots to Generate - enter true or false (1 or 0)
dynamics_plots = 0; % theta dynamics plots
strain_plot = 0; % strain plot
FFT_plot = 1; % FFT plot
run_large = 0; % large scale animation
run_small = 0; % small scale animation
% - both animations cannot run at the same time
% - make sure to check parameters in animations
% section before running

%% Adjustable Parameters
% Material Properties
Ms = 4.908e2; % kA/m, Saturation magnetization of Ni at 298K
L0 = -34; % ppm, saturation magnetostriction of Ni
lambda = 1.2e4; % adjustable damping parameter

% Source Properties, H = H0sin(omega*t-phi)+H_bias or
% H0square(omega*t)+Hbias
HSource = 1; % set to 1 for a sin source, 0 for a square wave. To
% run the square wave you will need MATLAB's signal
% processing package.
f = 100; % Hz, source frequency: omega = 2pi*f
H0 = 1.3; % kA/m, source amplitude
phi = 0; % radians, source phase; if set to -pi/2, the source becomes
% cosine.
H_bias = 0; % Add a bias to the source signal. If =0, no bias is included

% Initial Conditions and FFT Parameters
theta0 = 5*pi/6; % radians, initial theta position
t_0 = 0; % s, time where theta and strain plots begin
t_f = 10; % s, final time
fs = 1e5; % Hz, FFT sampling frequency
sety = 30; % yaxis upper limit of the FFT

%% Animations - check these parameters before running the animations
% Large Scale Animation - displays all motion of the magnetic moment
step_large = 10; % iteration step of animation
Hfactor_large = 5; % factor to increase the magnetic field vector by.
% This value should be H_factor*H0 <= Ms.
t_frac_large = 50; % What fraction of the total time do you want to run?

% Small Scale Animation - displays small scale motion of magnetic moment
% when H is in the theta = 0 direction. Run the large scale animation first
% to see if there are small oscillations. If there are, run this animation
% to increase the size of those small scale oscillations.
step_small = 1; % iteration step of animation

```

```

Hfactor_small = 5;      % factor to increase the magnetic field vector by
t_frac_small = 200;    % What fraction of the total time do you want to run?
theta_limit_0 = 5e-10; % upper limit of thetas of interest when the magnetic
                        % field is pointing in the direction of theta = 0.
                        % Note that this may need to be on the order of
                        % 10^-10 for high H0 (>10 kA/m).
theta_factor_0 = 1e5;  % factor to increase theta by when the magnetic
                        % field is pointing in the theta = 0 direction.
                        % Note that this may need to be on the order of 10^5
                        % for high H0 and low theta_limit_0.

%% Constants and some Calculations
g = 2; % spectroscopic splitting factor for e- spin
e = 1.6e-19; % C, e- charge
c = 3e8; % m/s, speed of light
me = 9.1e-31; % kg, e- mass
k = pi*4e-7; % H/m

gamma = g*e/(2*me*c); % constant related to angular momentum
alpha = lambda/(gamma*Ms); % damping constant
omega = 2*pi*f; % Radians/s source frequency

%% ODE Solver (5th order Runge-Kutta Method)
n=1;
%for n=1:length(f)
tspan = 0:1/fs:t_f-1/fs; % s, time span of interest
if HSource == 1
H = H0*sin(omega*tspan-phi)+H_bias; % magnetic field signal
else
H = H0*sqrt(omega*tspan);
end

[t(:,1),theta(:,1)] = ...
ode45(@(t,theta) LLG_2D(t,theta,gamma,alpha,H0,omega,phi,HSource,H_bias),tspan,
theta0);
%end
%% Plot of theta
if HSource == 1
j = 1;
else
j = 0;
end

if dynamics_plots == true
figure(1)
%subplot(2+j,1,1)
plot(t,theta,'-');
xlabel('Time_(s)');
ylabel('$\theta_(radians)$','Interpreter','latex');
title('Magnetic_Moment_Angle')
xlim([t_0 t_f])
yyaxis right
plot(t,H,'r')
ylim([-10*H0 10*H0])
ylabel('H_(kA/m)')
legend('$\theta$', 'H', 'Interpreter', 'latex')

%% Plot of Angular Velocity
dthetadt = LLG_2D(t,theta,gamma,alpha,H0,omega,phi,HSource,H_bias); % Calc dthetadt

```

```

figure (2)
%subplot(2+j,1,2)
plot (t, dthetadt, '-')
xlabel ('Time_(s)');
ylabel ('$ \dot{\theta}$ (radians/s)$', 'Interpreter', 'latex');
title ('Magnetic_Moment_Angular_Velocity')
xlim ([t_0 t_f])
yyaxis right
plot (t,H, 'r')
ylim ([-10*H0 10*H0])
ylabel ('H_(kA/m)')
v1 = legend ('$ \dot{\theta}$', 'H');
set (v1, 'Interpreter', 'latex');

%% Plot of Angular Acceleration
% Calculate angular acceleration (only for sine wave)
if HSource == 1
d2thetadt2 = ...
    -gamma*(1+alpha^2)/(1+alpha)*H0*(omega*cos(omega*t-phi).*sin(theta)...
    + dthetadt.*(sin(omega*t-phi)+H_bias).*cos(theta));

figure (3)
%subplot(3,1,3)
plot (t, d2thetadt2, '-')
xlabel ('Time_(s)');
ylabel ('$ \ddot{\theta}$ (radians/s^2)$', 'Interpreter', 'latex');
title ('Magnetic_Moment_Angular_Acceleration')
xlim ([t_0 t_f])
yyaxis right
plot (t,H, 'r')
ylim ([-10*H0 10*H0])
ylabel ('H_(kA/m)')
al = legend ('$ \ddot{\theta}$', 'H');
set (al, 'Interpreter', 'latex');
end

end

%% Plot of Strain
l1 = 3/2*L0.*(cos(theta).^2-1/3); % ppm, homogeneous strain response
if strain_plot == true

figure (4)
plot (t, l1, '-')
xlabel ('Time_(s)');
ylabel ('$ \lambda_{\theta}$ (ppm)');
title ('Strain_Response')
xlim ([t_0 t_f])
yyaxis right
plot (t,H, 'r')
ylim ([-10*H0 10*H0])
ylabel ('H_(kA/m)')
legend ('$ \lambda_{\theta}$', 'H')
end

%% Fourier Transform
if FFT_plot == true
y = fft (l1);

```

```

N = fs*t_f; % number of samples
fq = fs*(0:N/2-1)/N; % convert to frequency domain

figure(5)
plot(fq,abs(y(1:N/2)/N))
xlabel('f_(Hz)')
ylabel('Magnitude')
title('Model_Amplitude_Spectrum')
ylim([0 sety])
xlim([0 10*f])
%legend(strcat('f-1=',string(f(1))),strcat('f-2=',string(f(2))))
end

%% Motion Animation
% The magnetic moment is blue and the magnetic field is red. Hfactor
% multiplies the magnetic field by a specified constant.
if run_large == true
    e = 1/4;
    a=1;
    theta_r = 0:2*pi;
    r = sqrt(a^2*(1-e^2)/(1-e^2*cos(theta_r)));
    for i=1:step_large:length(t)/t_frac_large
        figure(4)
        polarplot(theta(i)*(0:1),0:1,'b-',[0 0],Hfactor_large*[0 H(i)/Ms], 'r-')
        title(strcat('Time:',{ '-' },string(t(i)), 's'))
    end
end

%% Small Motion Animation
% This animation displays the small angle motion on a polar plot and
% amplifies it so it can be seen better.
if run_small == true
    for i = 1:step_small:length(t)/t_frac_small
        if (abs(1-cos(theta(i))) < theta_limit_0)
            figure(5)
            polarplot(theta_factor_0*theta(i)*(0:1),0:1,'b-',[0 0],Hfactor_small*[0
                H(i)/Ms], 'r-')
            title(strcat('Time:',{ '-' },string(t(i)), 's'))
        else
            figure(6)
            polarplot(0,1,[0 0],Hfactor_small*[0 H(i)/Ms], 'r-')
            title(strcat('Time:',{ '-' },string(t(i)), 's'))
        end
    end
end
end

```

Listing A.5: Two-dimensional magnetostriction nonlinear analysis code in MATLAB.

```

%% Non-linear Analysis
% This is a look into the non-linearity of the system and what it means in
% terms of chaos theory. Hopefully this will provide some insight into the
% system's behavior.
clear;
close all

%% Plots to generate
% state space, delta theta, and poincare
state_plots = 0;

% Amplitude plots for harmonics at different H0
amp_plots = 1;
HH0 = 1; % kA/m, source amplitude range of interest

% H0 varying with theta0
initial_conditions = 0;
theta_i = 0:pi/10:pi; % radians, range of initial theta values

% Plot harmonic amp with different f
f_plots = 0;
ff = 1:1:100; % Hz, range of frequency
omega_vec = 2*pi*ff; % rad/s, angular frequency

%% Adjustable Parameters
% Material Properties
Ms = 4.908e2; % kA/m, Saturation magnetization of Ni at 298K
L0 = -34; % ppm, saturation magnetostriction of Ni
lambda = 4.5e3; % adjustable damping parameter

% Source Properties,  $H = H_0 \sin(\omega t - \phi)$ 
f = 100; % Hz, source frequency:  $\omega = 2\pi * f$ 
H0 = 1; % kA/M, source amplitude
phi = 0; % radians, source phase - if set to  $-\pi/2$ , the source becomes cos

% Initial Conditions and FFT Parameters
theta0 = [2*pi/3 2*pi/3.01]; % radians, initial theta positions. These should
% be close together to examine plots.
t_0 = 1; % s, time where theta and strain plots begin
t_f = 1.1; % s, final time
fs = 1e6; % Hz, FFT sampling frequency

%% Constants and some Calculations
g = 2; % spectroscopic splitting factor for e- spin
e = 1.6e-19; % C, e- charge
c = 3e8; % m/s, speed of light
me = 9.1e-31; % kg, e- mass

gamma = g*e/(2*me*c); % constant related to angular momentum
alpha = lambda/(gamma*Ms); % damping constant
omega = 2*pi*f; % Radians/s source frequency

%% ODE Solver (Runge-Kutta Method)
tspan = 0:1/fs:t_f-1/fs; % s, time span of interest
H = H0*sin(omega*tspan-phi); % magnetic field signal

```

```

t = zeros(length(tspan),length(theta0));
theta = zeros(length(tspan),length(theta0));
if state_plots == 1

for i = 1:length(theta0)
[t(:,i),theta(:,i)] = ...
ode45(@(t,theta) LLG_2D(t,theta,gamma,alpha,H0,omega,phi,1,0),tspan,theta0(i));
end

% Solve for dthetadt and d2thetadt2 for analysis
dthetadt = LLG_2D(t,theta,gamma,alpha,H0,omega,phi,1,0);
d2thetadt2 = ...
-gamma*(1+alpha^2)/(1+alpha)*H0*(omega*cos(omega*t-phi).*sin(theta)...
+ dthetadt.*sin(omega*t-phi).*cos(theta));

%% State Space
% Plot to see the dynamics in phase space
theta_0_pi = wrapToPi(theta);
t_initial = find(t(:,1)>=t_0);

figure(1)
subplot(2,1,1)
plot(theta(t_initial,1),dthetadt(t_initial,1),'-')
xlabel('\theta')
ylabel('\dot{\theta}$', 'Interpreter','latex')
legend(strcat('\theta_0=',string(theta0(1))))
subplot(2,1,2)
plot(theta(t_initial,2),dthetadt(t_initial,2),'-',color=[0.9290 0.6940 0.1250])
xlabel('\theta')
ylabel('\dot{\theta}$', 'Interpreter','latex')
legend(strcat('\theta_0=',string(theta0(2))))
sgtitle('State_Space')

%% Difference in Thetas
delta = theta(:,2) - theta(:,1);
logdelta = log10(abs(delta));
dll = 3/2*L0.*(cos(theta(:,2)).^2-1/3)-3/2*L0.*(cos(theta(:,1)).^2-1/3); % ppm,
homogeneous strain response

figure(2)
subplot(3,1,1)
plot(t(:,1),delta)
ylabel('\Delta\theta', 'FontSize',12)
title('Difference_in_Magnetic_Moment_Direction')
subplot(3,1,2)
plot(t(:,1),logdelta)
ylabel('log|\Delta\theta|', 'FontSize',12)
subplot(3,1,3)
plot(t(:,1),dll)
ylabel('\Delta\lambda_{\theta}', 'FontSize',12)
xlabel('time_(s)', 'FontSize',12)
title('Difference_in_Strain')

%% Angular Acceleration State Space

figure(3)
subplot(2,1,1)
plot(dthetadt(t_initial,1),d2thetadt2(t_initial,1),'-')
xlabel('\dot{\theta}$', 'Interpreter','latex')

```

```

ylabel('$\ddot{\theta}$', 'Interpreter', 'latex')
legend(strcat('\theta_0=', string(theta0(1))))
subplot(2,1,2)
plot(dthetadt(t_initial,2), d2thetadt2(t_initial,2), '- ', color=[0.9290 0.6940 0.1250])
xlabel('$\dot{\theta}$', 'Interpreter', 'latex')
ylabel('$\ddot{\theta}$', 'Interpreter', 'latex')
legend(strcat('\theta_0=', string(theta0(2))))
sgtitle('Angular_Acceleration_State_Space')

%% FFT Difference
ll = 3/2*L0.*(cos(theta).^2-1/3); % ppm, homogeneous strain response
y = fft(ll);

N = fs*t_f; % number of samples
fq = fs*(0:N/2-1)/N; % convert to frequency domain
y = abs(y(1:N/2,:)/(N/2));

figure(10)
plot(fq,y(:,1), '- ', fq,y(:,2), '-. ')
title('FFT')
xlabel('Frequency_(Hz)')
ylabel('Magnitude')
legend(strcat('\theta_0=', string(theta0(1))), strcat('\theta_0=', string(theta0(2))))
xlim([0 20*f])

end

%% Frequency Variation with Amplitude
if amp_plots == true

%tH = zeros(length(t), length(HH0));
%thetaH = zeros(length(t), length(HH0));
dthetadtH = zeros(length(tspan), length(HH0));
for i = 1:length(HH0)
[tH(:,i), thetaH(:,i)] = ...
ode45(@(t, theta) LLG_2D(t, theta, gamma, alpha, HH0(i), omega, phi, 1, 0), tspan, theta0
(1));
dthetadtH(:,i) = LLG_2D(tH(:,i), thetaH(:,i), gamma, alpha, HH0(i), omega, phi, 1, 0);
end

ll = 3/2*L0.*(cos(thetaH).^2-1/3); % ppm, homogeneous strain response
for i = 1:length(HH0)
y(:,i) = fft(ll(:,i));
end

N = fs*t_f; % number of samples
fq = fs*(0:N/2-1)/N; % convert to frequency domain
x_even = f*[4 8 12 16 18 20];
x_odd = f*[3 7 11 15 17 19];
x_tot = f*[1 2 3 4 5 6 7 8 0 10 11 12];
[~, fq_even] = ismember(x_even, fq);
[~, fq_odd] = ismember(x_odd, fq);
[~, fq_tot] = ismember(x_tot, fq);
y = abs(y(1:N/2,:)/(N/2));

figure(4)
plot(HH0,y(fq_tot(1:4),:), '. ')

```

```

title ( 'Frequency_Magnitudes_with_Increasing_Source_Amplitude' )
xlabel ( 'Source_Amplitude_(kA/m)' )
ylabel ( 'Magnitude' )
lgd = legend(strcat(string(x_tot(1:4)), '_Hz'));

% figure (5)
% subplot(2,1,1)
% plot(HH0,y(fq_odd,:),'.')
% legend(strcat(string(x_odd), ' Hz'))
% title('Odd Harmonics')
% ylabel('Magnitude')
% subplot(2,1,2)
% plot(HH0,y(fq_even,:),'.')
% legend(strcat(string(x_even), ' Hz'))
% ylabel('Magnitude')
% xlabel('Source Amplitude (kA/m)')
% title('Even Harmonics')

% Bifurcation Diagram
syms theta t
t_use = tH(tH >= 1.09);
theta_use = thetaH(tH >= 1.09);
sol_vec = [];
sol1 = 0;
% for i = 1:length(t_use)
%     f = -gamma*(1+alpha^2)/(1+alpha)*H0.*sin(omega.*t-phi).*sin(theta);
%     sol = vpasolve(f,[theta, t],[theta_use(i), t_use(i)]);
%
%     if vpa(sol.theta) ~= sol1
%         sol_vec = [sol_vec, vpa(sol.theta)];
%     end
%
%     sol1 = vpa(sol.theta);
% end

figure(15)
plot(H0, sol_vec, '.')
ylabel ('\theta')
xlabel ('H_0')
end

%% Variation of Frequency with Initial Conditions
if initial_conditions == 1

for i = 1:length(theta_i)
[t_th(:,i), theta_th(:,i)] = ...
    ode45(@(t,theta) LLG_2D(t,theta, gamma, alpha, H0, omega, phi), tspan, theta_i(i));
end

l1 = 3/2*L0.*(cos(theta_th).^2-1/3); % ppm, homogeneous strain response
for i = 1:length(theta_i)
y(:,i) = fft(l1(:,i));
end

N = fs*t_f; % number of samples

```

```

fq = fs*(0:N/2-1)/N; % convert to frequency domain
x_even = f*[4 8 12 16 18 20];
x_odd = f*[3 7 11 15 17 19];
x_tot = f*[1 2 3 4 5 6 7 8 0 10 11 12];
[~,fq_even] = ismember(x_even,fq);
[~,fq_odd] = ismember(x_odd,fq);
[~,fq_tot] = ismember(x_tot,fq);
y = abs(y(1:N/2,:)/(N/2));

figure(6)
plot(theta_i,y(fq_tot(1:4),:),'.')
title('Frequency_Magnitudes_with_theta_0')
xlabel('\theta_0')
ylabel('Magnitude')
lgd = legend(strcat(string(x_tot(1:4)),'_Hz'));

figure(7)
subplot(2,1,1)
plot(theta_i,y(fq_odd,:),'.')
legend(strcat(string(x_odd),'_Hz'))
title('Odd_Harmonics')
xlabel('\theta_0')
ylabel('Magnitude')
subplot(2,1,2)
plot(theta_i,y(fq_even,:),'.')
legend(strcat(string(x_even),'_Hz'))
xlabel('\theta_0')
ylabel('Magnitude')
title('Even_Harmonics')

end

%% Response Magnitude Frequency Dependence
if f_plots == true

%t_f = zeros(length(t),length(HH0));
%thetaf = zeros(length(t),length(HH0));
for i = 1:length(ff)
[t_ff(:,i),thetaf(:,i)] = ...
ode45(@(t,theta) LLG_2D(t,theta,gamma,alpha,H0,omega_vec(i),phi),tspan,theta0(1)
);
end

l1 = 3/2*L0.*(cos(thetaf).^2-1/3); % ppm, homogeneous strain response
for i =1:length(ff)
y(:,i) = fft(l1(:,i));
end

N = fs*t_f; % number of samples
fq = fs*(0:N/2-1)/N; % convert to frequency domain

for j = 1:length(ff)
x_even(j,:) = ff(j)*[4 8 12 16 18 20];
x_odd(j,:) = ff(j)*[3 7 11 15 17 19];
x_tot(j,:) = ff(j)*[1 2 3 4 5 6 7 8 0 10 11 12];
end
[~,fq_even] = ismember(x_even,fq);
[~,fq_odd] = ismember(x_odd,fq);
[~,fq_tot] = ismember(x_tot,fq);

```

```

y = abs(y(1:N/2,:)/(N/2));

figure(8)
plot(ff,y(fq_tot(1:2),:),'.')
title('Response_Amplitudes_with_Source_Frequency')
xlabel('Source_Frequency_(Hz)')
ylabel('Response_Magnitude')
lgd = legend('Driving_f','Double_f');

% figure(9)
% subplot(2,1,1)
% plot(ff,y(fq_odd,:),'.')
% legend(strcat(string(x_odd),' Hz'))
% title('Odd Harmonics')
% ylabel('Magnitude')
% subplot(2,1,2)
% plot(ff,y(fq_even,:),'.')
% legend(strcat(string(x_even),' Hz'))
% ylabel('Magnitude')
% xlabel('Source Amplitude (kA/m)')
% title('Even Harmonics')

end

```

Listing A.6: Two-dimensional LLG function used in other two-dimensional codes.

```
%% Equation of Motion  
% function used in 2D simulation  
function dthetadt = LLG_2D(t, theta, gamma, alpha, H0, omega, phi, HSource, H_bias)  
if HSource == 1  
dthetadt = ...  
    -gamma*(1+alpha^2)/(1+alpha)*(H0.*sin(omega.*t-phi)+H_bias).*sin(theta);  
else  
dthetadt = ...  
    -gamma*(1+alpha^2)/(1+alpha)*(H0.*square(omega*t)+H_bias).*sin(theta);  
end  
end
```

Listing A.7: Three-dimensional magnetostriction model code in Python.

```

# This code is used to run a single simulation with
# a 3D magnetostriction model.

# Run Number
num = 0          # define the number label of the run here, this will create a
                # new folder for the outputs

# Import packages
import oommfc as mc
import discretisedfield as df
import micromagneticmodel as mm
import numpy as np
import matplotlib.pyplot as plt
import random
import os

# Time setup
tfinal = 1      # Final time of simulation
tstep = 1e-6    # timestep in seconds
ntot = 1000     # total number of time steps
# Material properties
A_ex = 15e-12   # exchange constant
L1 = -24        # Strain constant 1 in ppm
L2 = -48        # Strain constant 2 in ppm
#Ku = -0.5e4    # anisotropy constant
#u_easy = (1, 0, 1) # easy axis
#u_hard = (0, 1, 0) # hard axis
damping = 0.9   # damping constant (alpha)
Ms = 4.8e5      # magnetization saturation (A/m)
# Alternating source properties
source_freq = 100 # source frequency (Hz)
H_app = (0, 0, 1.3e4) # applied field (A/m)
source_type = 'sin' # waveform of source
# Strain measurement axis
B = np.array([0,0,1])
# Geometry of object
r = 5e-9        # material radius, m
L = 1e-8        # material length, m
d = .5e-9       # domain dimensions, m

# Create a new folder with name model_{num}
newpath = r'C:\Users\Tomas\Desktop\Martin_Group\ubermag_images\model_'
newpath = newpath + str(num)
if not os.path.exists(newpath):
    os.makedirs(newpath)

# Create a new file with all parameters written into it
newfile = newpath + r'\parameters.txt'
f = open(newfile, "w")
f.write(
f"""
# Run Number
num = {str(num)}          # define the number label of the run here, this
                        # will create a new folder for the outputs
# Time setup
tfinal = {str(tfinal)}   # Final time of simulation in seconds

```

```

tstep = {str(tstep)}           # timestep in seconds
ntot = {str(ntot)}           # total number of time steps
# Material properties
A_ex = {str(A_ex)}           # exchange constant
L1 = {str(L1)}               # Strain constant 1 in ppm
L2 = {str(L2)}               # Strain constant 2 in ppm
damping = {str(damping)}     # damping constant (alpha)
Ms = {str(Ms)}               # magnetization saturation (A/m)
# Alternating source properties
source_freq = {str(source_freq)} # source frequency (Hz)
H_app = {str(H_app)}         # applied field (A/m)
source_type = {source_type}  # waveform of source
# Strain measurement axis
B = {str(B)}
# Geometry of object
r = {str(r)}                 # material radius (m)
L = {str(L)}                 # material length (m)
d = {str(d)}                 # domain dimensions (m)
"""
)

f.close()

# Define initial mesh
p1 = (-r, -r, -L/2)          # Starting point
p2 = (r, r, L/2)            # Ending point
cell = (d, d, d)            # Cell size
region = df.Region(p1=p1, p2=p2) # Define the region
mesh = df.Mesh(region=region, cell=cell) # Create the mesh

# Define the system name
system = mm.System(name='time_dependent_field')

# Define system energy
system.energy = (mm.Zeeman(H=H_app, func='sin', f=source_freq, t0=0)
                + mm.Demag()
                + mm.Exchange(A=A_ex))
#                + mm.CubicAnisotropy(K=Ku, u1=u_easy, u2=u_hard))

# Define system dynamics
system.dynamics = mm.Precession(gamma0=mm.consts.gamma0) + mm.Damping(alpha=damping)

def Ms_fun(pos):
    """Function to set magnitude of magnetisation: zero outside cylindric shape,
    Ms inside cylinder.

    Cylinder radius is r.

    """
    x, y, z = pos
    if (x**2 + y**2)**0.5 < r:
        return Ms
    else:
        return 0

# Define the field element
system.m = df.Field(mesh, dim=3, value=(0,0,0), norm=Ms_fun)

```

```

# Assign a random value of 4 defined states to each cell to represent the different
domains.
i_states = {'state_1':(1,1,1), 'state_2':(-1,-1,-1), 'state_3':(-1,1,-1), 'state_4':
:(1,-1,1)}
n = len(system.m.array[0,0])
i=0
for array_mass in system.m.array:
    j=0
    for array_element in system.m.array[i]:
        array_element = np.array(random.choices(list(i_states.values()),k=n))
        system.m.array[i,j] = array_element
        j+=1
    i+=1

# Redefine the field element to define the cylindrical shape again
system.m = df.Field(mesh, dim=3, value = system.m.array, norm=Ms_fun)

# Plot the initial magnetization of one cross section that is one cell thick
system.m.plane('z').mpl()
plt.savefig(newpath+r'\initial_mag.jpg')

# Evolve the system
ev = mc.RungeKuttaEvolver(min_timestep=tstep) # Define the evolver as Runge Kutta
method
td = mc.TimeDriver(evolver=ev) # Setup time driver with evolver input
td.drive(system, t=tfinal, n=ntot, verbose=2) # Drive the system

# Plot the external magnetic field
system.table.mpl(y=['Bx_zeeman', 'By_zeeman', 'Bz_zeeman'])
plt.legend(['$H_x$', '$H_y$', '$H_z$'])
plt.title('External_Field')
plt.ylabel('Field_Magnitude_(kA/m)')
plt.savefig(newpath+r'\mag_field.jpg')

# Plot the normalized magnetization
system.table.mpl(y=['mx', 'my', 'mz'])
plt.legend(['$m_x$', '$m_y$', '$m_z$'])
plt.ylabel('m')
plt.title('Normalized_Magnetization')
plt.savefig(newpath+r'\magnetization.jpg')

# Assign magnetization data to x,y,z variables.
mx = system.table.data['mx']
my = system.table.data['my']
mz = system.table.data['mz']

# Normalize the strain measurement axis and separate into x,y,z.
B = B/np.linalg.norm(B)
Bx = B[0]
By = B[1]
Bz = B[2]

# Strain calculation for cubic anisotropy
l1 = 3/2*L1*(mx**2*Bx**2+my**2*By**2+mz**2*Bz**2-1/3)+3*L2*(mx*my*Bx*By+my*mz*By*Bz+
mz*mx*Bz*Bx)

# Define a new column in the data for the strain
system.table.data['l1'] = l1

```

```

# Plot the strain response
system.table.mpl(y=['l1'])
plt.legend().remove()
plt.title('Model_Strain_Response')
plt.ylabel(r'$\lambda$(ppm)')
plt.savefig(newpath+r'\strain.jpg')

# FFT setup
from numpy.fft import fft, ifft
x = np.array(system.table.data['l1'])
fft_l1 = fft(x)
N = len(fft_l1)
n = np.arange(N)
T = tfinal

tt = np.max(system.table.data['t'])
freq = n/T

# Plot the amplitude spectrum
plt.stem(freq, np.abs(fft_l1)/N, 'b', \
         markerfmt="_", basefmt="-b")
plt.xlabel('f_(Hz)')
plt.ylabel('Magnitude')
plt.xlim(0, 5.5*source_freq)
plt.ylim(0, 1)
plt.title('Model_Amplitude_Spectrum')
plt.savefig(newpath+r'\amp_spectrum.jpg')

```

Listing A.8: Three-dimensional magnetostriction model code for multiple simulations in Python.

```

# This code is used to produce multiple folders with 3D simulation results.
# Vary one parameter at a time and plot the powerspectrum results from the folders.

# Import packages
import oommfc as mc
import discretisedfield as df
import micromagneticmodel as mm
import numpy as np
import matplotlib.pyplot as plt
import os
import pandas as pd

# define the number label of the run here, this will create a new folder for the
  outputs
newpath = r'C:\Users\Tomas\Desktop\Martin_Group\3D_results\H_field_high-' # define
  model location and name here
# Run Number
num = 1      # initial number of run to start at
num_runs = 40 # number of simulations to run
# Parameters to change:
edit_damping = False # edit damping parameter (True or False)
damping_change = 0.01 # how much to increase the damping parameter each iteration

edit_H = True # edit applied magnetic field (True or False)
H_change = np.array((0,0,5)) # how much to increase the field each iteration (Bx,By
  ,Bz)

edit_T = False # edit temperature (True or False)
temp_change = 1 # how much to increase the temperature each iteration (C)

# Time setup
tfinal = .5 # Final time of simulation
tstep = 1e-5 # timestep in seconds
ntot = int(tfinal/tstep) # total number of time steps
# Material properties
A_ex = 15e-12 # exchange constant
L1 = -24 # Strain constant 1 (<100> cubic direction) in ppm
L2 = -48 # Strain constant 2 (<111> cubic direction) in ppm
K1 = -0.5e5/1.257e2 # anisotropy constant 1 J/m^3: K1 < 0 indicates hard axis ,
  K1 > 0 easy axis
K2 = -0.2e5/1.257e2 # anisotropy constant 2 J/m^3, not callable in this code
u_11 = (1, 0, 0) # K1 axis one: will be hard axis if K1 < 0, easy axis if K1 > 0
u_12 = (0, 1, 0) # K1 axis 2: just needs to be orthogonal to u_11
damping = .75 # damping constant (alpha)
Ms = 5.35e5 # magnetization saturation (A/m)
Tc = 631 # K, Curie temperature
M0 = 5.4e5 # Ms at 0K (A/m)
# Alternating source properties
source_freq = 100 # source frequency (Hz)
H_app = (0, 0, 10) # applied field (A/m) in (x,y,z) coordinates
source_type = 'sin' # waveform of source
# Strain measurement axis
B = np.array([0,0,1]) # ([x,y,z])
# Geometry of object
r = 1e-9 # material radius, m (this is only a radius if making a cylinder
  )

```

```

L = 2*r          # material length, m
d = 1e-9        # cell dimensions, m
# Temperature modeling
Temp = 294      # Temperature in K
'''
t = Temp/Tc     # fractional temperature

# function to determine magnetization saturation
def fn1(m):
    return m - np.tanh(m/t)

m = sp.optimize.brentq(fn1,0.001,2) # fractional mag sat
Ms = M0*m       # saturation at given temperature

# Sigmoid function definition
def sigmoid(x):
    return 0.12677279-0.10035642 / (1 + np.exp(-0.0851499*(x-69.35616788)))

# Apply the sigmoid function to temperature
damping = sigmoid(Temp)
'''

def Ms_fun(pos):
    """Function to set magnitude of magnetisation: zero outside cylindric shape,
    Ms inside cylinder.

    Cylinder radius is r.

    """
    x, y, z = pos
    if (x**2 + y**2)**0.5 < r:
        return Ms
    else:
        return 0

def cube_fun(pos):
    """Function to set values for a 4x4 cube

    """
    i_states = {'state_1':(1,0,1), 'state_2':(-1,0,-1), 'state_3':(0,1,0), 'state_4':
                :(0,-1,0)}
    x, y, z = pos
    if x > 0 and y > 0 and z > 0:
        return i_states['state_1']
    if x > 0 and y < 0 and z > 0:
        return i_states['state_3']
    if x < 0 and y < 0 and z > 0:
        return i_states['state_2']
    if x < 0 and y > 0 and z > 0:
        return i_states['state_4']
    if x > 0 and y > 0 and z < 0:
        return i_states['state_3']
    if x > 0 and y < 0 and z < 0:
        return i_states['state_2']
    if x < 0 and y < 0 and z < 0:
        return i_states['state_4']
    if x < 0 and y > 0 and z < 0:
        return i_states['state_1']

```

```

for j in range(0,num_runs):
    #display run number
    print("Run_Number:_",str(num))
    newpath = newpath + str(num) # appends the number (num) of the run to the file
    name
    if not os.path.exists(newpath):
        os.makedirs(newpath)
    # Create a new file with all parameters written into it
    newfile = newpath + r'\parameters.txt'
    f = open(newfile,"w")
    f.write(
    f"""
    # Run Number
    num = {str(num)} # define the number label of the run here,
    this will create a new folder for the outputs
    # Time setup
    tfinal = {str(tfinal)} # Final time of simulation in seconds
    timestep = {str(tstep)} # timestep in seconds
    ntot = {str(ntot)} # total number of time steps
    # Material properties
    A_ex = {str(A_ex)} # exchange constant
    L1 = {str(L1)} # Strain constant 1 in ppm
    L2 = {str(L2)} # Strain constant 2 in ppm
    K1 = {str(K1)} # anisotropy constant 1
    K2 = {str(K2)} # anisotropy constant 2
    u_easy = {str(u_11)} # axis 1 for K1
    u_hard = {str(u_12)} # axis 2 for K1
    damping = {str(damping)} # damping constant (alpha)
    Ms = {str(Ms)} # magnetization saturation (A/m)
    Tc = {str(Tc)} # K, Curie temperature
    M0 = {str(M0)} # Ms at 0K (A/m)
    # Alternating source properties
    source_freq = {str(source_freq)} # source frequency (Hz)
    H_app = {str(H_app)} # applied field (A/m)
    source_type = {source_type} # waveform of source
    # Strain measurement axis
    B = {str(B)}
    # Geometry of object
    r = {str(r)} # material radius (m)
    L = {str(L)} # material length (m)
    d = {str(d)} # cell dimensions (m)
    # Temperature modeling
    T = {str(Temp)} # Temperature in K
    """
    )

    f.close()

    # Define initial mesh
    p1 = (-r, -r, -L/2) # Starting point
    p2 = (r, r, L/2) # Ending point
    cell = (d, d, d) # Cell size
    region = df.Region(p1=p1, p2=p2) # Define the region
    mesh = df.Mesh(region=region, cell=cell) # Create the mesh

    # Initial mesh
    mesh.k3d()

    # Define the system name

```

```

system = mm.System(name='time_dependent_field')

# Define system energy
system.energy = (mm.Zeeman(H=H_app, func=source_type, f=source_freq, t0=0)
                + mm.Demag()
                + mm.Exchange(A=A_ex)
                + mm.CubicAnisotropy(K=K1, u1=u_11, u2=u_12))

# Define system dynamics
system.dynamics = mm.Precession(gamma0=mm.consts.gamma0) + mm.Damping(alpha=
    damping)

# Define the field element
system.m = df.Field(mesh, dim=3, value=cube_fun, norm=Ms)

# Plot the initial magnetization of one cross section that is one cell thick
system.m.plane('z').mpl()
plt.savefig(newpath+r'\initial_mag.jpg')

ev = mc.RungeKuttaEvolver(min_timestep= timestep) # Define the evolver as Runge
    Kutta method
td = mc.TimeDriver(evolver=ev) # Setup time driver with evolver
    input
td.drive(system, n=ntot, t=tfinal, verbose=2) # Drive the system

# Plot the external magnetic field
system.table.mpl(y=['Bx_zeeman', 'By_zeeman', 'Bz_zeeman'])
plt.legend(['$H_x$', '$H_y$', '$H_z$'])
plt.title('External_Field')
plt.ylabel('Field_Magnitude_(kA/m)')
plt.savefig(newpath+r'\mag_field.jpg')

# Plot the normalized magnetization
system.table.mpl(y=['mx', 'my', 'mz'])
plt.legend(['$m_x$', '$m_y$', '$m_z$'])
plt.ylabel('m')
plt.title('Normalized_Magnetization')
plt.savefig(newpath+r'\magnetization.jpg')

# Assign magnetization data to x,y,z variables.
mx = system.table.data['mx']
my = system.table.data['my']
mz = system.table.data['mz']

# Normalize the strain measurement axis and separate into x,y,z.
B = B/np.linalg.norm(B)
Bx = B[0]
By = B[1]
Bz = B[2]

# Strain calculation for cubic anisotropy
ll = 3/2*L1*(mx**2*Bx**2+my**2*By**2+mz**2*Bz**2-1/3)+3*L2*(mx*my*Bx*By+my*mz*By
    *Bz+mz*mx*Bz*Bx)
ll_rate = [0]
# calculate strain rate by numerical differentiation over one time step
for i in range(0, len(ll)-1):
    ll_rate_i = (ll[i+1]-ll[i])/(system.table.data['t'][1]-system.table.data['t']
        [0])
    ll_rate.append(ll_rate_i)

```

```

# Define a new column in the data for the strain
system.table.data['ll'] = ll
system.table.data['ll_rate'] = ll_rate

# Plot the strain response
system.table.mpl(y=['ll'])
plt.legend().remove()
plt.title('Model Strain Response')
plt.ylabel(r'$\lambda$ (ppm)')
plt.savefig(newpath+r'\strain.jpg')

# Plot the strain response zoomed
#system.table.mpl(y=['ll'])
#plt.legend().remove()
#plt.title('Model Strain Response')
#plt.ylabel(r'$\lambda$ (ppm)')
#plt.xlim([28,30])
#plt.ylim([7.5875,7.595])
#plt.savefig(newpath+r'\strain_zoom.jpg')

# plot strain rate response
system.table.mpl(y=['ll_rate'])
plt.legend().remove()
plt.title('Model Strain Rate')
plt.ylabel(r'$\frac{d\lambda}{dt}$ (ppm/s)')
plt.savefig(newpath+r'\strain_rate.jpg')

# zoomed strain rate response
#system.table.mpl(y=['ll_rate'])
#plt.legend().remove()
#plt.title('Model Strain Rate')
#plt.ylabel(r'$\frac{d\lambda}{dt}$ (ppm/s)')
#plt.ylim([-500,500])
#plt.xlim([29.8,30])
#plt.savefig(newpath+r'\strain_rate_zoom.jpg')

# FFT setup
from scipy.fft import fft, fftfreq
T = system.table.data['t'][1] - system.table.data['t'][0]
y = np.array(system.table.data['ll'])

fft_ll = fft(y)
N = len(y)
x = np.linspace(0.0, N*T, N, endpoint=False)

xf = fftfreq(N, T)[:N//2]

PS = 2*np.abs(fft_ll[0:N//2])/N

# Plot the amplitude spectrum
#plt.plot(xf, PS)
#plt.xlabel('f (Hz)')
#plt.ylabel('Magnitude')
#plt.xlim(0,5*source_freq)
#plt.ylim(0,0.001)
#plt.grid()
#plt.title('Model Amplitude Spectrum')
#plt.savefig(newpath+r'\amp_spectrum.jpg')

```

```

# Export Data
system.table.data.to_csv(newpath+r'/data.csv')
dff = pd.DataFrame({'frequency':xf, 'Amplitude':PS})
dff.to_csv(newpath+r'/Power_Spectrum.csv')

# FFT setup
T = system.table.data['t'][1]-system.table.data['t'][0]
y = np.array(system.table.data['ll'][system.table.data['t']>.1])

fft_ll = fft(y)
N = len(fft_ll)
x = np.linspace(0.0, N*T, N, endpoint=False)

xf = fftfreq(N, T)[:N//2]

PS = 2*np.abs(fft_ll[0:N//2])/N

# Record the amplitude at 100Hz, 200Hz, and harmonics up to 1000Hz
peak_f = [100,200,300,400,500,600,700,800,900,1000]
peaks = [PS[40],PS[80],PS[120],PS[160],PS[200],PS[240],PS[280],PS[320],PS[360],
        PS[400]]
df_peak = pd.DataFrame({'frequency':peak_f, 'Amplitude':peaks})
df_peak.to_csv(newpath+r'/peak_values.csv')
# Plot the amplitude spectrum
#plt.plot(xf, PS)
#plt.grid()
#plt.xlabel('f (Hz)')
#plt.ylabel('Magnitude')
#plt.xlim(0,5*source_freq)

#plt.ylim(0,.2)
#plt.title('Filtered Model Amplitude Spectrum')
#plt.savefig(newpath+r'\amp_spectrum_filtered.jpg')

# FFT setup for strain rate
T = system.table.data['t'][1]-system.table.data['t'][0]
y = np.array(system.table.data['ll_rate'][system.table.data['t']>.1])

fft_ll = fft(y)
N = len(fft_ll)
x = np.linspace(0.0, N*T, N, endpoint=False)

xf_rate = fftfreq(N, T)[:N//2]

PS_rate = 2*np.abs(fft_ll[0:N//2])/N

# Plot the amplitude spectrum of the strain rate
#plt.plot(xf_rate, PS_rate)
#plt.xlabel('f (Hz)')
#plt.ylabel('Magnitude')
#plt.xlim(0,5*source_freq)
#plt.ylim(0,0.01)
#plt.grid()
#plt.title('Model Strain Rate Amplitude Spectrum')
#plt.savefig(newpath+r'\amp_spectrum_filtered_strain_rate.jpg')

df_rate = pd.DataFrame({'frequency':xf_rate, 'Amplitude':PS_rate})
df_rate.to_csv(newpath+r'/Rate_Power_Spectrum.csv')

```

```
# edit damping constant for next run
if edit_damping:
    damping += damping_change      # damping constant (alpha)
# edit magnetic field strength for next run
if edit_H:
    H_app = tuple(np.array(H_app) + H_change)
# edit temperature for next run
if edit_T:
    Temp += temp_change
#edit run number for next run
num += 1
```

APPENDIX B
SOIL BOX FOR ENVIRONMENTAL CONDITION STUDIES

A soil box was prepared for experiments with the DMS fiber exposed to different temperatures, soil saturation levels, and different amounts of magnetic material embedded in the soil, as shown in Figure B.1. Temperature probes were placed at even spacing along the length of the fiber. These probes can be heated to a specified temperature, allowing us to develop an understanding of how the DMS fiber response varies with temperature in reality. Future research could use this experiment to determine how the DMS fiber response changes based on soil conditions.



Figure B.1 This figure shows the sandbox experimental setup. Temperature probes are evenly spaced at the top of the box. The solenoid is shown near the bottom of the box. The DMS fiber is buried shallow between the solenoid and temperature probes

APPENDIX C

FIBER MANUAL ALIGNMENT METHOD

The manual alignment method can be difficult to accomplish, so this appendix covers good practices to make completing the alignment easier. The instructions outlined for alignment in this appendix reference the Fujikura FSM-70S Fusion Splicer shown in Figure C.1, however, other splicers may involve similar steps. The steps that we have typically taken in manual alignment are the following:

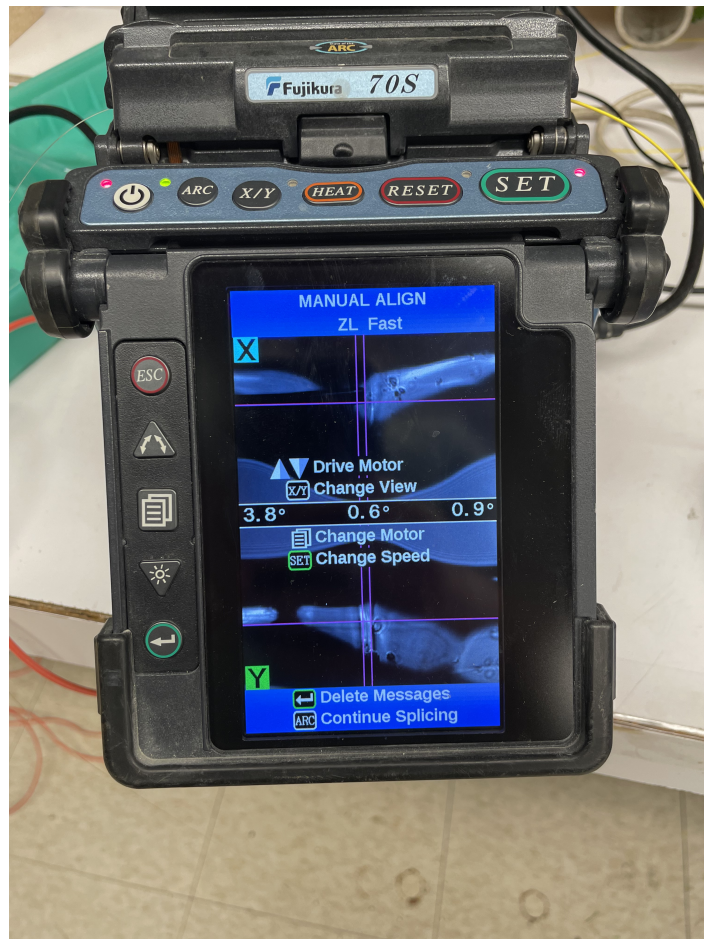


Figure C.1 This figure shows the Fujikura FSM-70S Fusion Splicer manual alignment screen. Shown on the screen, a DMS fiber is being aligned with an acoustic fiber, with index matching gel applied.

1. Put on rubber gloves and protective eyewear to prevent any injury from sharp fiber pieces.
2. Remove the sheath from the end of some scrap acoustic fiber and set aside. This will be used at a later step.

3. Turn on the interrogator, ensuring the laser is off.
4. Open the OTDR on the interrogator.
5. Turn on the splicer.
6. Navigate to the “Splice Menu” by clicking the ”Main Menu” button.
7. Select “Select Splice Mode” in the “Splice Menu”.
8. Select “SM-SM” if it is not already selected.
9. Return to the “Splice Menu”.
10. Select “Splice Settings”.
11. Change the “Operation Mode” to “Manual”, if not already set.
12. Press “ESC” to return to the initial screen.
13. Remove the sheath from the end of the acoustic fiber and cleave it.
14. Clean the end of the acoustic fiber with an alcohol wipe and clean the tip with tape.
15. Place the acoustic fiber into the splicer by clamping it on its sheath, with the exposed fiber tip near the metal tips in the center.
16. Remove the coating from the end of the DMS fiber and cleave it. Removing the coating is best done using a razor blade. You should scrape the coating off slowly, holding the blade nearly parallel to the fiber. The coating should peel off as you scrape. If it does not peel off, you may have to press slightly harder into the coating with the razor.
17. Clean the DMS fiber with an alcohol wipe and clean the tip with tape.
18. Place the DMS fiber into the splicer by gently clamping it on its coating, with the exposed fiber tip near the metal tips in the center.
19. Run the splicer by clicking “SET” and ensure the lids close so the fiber is not exposed.
20. If the splicer accepts both fiber cleaves, continue with the next steps. Otherwise, remove and attempt cleaning the fiber with a bad cleave. Place the fiber back into the splicer and rerun the splice. If this does not work, remove and cleave the fiber again.
21. If both fiber cleaves are accepted, carefully open the lids to the fibers in order to not move them.

22. Pick up the scrap acoustic fiber from step 2 and dip the end into the index matching gel.
23. Using the scarp fiber, gently rub the index matching gel onto the connection point of the two fibers in the splicer.
24. Close the lid to the fibers.
25. Turn on the interrogator laser to check the OTDR. The next steps will outline how to align the fiber to achieve good transmission, shown in Figure C.2.
26. If the OTDR does not show good transmission, adjust the position of one of the fibers using the up and down arrows next to the splicer screen. It is recommended to choose a slow motor speed with the “SET” button. You can change which direction you are aligning in with the document button, between the arrows left of the screen.
27. Once the OTDR shows a signal similar to that in Figure C.2, leave the splicer on and begin your experiment. DO NOT touch the splicer, you may have to realign. NOTE: the alignment may slip during experiments; ensure you check the OTDR and realign if this occurs.

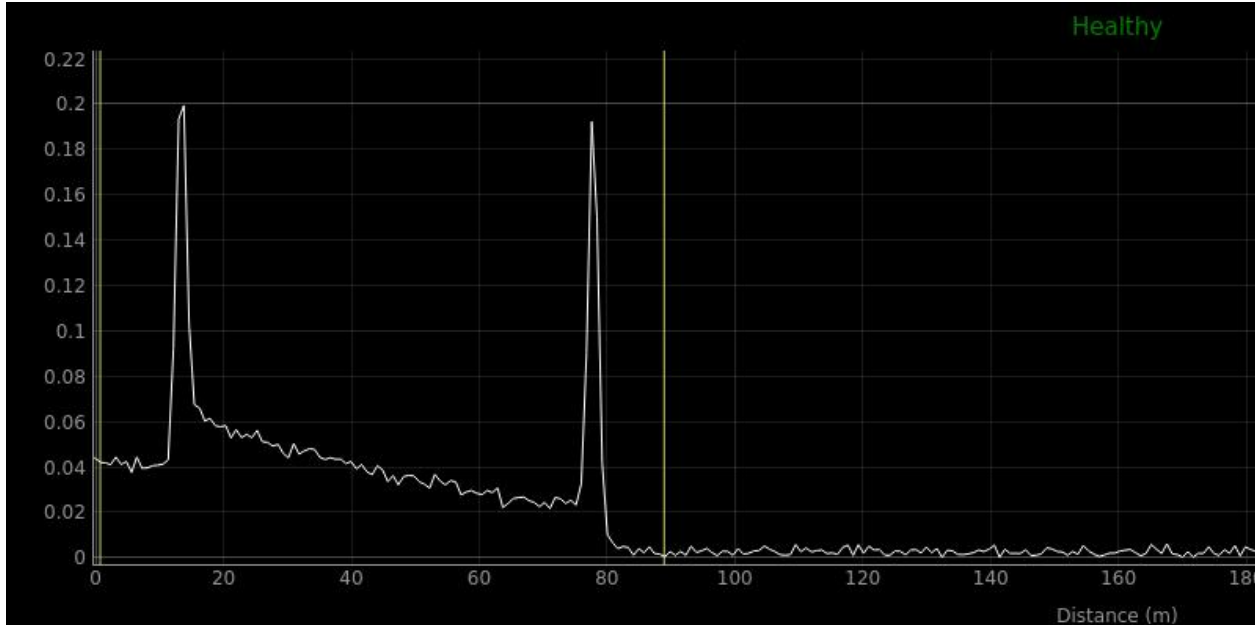


Figure C.2 This figure shows an example of what a good alignment, allowing for transmission of light through the fiber, looks like on the OTDR. There should be a peak at the manual alignment position, followed by a steady decrease along the length of the fiber, and a peak at the end of the fiber. The peaks indicate points of greater back-scattering. The lower you can get the first peak with alignment, the better the alignment is.

APPENDIX D
FURTHER TWO-DIMENSIONAL MODELING

The two-dimensional modeling involved many simulations, most of which resulted in nothing of note. One interesting result, also discussed in the thesis, involves the evolution of higher harmonics with increasing applied magnetic field magnitude. In Figure D.1, for a 100 Hz source, we can see the difference between the even harmonic multiples of the source frequency, $f_{even} = 2nf_s$ and the odd harmonic multiples of the source frequency, $f_{odd} = (2n + 1)f_s$, where $n = 1, 2, 3, \dots$. Essentially, at magnetic fields below ~ 18 kA/m, the even and odd harmonics demonstrate similar trends. At magnetic fields higher than ~ 18 kA/m, we see that the even harmonics dominate the signal, while the odd harmonics show lower amplitudes with some small increases in amplitude at certain magnetic field amplitudes. This could be because larger magnetic field amplitudes force the magnetization vector to point mainly in the direction of the external magnetic field, creating less opportunity for oscillation at the odd harmonic frequencies. However, this explanation is not satisfactory and more research is needed to explain this result.

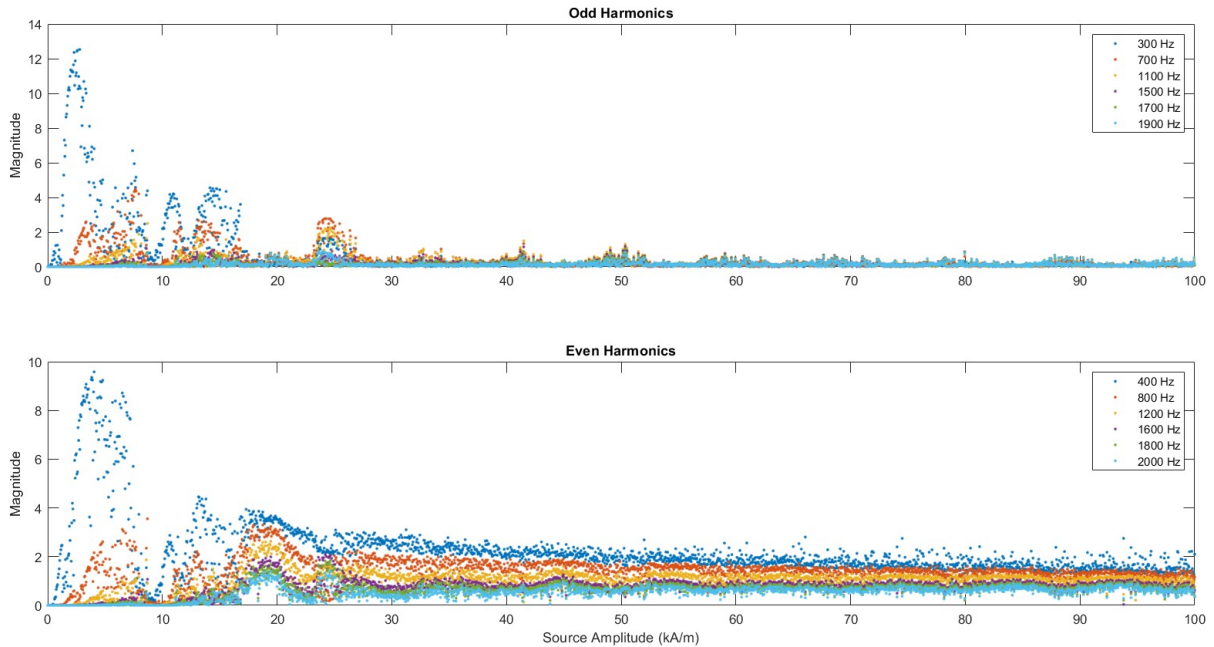


Figure D.1 This figure shows plots of the odd harmonic (top) and even harmonic (bottom) peak amplitudes at increasing magnetic field strength. Magnitude is in units of $\mu\varepsilon$.

Additional modeling involved determining how the peak amplitudes changed based on the initial condition, θ_0 . Figure D.2 demonstrates this relationship for a source frequency of 100 Hz and magnetic field amplitude of 8 kA/m. Interestingly, the peak amplitudes of the 100 Hz, 200 Hz, 300 Hz, and 400 Hz peaks vary greatly depending on θ_0 . The general trend seems to suggest that as the initial angle between the applied magnetic field and the magnetization vector increases, so too do the peak amplitudes. This could be due to increased initial torque on the magnetization vector, which increases the oscillation for the duration of the simulation. This amplitude spectrum is only of the first 2 s of the signal, so it is possible that the difference in peak amplitude over time is not so dramatic. More research into this would need to be performed to determine the exact reason and how this changes with longer simulation times.

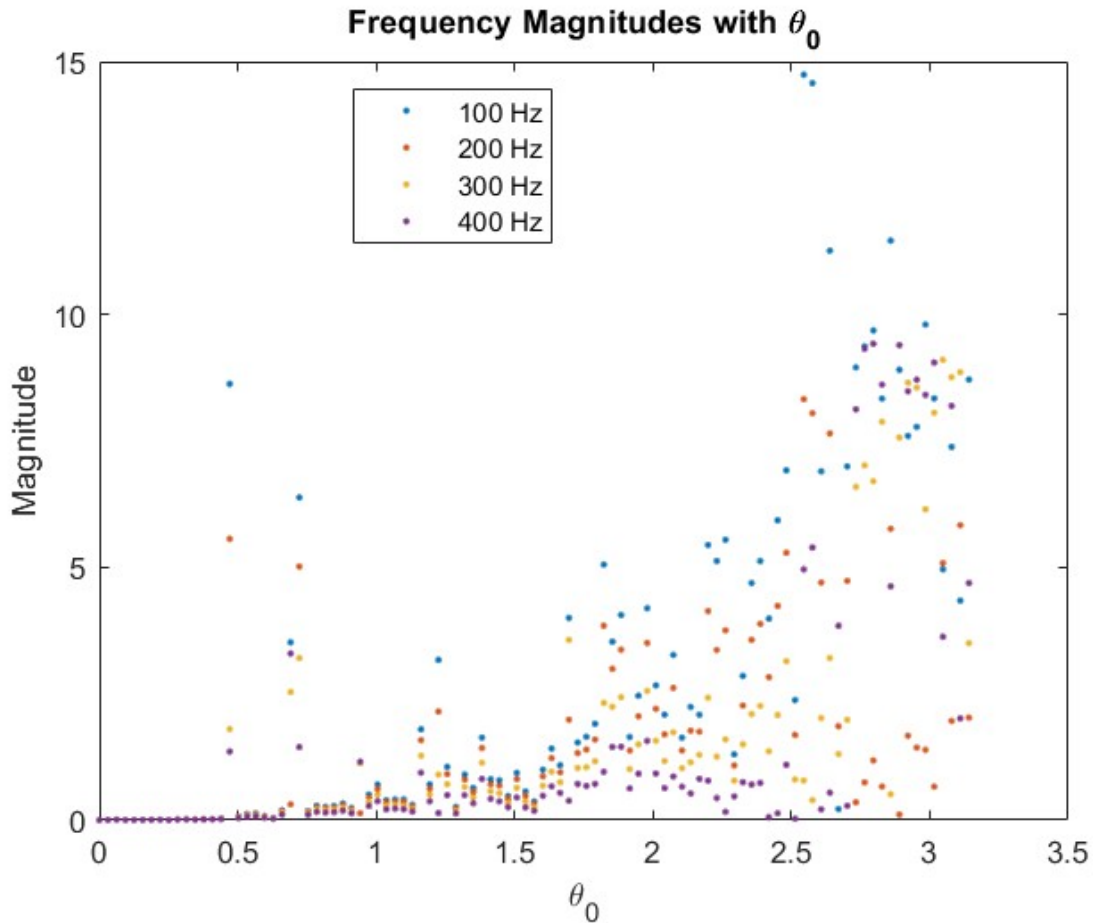


Figure D.2 This figure shows how peak amplitudes in the amplitude spectrum change based on the initial angle between the external magnetic field and the magnetization vector, θ_0 in the two-dimensional model. Magnitude is in units of $\mu\varepsilon$.

Modeling to determine whether the two-dimensional simulations exhibit chaos was also performed. This involved the creation of phase space plots, seen in Figure D.3, which plot angular position, θ , against

angular velocity $\dot{\theta}$. In these images, two different initial angles are plotted to demonstrate how small differences in the initial angle can change the resulting phase space plot. This is a characteristic of chaotic systems, suggesting this system may exhibit chaos at certain magnetic field strengths. More research would need to be performed to determine if this particular system demonstrates chaos. Chaos has been shown for certain conditions with the LLG equation in previous studies, e.g. Lakshmanan (2011) and Smith *et al.* (2010).

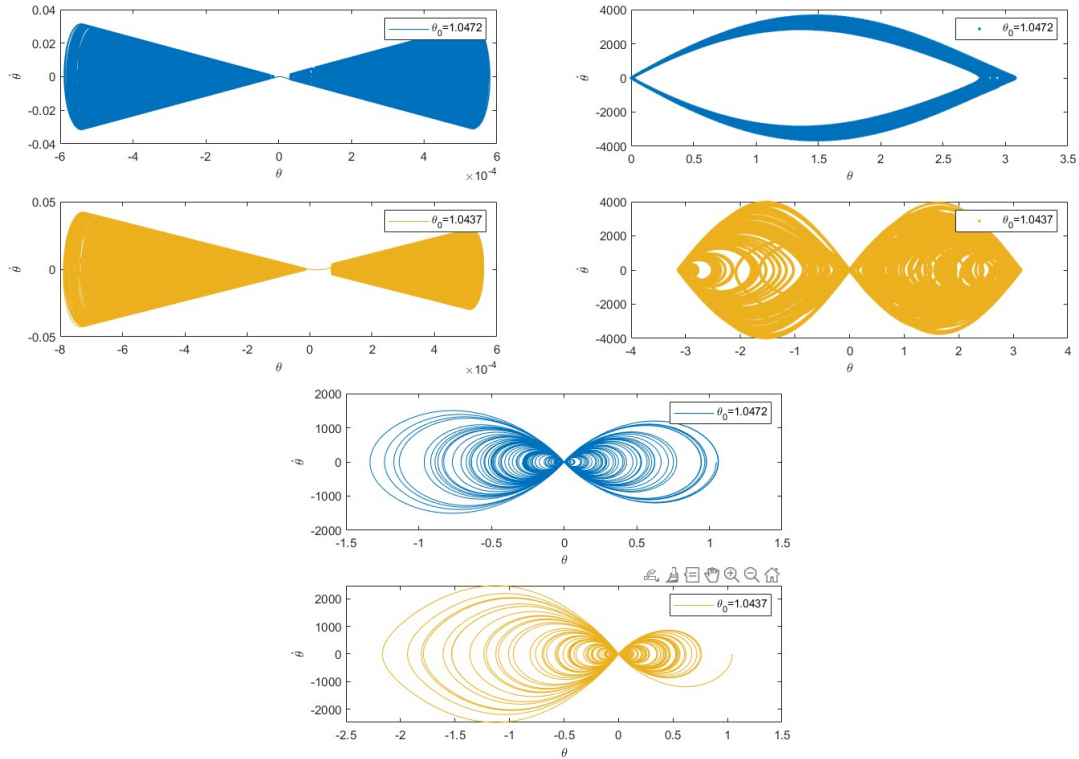


Figure D.3 This figure shows phase space plots for two different initial conditions in each plot. All images were generated using a source frequency of 100 Hz and magnetic field amplitudes of 0.1 kA/m (top left), 7 kA/m (top right), and 10 kA/m (bottom). θ is in units of radians and $\dot{\theta}$ is in units of radians/s.

APPENDIX E

APPLICATION SIMULATION OF BOREHOLE WATER SOLUTION

Chapter 2 discusses application modeling using SimPEG. One assumption of the models discussed in Chapter 2 was that the magnetic field is applied to all of the material in the model. This assumption is problematic because the solenoid would only apply a magnetic field to the water inside the borehole, meaning there would be less material contributing to the magnetic field observed by the sensors. This led to an over-prediction of the TMI anomaly by the models created in Chapter 2 and, therefore, sensitivity requirements of the DMS fiber that are too high.

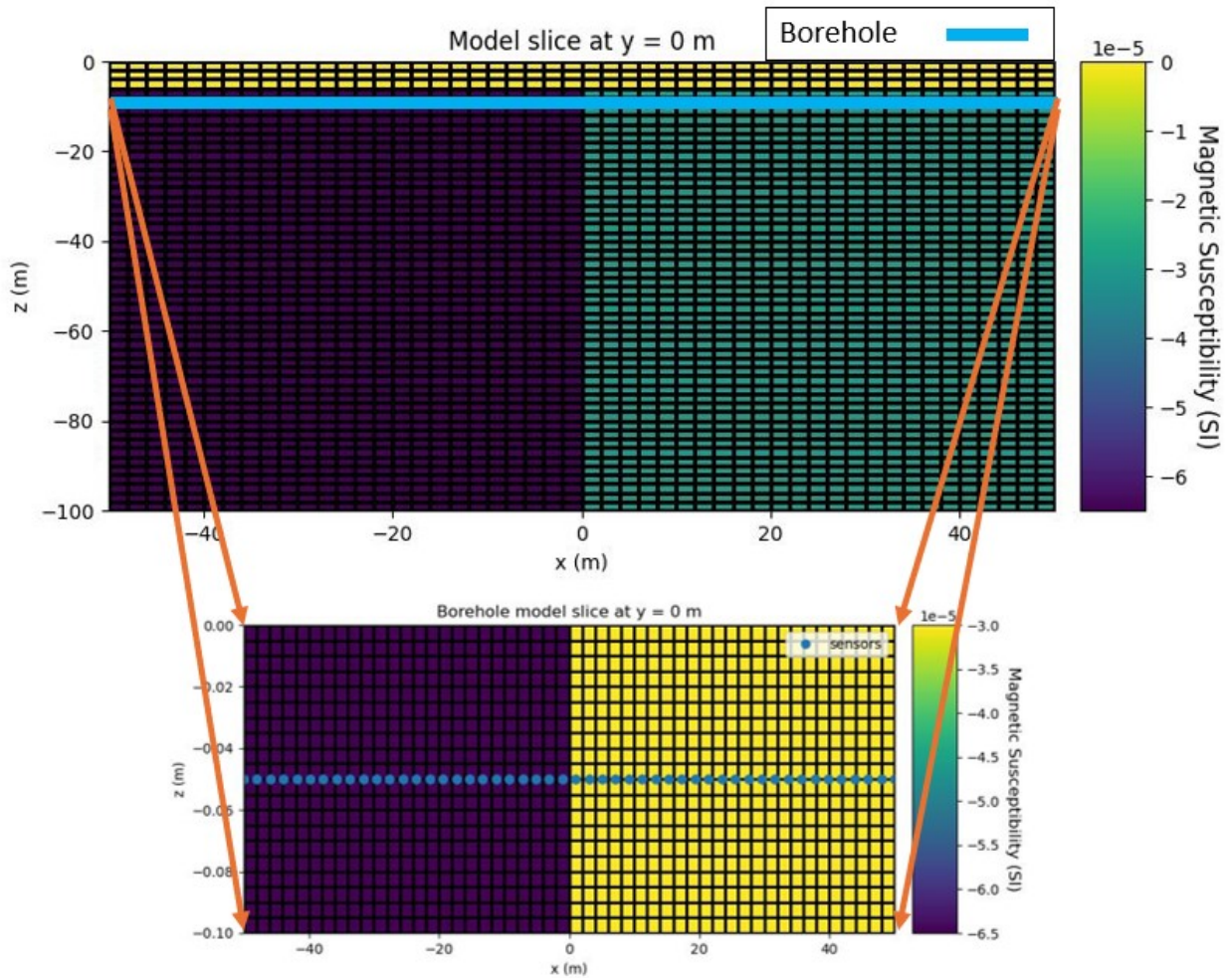


Figure E.1 This figure shows a borehole model slice of the seawater intrusion model illustrated in Figure 2.2. The borehole model only exposes the water in the borehole to an external magnetic field of $560 \mu T$ in the positive x -direction. The borehole has a square cross-section with side lengths of 0.1 m.

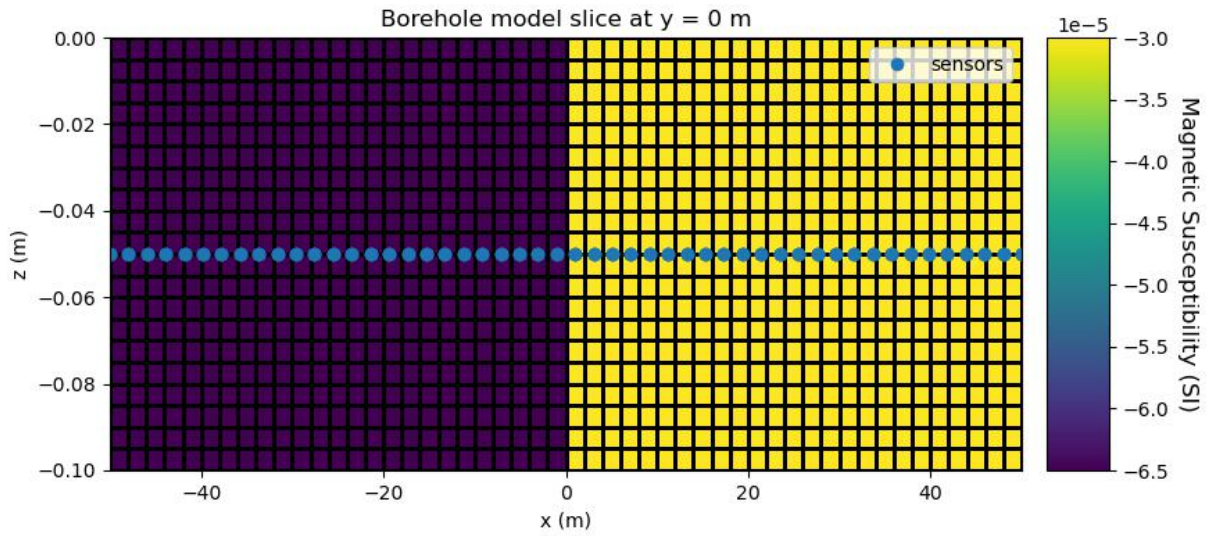


Figure E.2 This figure shows a larger version of the same borehole model shown in Figure E.1. The sensors are shown in the center of the borehole with 2 m spacing.

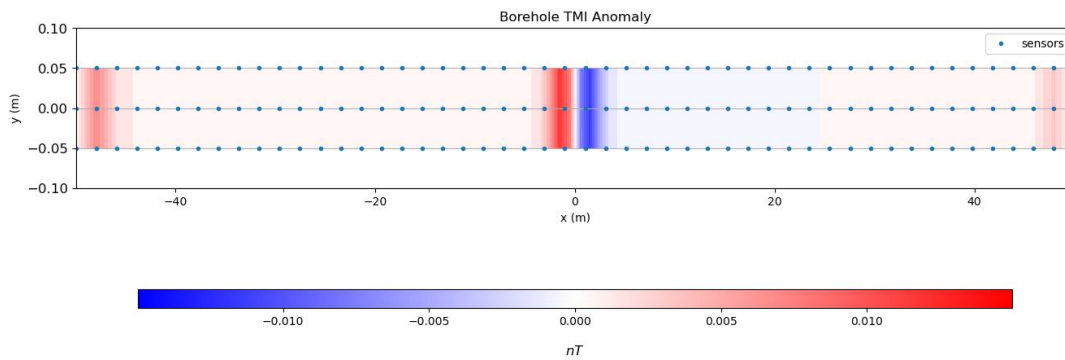


Figure E.3 This figure shows the forward modeled TMI anomaly for the borehole seawater intrusion model shown in Figure E.2. This figure shows a cross-section of the borehole at the sensor z location of -0.05 m. The three lines of sensors are shown with a spacing of 2 m. There is a clear difference in TMI anomaly at $x = 0$ m, where the saltwater-freshwater interface is in the model.

To account for this issue of applying a magnetic field to the whole model shown in Figure 2.2, we can create a model of only the water in the borehole fluid. This model assumes a borehole with a square cross-section that is 100 m long with side lengths of 0.1 m, with a uniform magnetic field of $560 \mu T$ applied in the positive x-direction. Three lines of sensors with a spacing of 2 m in the x-direction, to simulate the fiber Bragg grating spacing, and 0.05 m in the y-direction were placed along the borehole to span the space required by SimPEG for numerical integration. The magnetic susceptibility values for this seawater intrusion model are $\chi_{saltwater} = -6.5 \times 10^{-5}$ and $\chi_{freshwater} = -3.0 \times 10^{-5}$. The relation of this borehole model to the seawater intrusion model shown in Figure 2.2 is illustrated in Figure E.1. A depth slice of this SimPEG model is shown in Figure E.2, with a corresponding forward model shown in Figure E.3. With the model created in this nontraditional way, it is more appropriate to call the depth slice a borehole slice.

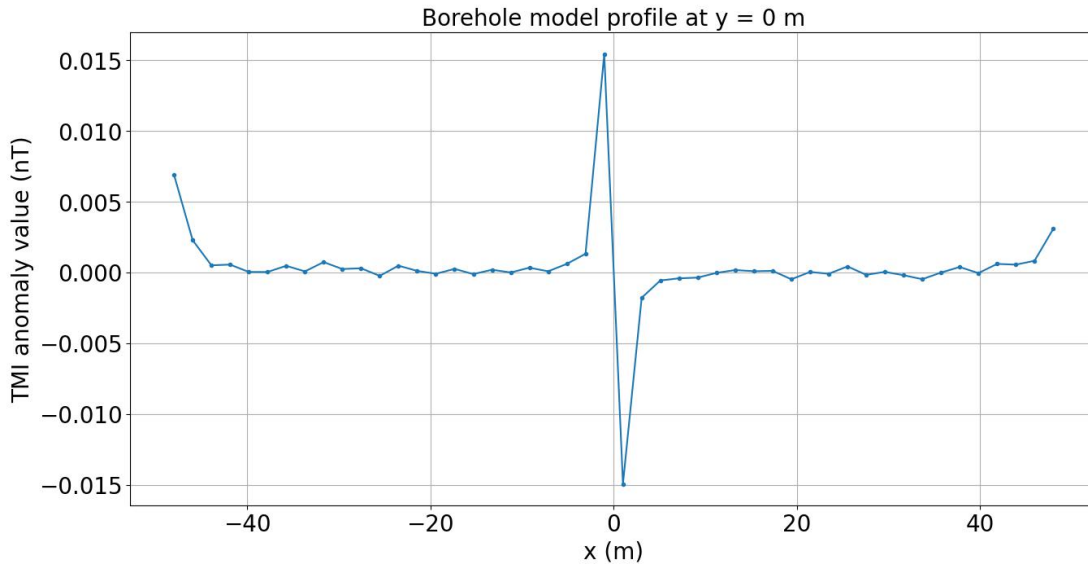


Figure E.4 This figure shows the TMI anomaly contour value along $y = 0$ m at $z = -0.05$ m in Figure E.3. A difference in TMI anomaly of 0.03 nT is apparent at $x = 0$ m, where the saltwater-freshwater interface is in the model.

The profile along $y = 0$ m of the borehole is shown in Figure E.4. There is a TMI anomaly difference of 0.03 nT at the seawater-freshwater interface. This result is $\sim 1,000$ times smaller than the 17 nT interface difference seen in the simple seawater intrusion forward model, shown in Figure 2.3. This simulation result alone provides strong evidence that the models discussed in Chapter 2, which are based on a constant magnetic field throughout the entire subsurface region, have much larger TMI anomaly differences at boundaries than the scenario with a solenoid source.

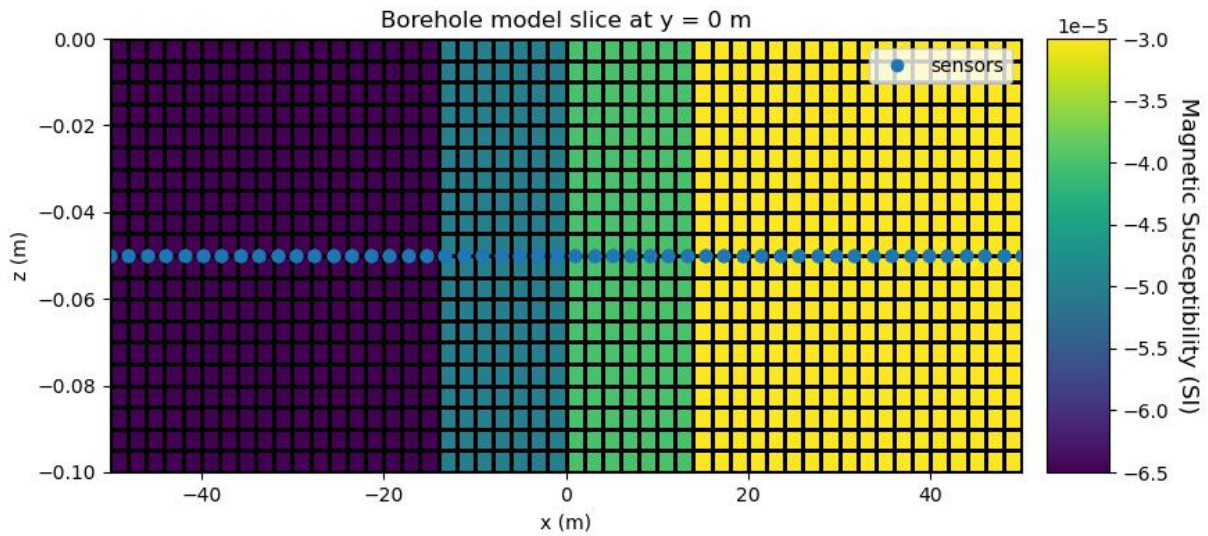


Figure E.5 This illustration shows the borehole model at $y = 0$ m that was created for magnetic simulation of the complex seawater intrusion model in Figure 2.6. The saltwater is on the left with a gradient in χ towards the freshwater. The χ values from left to right are $\chi_{seawater} = -6.5 \times 10^{-5}$, $\chi_1 = -5 \times 10^{-5}$, $\chi_2 = -4 \times 10^{-5}$, and $\chi_{freshwater} = -3 \times 10^{-5}$.

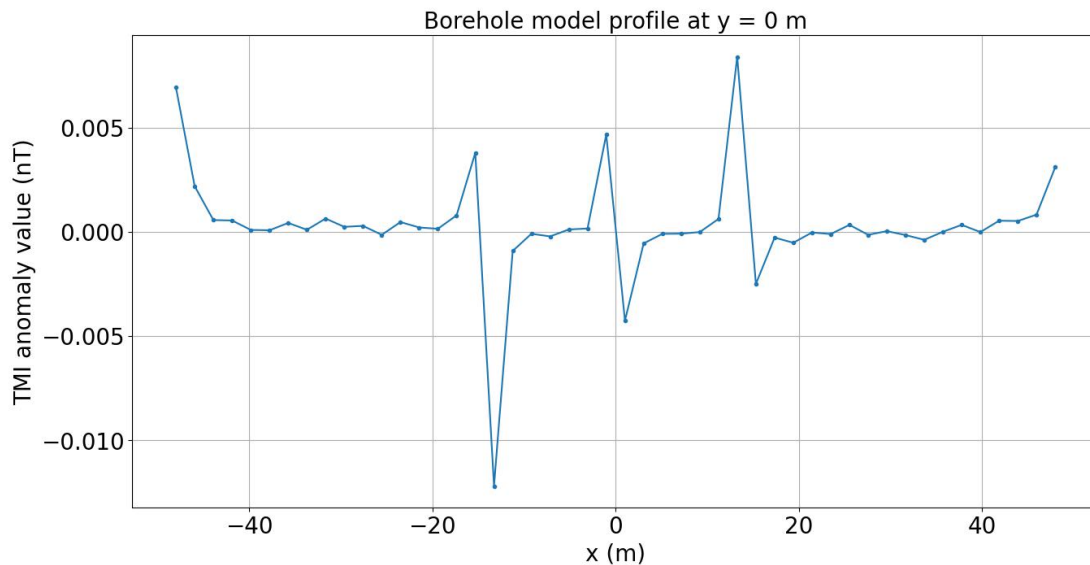


Figure E.6 This figure shows the TMI anomaly contour value along $y = 0$ m at $z = -0.05$ m of the forward modeled results from Figure E.5. Differences in TMI anomaly of 0.015 nT, 0.009 nT, and 0.008 nT are apparent at $x = -15$ m, $x = 0$ m, and $x = 15$ m where the gradient changes in salinity are in the model.

Since such a large change in TMI anomaly difference at the saltwater-freshwater interface was observed in the simple saltwater intrusion model, a borehole model for the saltwater gradient model in Figure 2.6 was created as well, shown in Figure E.5. The χ values from negative to positive x values are $\chi_{seawater} = -6.5 \times 10^{-5}$, $\chi_1 = -5 \times 10^{-5}$, $\chi_2 = -4 \times 10^{-5}$, and $\chi_{freshwater} = -3 \times 10^{-5}$. There is no dipping boundary within the borehole, as shown in Figure 2.6, since the borehole is a small hole through the subsurface model. The magnetic field and borehole dimensions are the same as discussed for the simple interface in Figure E.2.

The forward modeled data was computed using the model in Figure E.5. A profile of the forward modeled data at $y = 0$ m is shown in Figure E.6. The profile shows differences in TMI anomaly of 0.015 nT, 0.009 nT, and 0.008 nT at $x = -15$ m, $x = 0$ m, and $x = 15$ m, respectively, where the gradient changes in salinity are in the model. In comparison to the gradient model response to a field applied to an entire region, shown in Figure 2.8, which shows TMI anomaly differences of 2 nT to 2.5 nT, the borehole model TMI anomaly differences are ~ 100 times lower.

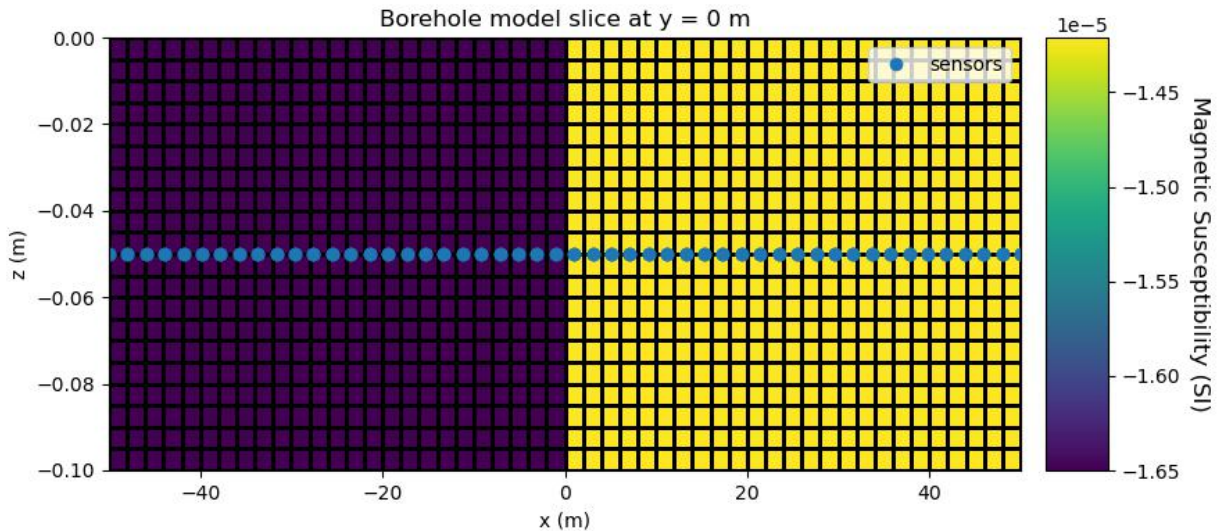


Figure E.7 This figure shows the borehole model for the mine drainage and lithium brine model. The freshwater is on the left and the metal ion solution of Fe^{2+} or Li^+ is on the right. This image shows the model of an Fe^{2+} concentration of 1000 mg/L.

Models were also created for borehole water with concentrations of Fe^{2+} and Li^+ , shown in Figure E.7. In these models, the freshwater block was created for negative x values and the water with metal ions was created for positive x values. The magnetic susceptibility of the metal ion solution was calculated using Equation 2.1. The magnetic field and borehole dimensions are the same as discussed for the simple interface in Figure E.2.

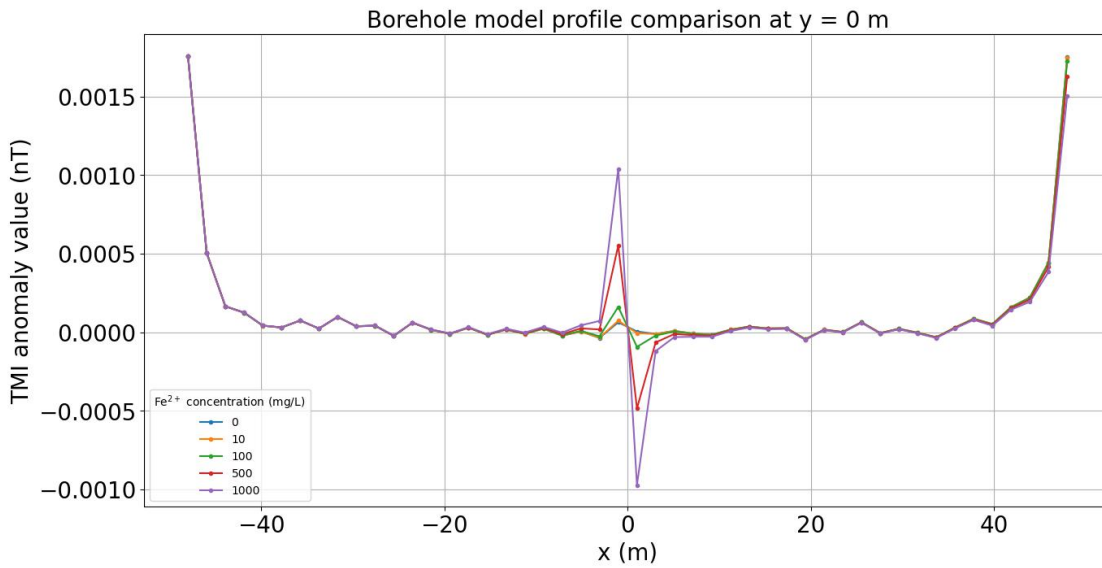


Figure E.8 This figure shows the TMI anomaly contour value along $y = 0$ m of the forward modeled results from Figure E.7. Fe²⁺ concentrations were varied from 0 mg/L to 1000 mg/L.

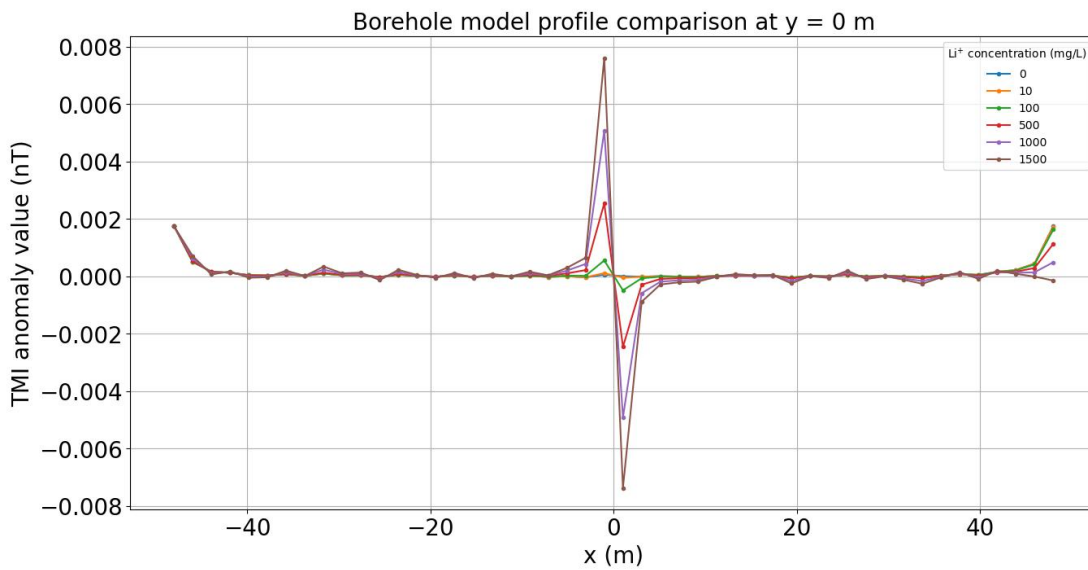


Figure E.9 This figure shows the TMI anomaly contour value along $y = 0$ m of the forward modeled results from Figure E.7. Li⁺ concentrations were varied from 0 mg/L to 1500 mg/L.

Fe^{2+} concentrations were varied from 0 mg/L to 1000 mg/L in Figure E.8 and forward modeled data was computed, from which the TMI anomaly contour value along $y = 0$ m was extracted, shown in Figure E.8. These results demonstrated that the TMI anomaly difference for 100 mg/L of Fe^{2+} is 0.0003 nT. This is $\sim 1,000$ times lower than the mine drainage scenario result for 100 mg/L of Fe^{2+} in Chapter 2, which had a TMI anomaly difference of 0.25 nT.

Li^+ concentrations were varied from 0 mg/L to 1500 mg/L in Figure E.9 and forward modeled data was computed, from which the TMI anomaly contour value along $y = 0$ m was extracted, shown in Figure E.8. These results demonstrated that the TMI anomaly difference for 100 mg/L of Fe^{2+} is 0.001 nT. This is $\sim 1,000$ times lower than the mine drainage scenario result for 100 mg/L of Li^+ in Chapter 2, which had a TMI anomaly difference of 1 nT.

From the models discussed in this appendix, it is apparent that the models discussed in Chapter 2 over-predicted the TMI anomaly difference by ~ 100 to $\sim 1,000$ times. This also means that magnetic field sensitivity requirements for the DMS fiber should be ~ 100 to $\sim 1,000$ times lower if this modeling is used to estimate fiber sensitivity requirements. Further modeling with the method outlined in this appendix could be performed to determine the effect that borehole dimensions have on sensitivity requirements. Increasing the borehole dimensions should increase TMI anomaly since more water is exposed to the external magnetic field, however, model simulations are required to verify this hypothesis.

This appendix only addressed one model issue discussed in Chapter 2, however including an alternating magnetic field in the model and the effect of other ions on magnetic susceptibility still needs to be addressed. If these two issues are discussed with this borehole model, then this modeling would be more realistic. Two other concerns following these model additions would be to include the effects that different casings may have on the results and the effect that including noise in the forward modeled data has on the final results.